CONTENTS

ABSTRACTS

Edyta Andrysewicz, Joanna Mystkowska, Jan Ryszard Dąbrowski, Ewa Och, Katarzyna Skolimowska, Marcin Klekotka
The Influence of Saliva and Its Substitutes on Corrosion of Some Implant Alloys

The purpose of this paper is evaluation of the influence of human saliva and its substitutes on the corrosion resistance of some implant alloys used in stomatology, which included: austenitic steel (316L), titanium alloy (Ti6Al4V), and cobalt alloy (CoCrMo). Corrosion studies were conducted by means of the potentiodynamic method with the application of the VoltaLab 21 kit with VoltaMaster 4 software. The reference electrode was a saturated calomel electrode (SCE), whereas the counter electrode was a platinum electrode. The results of conducted studies indicate an increased current density in the passive range on potentiodynamic curves of studied alloys in the environment of human saliva, and also in a commercial saliva solution – Mucinox. On the basis of conducted corrosion studies, it can be stated that in terms of corrosion resistance the developed saliva substitutes may constitute competitive solutions to commercial saliva substitutes. The prepared substitutes should be studied further from the perspective of practical application for patients. The original value of the paper is a proposition of new saliva substitutes.

Ľuboš Kaščák, Emil Spišák, Ivan Gajdoš
Joining the Combination of AHSS Steel and HSLA Steel by Resistance Spot Welding

The paper deals with the optimization of parameters of resistance spot welding and quality analysis of welded joints made by combination of galvanized Advanced High Strength Steel and High Strength Low Alloy steel. It is an advanced material combination utilized in automotive industry to reduce weight of the vehicle body and consequently lowering the fuel consumption to achieve the lowest possible fuel consumption, high active and passive safety of passengers while decreasing the amount of emission. The quality of welded joints was evaluated by destructive tests and non-destructive tests. The shear tensile test according to STN 05 1122 standard was used. Some samples were prepared for metallographic analysis, where the influence of the welding parameters on the structure of welded joint and occurrence of pores in the weld metal caused by evaporation of zinc from the coating was observed.

Ľuboš Kaščák, Emil Spišák, Jacek Mucha
Clinchrivet as an Alternative Method to Resistance Spot Welding

Various materials are used in car body production which are not always possible to join by conventional joining methods such as resistance spot welding. Therefore ClinchRivet method seem to be possible alternative. The paper deals with evaluation of properties of the joints made by mechanical joining method – ClinchRivet. The joint is made with the using of a special rivet, which is pushed into the joined materials by the flat punch. Following materials were used for joining of this method: DX51D+Z and H220PD steel sheets. The tensile test for observing the carrying capacities and metallographicall analysis were used for the evaluation of joint properties. Some results of the tests of ClinchRivet joints were compared to the properties of the joints made by resistance spot welding.

Tomasz Kubiak, Zbigniew Kołakowski
Thin-Walled Epoxy-Glass Fibre Beams Subjected to Pure Bending

Buckling and postbuckling behaviour of thin-walled channel section beam made of epoxy-glass composite have been considered. The beams under analysis was subjected to pure bending. The main aim was check the influence of ply arrangement on buckling load and postbuckling behaviour and validate the authors analytical-numerical method by commercial finite element method software. Mentioned analytical-numerical method has been developed for more than 25 years in Department of Strength of Materials. This method uses asymptotic Koiter theory for conservative systems in the second order approximation modified by Byskov and Hutchinson. Additionally, using the finite element method software the influence of ply arrangement on failure load were checked.

Jerzy Madej, Bartłomiej Będkowski
Air Flow Analisis for Electrical Motor's Cooling System with Autodesk Simulation CFD 2013 Program

In the article the analysis of airflow through electrical motor was conducted and optimal design solution was chosen in order to increase cooling efficiency. Numerical simulations allow to determine the areas of temperature occurrence which may have destructive influence on electrical motor parts and on its safe operation. The numerical calculations of airflow was carried out for two different types of fans as well as for two different housings. An analysis of the construction was carried out by CFD method using Autodesk Simulation CFD 2013. Community results of the analysis, we can conclude that the better solution for machines with fixed direction of rotation is to use instead of the radial the axial fan. For axial fan the motor temperature in the same condition was lower by about 5°C.

Stanisław Mroziński, Michał Piotrowski
Influence of Temperature and Loading Program on the Fatigue Life of Steel P91

In this paper there are shown the results of low-cycle fatigue testing of steel P91 samples. During the testing there was conducted a fixed amplitude loading testing as well as programmed loading with various sequence degrees of the program. The testing was done in two temperatures: T=20□C and T=600ºC. During the testing a cyclic steel weakening was observed without a clear period of stabilization. Greater changes of the cyclic properties were observed in temperature T=600ºC. The influence of temperature on the fatigue life was determined in this paper. This influence is dependent on the degree of strain. It's a minor one in the range of big strain and increases in the process of decreasing the degree of strain. Furthermore, the impact of the loading program type was determined on the test results and fatigue life calculations.

Michał Petaś, Krzysztof Mróz, Krzysztof Doliński
Damage Modeling in Graded Layer System

The simplified approach to the modelling of low cycle fatigue (LCF) of functionally graded materials (FGM) based on the continuum mechanics is presented. The fatigue damage model takes into account the mechanical part of the load and a constant service temperature. The concept of FGM as a particle-reinforced metal-matrix composite with gradual change of the reinforcement fraction is used. The FGM is considered as a material consisting of homogeneous layers containing different volume fractions of the reinforcement. The variation of the reinforcement fraction changes the material properties for each layer. The different material properties are obtained according to modified rule of mixture. Since the fatigue damage of metal matrix composites is strongly influenced by the inelastic deformation of the metallic matrix, the constitutive equations of LCF damage model are taken into consideration. The combined isotropic/kinematic hardening model with linear behaviour of isotropic and kinematic parts of hardening is adopted. The damage scalar parameter is associated with the plastic energy dissipation which is used to update the material properties. The fatigue damage model presented in this paper is applied to the fatigue damage analysis of the cooling channel of thruster used in space shuttles and rockets.

Bogdan Sapiński, Wojciech Horak
Rheological Properties of MR Fluids Recommended for Use in Shock Absorbers

The paper summarises the results of laboratory testing of rheological behaviour of (magnetorheological) MR fluids designed for use in shock absorber and vibration dampers. The experiments used a rotational rheometer with an extra chamber inside which a uni-form magnetic field can be generated. Underlying the description of rheological properties of fluids is the Herschel-Bulkley's model of viscous-plastic substances. The aim of the experiment was to determine the shear stress, yield stress, the yield factor and the power-law exponent depending on the magnetic flux density, followed by the comparative study of rheological parameters of investigated fluids.

Bogdan Sapiński, Wojciech Horak,Marcin Szczęch
Investigation of MR Fluid in the Oscillatory Squeeze Mode

The paper summarises the results of laboratory testing of three commercially available magnetorheological (MR) fluids operated in the oscillatory squeeze mode. Tested fluids include the Basonetic 204 and Basonetic 4035 (BASF) and MRF-122EG (Lord Corporation). The oscillatory squeeze mode produces large forces at small displacements. This feature may be well utilised in fabrication of new MR devices. The purpose of the experiments was to evaluate the suitability of MR fluids for applications in MR vibration dampers being developed under the current research project. The results enable a comparative analysis of investigated fluids and verification of phenomena encountered in the oscillatory squeeze mode and reported in the literature.

Ján Slota, Miroslav Jurčišin, Ivan Gajdoš, Emil Spišák
The Sensitivity of a Photogrammetric Method in Formability Analysis

Nowadays is a possible to implement numerical simulation and photogrammetric inspection to the complex process chain of inspection. In the recent years there has been significant progress in accuracy improving of these methods of inspection in pre-production or post-production stage of manufacturing. This article discusses these two methods from sensitivity and comparison point of view. Most attention has been paid to the photogrammetric method and his sensitivity to using different approaches. Results were compared with the result of numerical simulation and experiment. Numerical simulation was performed in static implicit finite element code Autoform. For this purpose, GPS cover of galvanized steel of DQ category was used for inspection. In this paper was proved that photogrammetric method of strain measurement is highly sensitive on the various external factors. Further results and findings are included in the next chapters of this paper.

THE INFLUENCE OF SALIVA AND ITS SUBSTITUTES ON CORROSION OF SOME IMPLANT ALLOYS

Edyta ANDRYSEWICZ*, Joanna MYSTKOWSKA*, Jan Ryszard DĄBROWSKI*, Ewa OCH*, Katarzyna SKOLIMOWSKA*, Marcin KLEKOTKA*

*Faculty of Mechanical Engineering, Department of Materials and Biomedical Engineering, Bialystok University of Technology, ul. Wiejska 45 C, 15-351 Bialystok, Poland

edchem@o2.pl, j.mystkowska@pb.edu.pl, j.dabrowski@pb.edu.pl, ewa.kulesza1@gmail.com,skolimowska.katarzyna@gmail.com, m.klekotka@pb.edu.pl

Abstract: The purpose of this paper is evaluation of the influence of human saliva and its substitutes on the corrosion resistance of some implant alloys used in stomatology, which included: austenitic steel (316L), titanium alloy (Ti6Al4V), and cobalt alloy (CoCrMo). Corrosion studies were conducted by means of the potentiodynamic method with the application of the VoltaLab 21 kit with VoltaMaster 4 software. The reference electrode was a saturated calomel electrode (SCE), whereas the counter electrode was a platinum electrode. The results of conducted studies indicate an increased current density in the passive range on potentiodynamic curves of studied alloys in the environment of human saliva, and also in a commercial saliva solution – Mucinox. On the basis of conducted corrosion studies, it can be stated that in terms of corrosion resistance the developed saliva substitutes may constitute competitive solutions to commercial saliva substitutes. The prepared substitutes should be studied further from the perspective of practical application for patients. The original value of the paper is a proposition of new saliva substitutes.

Key words: Metallic Alloys, Corrosion, Human Saliva, Saliva Substitute, Prosthodontia

1. INTRODUCTION

Human saliva fulfills many important functions in the human organism (e.g. digestive, protective, excretory, buffering, demineralizing, nutritional). However, it can also be the cause of health problems for patients (Dodds et al., 2005; Amerongen et al., 2002; Rantonen, 2003; Brosky, 2007; Zalewska et al., 2007; Kaczmarek, 2007). Disadvantageous processes leading to an increase in the intensiveness of destruction of metallic elements in the human stomatognathic system can be observed in the oral cavity Chaturvedi (2009). The most often cause of this phenomenon is the aggressiveness of the contact environment, which may lead to initiation of corrosive processes in metallic biomaterials, and thus, to worsening of their biofunctional properties (Sharma et al., 2008; Upadhyay et al., 2006). In this case, this pertains to contact of human saliva with metallic biomaterials used in stomatology. As a result, the phenomenon of corrosion takes place.

Processes of destruction of stomatological implants, orthodontic apparatus, metallic fillings or elements of stomatological prostheses mainly result from biological metabolic reactions occurring in a living organism. These are phenomena that result from the reaction of hydrogen emission and oxygen absorption from the tissue surrounding the implant, variable body temperature, changes in the pH of body fluids, factors of exploitation (e.g. friction processes, mechanical damage, overload, incorrect implant geometry, and the presence of specific ions (e.g. chlorine, sodium, potassium, calcium, and magnesium phosphate) (Sharma et al., 2008; Upadhyay et al., 2006; Świeczko-Żurek, 2009; Hansen, 2008). They also include the influence of proteins, enzymes, fluoride ions, and bacteria from biofilms present in saliva (Lee and Newman, 2003, Jayaraman et al., 1997a, b). Other pathogenic factors include: improper diet and oral cavity hygiene, or medication taken by patients (Canay and Oktemer, 1992; Wataha, 2000). Metallic biomaterials are exposed to pitting, fatigue, fretting, and crevice corrosion (Reclarua et al., 2005; Blackwood, 2010; Manivasagam, 2010). It is worth noting that many types of corrosion may be present in a single implant. The development of this process causes toxic and allergic reactions, inflammatory states, development of tumors or metalosis in the human organism (Chaturvedi, 2009; Santonen et al., 2010; Marciniak and Paszenda, 2005). In addition, metal ions released from metallic stomatological implants as a result of corrosion may travel to the digestive tract and accumulate in the stomach, liver, spleen, kidneys, bones, lungs, brain, or in the mucous membrane. In stomatology, local toxicity of metals and their alloys is encountered most often. The effect of suction of human saliva (of an increased acidity) into the interiors of contraction cavities found in metallic biomaterials caused by pulsatory changes in their volume (during cyclic deformations, e.g. of prosthetic implants during chewing), accelerates corrosion of prostheses due to the formation of a concentration cell. In relation with this, conduct of corrosion resistance studies of implants in a tissue or body fluid environment is very important, and the results of these studies should be used to develop chemical compositions of alloys used in stomatology and artificial saliva solutions (Mareci et al., 2007, 2011; Rajendran et al., 2010). A lack of activity of corrosive processes is considered to be one of the most important parameters for biocompatibility of materials used in medicine (Bedi et al., 2009).

One of the methods of treatment and prevention of the destructive processes in the oral cavity (dryness of the oral cavity, use of prostheses, etc.) is the application of e.g. lubricants (vaseline or glycerin, etc.) or substitutes in the form of fluids or gels (Kaczmarek, 2007).

In many scientific centers, attempts are being made to create preparations with properties that are as similar as possible to those of human saliva, for the purpose of improving the comfort of life for a certain group of patients. In addition, these substitutes are to positively impact the utilitarian properties of dental fillings as well as ceramic and metallic biomaterials in the oral cavity. An important criterion for admission of such substances for use by patients is their lack of aggressiveness towards metallic biomaterials (Wang, 1996; Surowska, 2009; Unalan et al., 2009; Manivasagam et al., 2010; Grogogeat et al., 1999; Adya et al., 2005; Barao et al., 2011; Kocjan and Conradi 2010).

Because of their properties, metal alloys are the materials generally used to produce dental implants. Due to the nature of the human body, it is necessary to learn about the electrochemical properties of applied biomaterials, which facilitates their selection for the purpose of ensuring the best biocompatibility (Bundy, 1994).

Evaluation of corrosion resistance of metallic biomaterials used in stomatology is included in the group of accelerated electrochemical tests.

The aim of this work was to evaluate the corrosion properties of human saliva and its substitutes under in vitro conditions, using the example of metallic materials most commonly used in dental implantology, such as: steel (316L), a titanium alloy (Ti6Al4V), and a cobalt alloy (CoCrMo).

2. MATERIALS AND RESEARCH METHODOLOGY

Human saliva, its commercial substitutes, and three preparations with compositions developed at the Department of Materials and Biomedical Engineering of the Bialystok University of Technology (Tab. 1), were subjected to tests. The selection of the ingredients of the developed saliva substitutes was based on the wide application of these ingredients in the pharmaceutical industry (toothpastes, mouthwashes, etc.) (Kaczmarek, 2007).

Tab. 1. Lubricants used in the corrosion tests

Solution A	human saliva
Solution B	PBS (phosphate buffered saline, pH=7)
Solution C	hydrated tetra-sodium pyrophosphate (Sigma-Aldrich) + di-sodium dihydrogen phosphate (Sigma-Aldrich) + tetra-potassium pyrophosphate (Sigma-Aldrich) + xanthan gum (Sigma-Aldrich) in PBS (phosphate buffered saline) of pH=7.0;
Solution D	type II mucin solution (Sigma-Aldrich) in PBS of pH=7.0
Solution E	type III mucin solution (Sigma-Aldrich) in PBS of pH=7.0
Solution F	Mucinox (PARNELL PHARMACEUTICALS)
Solution G	BioXtra (BIO-X HEALTHCARE)

For the purpose of achieving repeatable test conditions for human saliva, a previously developed method for its acquisition was applied (Andrysewicz et al., 2008).

Corrosion resistance tests of 316L steel, Ti6Al4V titanium alloy, and CoCrMo cobalt alloy in the environment of saliva and its substitutes were conducted on the basis of methodology based on the PN-EN ISO 10993-15 standard ("Biological evaluation of medical products. Identification and quantitative determination of products of degradation of metals and alloys") (PN-EN ISO 10993-15:2009).

Before the test started samples were polished and burnished. For corrosion tests using the potentiodynamic method, the VoltaLab 21 kit with VoltaMaster 4 software was applied, along with measuring vessels with an electrode system and an ultra-thermostat (Fig. 1).

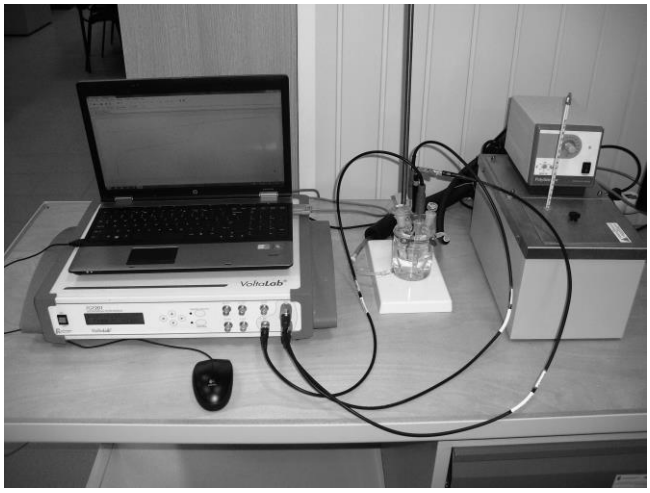

Fig. 1. VoltaLab 21 kit for electrochemical tests with VoltaMaster4 software

The temperature of solutions during tests was equal to 37°C. The reference electrode was a saturated calomel electrode (SCE). The counter electrode was a platinum electrode with a contact surface of 128 mm^2 with the electrolyte. During a time of one hour, the potential of an open system was tested in Solutions B-G. However, tests in Solution A (human saliva) were conducted directly after assembly of the test system, without hourly registration of the potential of the open system (due to precipitation of protein morphotic elements of the saliva and disruptions of the flow of electric current through the tested system). Every kind of sample was tested three times. The middle result of investigations was presented at the work.

Using VoltaMaster 4 software, the values of corrosive potentials and electrical current densities of corrosion (using the Tafel method), corrosion resistance, and yearly loss of material were determined. Samples were polarized in the range of potentials from about open circuit potential (E_{OCP}) – 100 mV to +4 V at a set rate of potential increase of 1 mV/s.

3. DESCRIPTION OF ACHIEVED RESULTS OF OWN RESEARCH

The results of corrosion tests for the tested alloys have been presented in Figs. 2-4 and in Tab. 2-4. Comparisons of corrosion test results for: Solution C have been presented in Fig. 5, for Solution D – Fig. 6, for Solution F – Fig. 7, for Solution A – Fig. 8. Tab. 5-8 contain a list of tested quantities for individual charts, respectively.

The below charts (Fig. 2, Tab. 2) show that 316L steel has the greatest polarization resistance (138 $k\Omega cm^2$) in solution C, which, combined with the high value of corrosion potential (-294 mV) and small annual loss of thickness (0.004593 mm/Y), means that this alloy is the most resistant to corrosion in this environment. It is also worth noting, that despite having an identical corrosion

potential as in solution C, 316L steel exhibits the lowest corrosion resistance in natural saliva (solution A), and this is also indicated by the lowest value of polarization resistance (4 kΩcm^2) and by the greatest annual loss of thickness (0.1637 mm/Y).

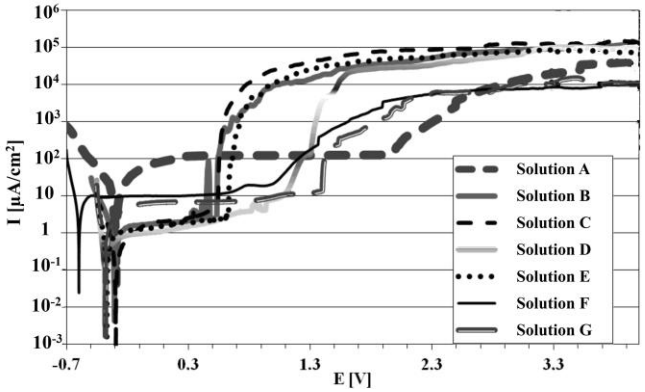

Fig. 2. Potentiodynamic curves for 316 L steel in saliva and its substitutes

Tab. 2. Corrosion properties of 316 L steel

	E_{cor} [mV]	R_p [kΩcm^2]	Corrosion rate [mm/Y]	E_b [mV]
C	-294	138	0.004593	515
D	-381	104	0.001589	1070
E	-367	49	0.004851	615
B	-308	48	0.008319	504
G	-378	29	0.004055	1363
F	-597	5	0.028970	962
A	-294	4	0.163700	1955

where: E_{cor} [V] – corrosion potential, R_p - [kΩcm^2] – polarization resistance, E_b [mV] – breakdown potential.

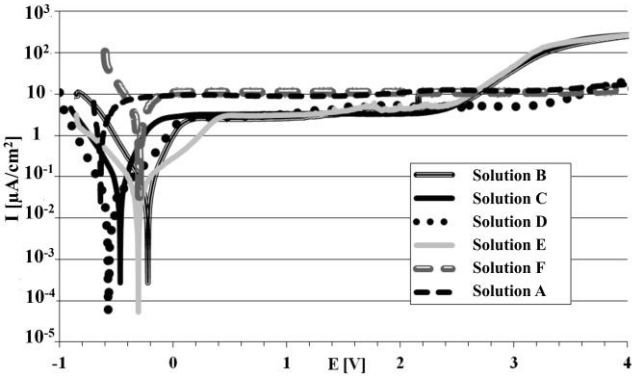

Fig. 3. Potentiodynamic curves of Ti6Al4V alloy in saliva and its substitutes

Tab. 3. Corrosion properties of the Ti6Al4V alloy

	E_{cor} [mV]	R_p [kΩcm^2]	Corrosion rate [mm/Y]	E_b [mV]
E	-305	1620	0.000405	2415
B	-222	970	0.000269	2532
D	-568	889	0.000196	-
C	-466	775	0.000521	2356
A	-637	16	0.006803	-
F	-298	14	0.009404	-

From analysis of Fig. 3 and Tab. 3, it results that the Ti6Al4V alloy is characterized by the greatest polarization resistance in solution E (1629 kΩcm^2) and exhibits, at the same time, a small annual loss of thickness (0.000405 mm/Y) and the greatest corrosion resistance. It should be emphasized that a stable passive range, not exceeding 10 μA/cm^2 for small current densities, was achieved in the environment of all saliva substitutes. The most corrosive environments for the titanium alloy turned out to be the commercially available formula, Mucinox (solution F), and natural saliva (solution A).

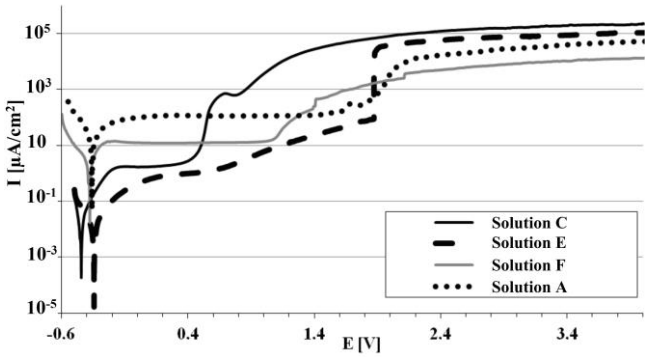

Fig. 4. Potentiodynamic curves of CoCrMo alloy in saliva and its substitutes

Tab. 4. Corrosion properties of the CoCrMo alloy

	E_{cor} [mV]	R_p [kΩcm^2]	Corrosion rate [mm/Y]	E_b [mV]
E	-346	2500	0.000146	1829
C	-446	1480	0.002190	387
F	-379	14	0.021660	1066
A	-361	2	0.402900	1733

It results from Fig. 4 and Tab. 4, that the cobalt alloy in Solution E, is characterized by the highest polarization resistance (2500 kΩcm^2) and breakthrough potential (1829 mV), as well as by a lowest negative corrosion potential (-346 mV). These parameters are decisive of the high corrosion resistance of the alloy in Solution E, manifested in the lowest yearly decrement of thickness (0,000146 mm/Y).

The second part of the work concerns analysis of the influence of the type of solution on the corrosion properties of the three tested metallic materials.

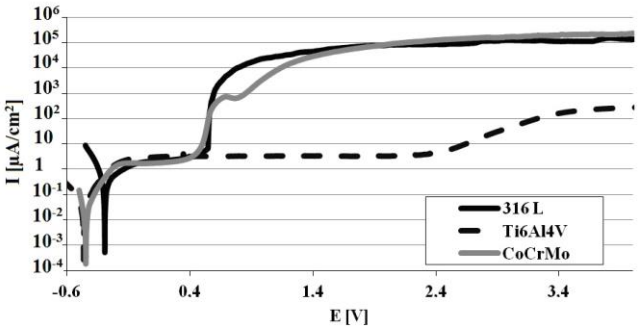

Fig. 5. Potentiodynamic curves in Solution C

Tab. 5. Corrosion properties of materials in Solution C

	E_{cor} [mV]	R_p [kΩcm^2]	Corrosion rate [mm/Y]	E_b [mV]
316 LV	-294	138	0.004593	515
Ti6Al4V	-466	775	0.000521	2356
CoCrMo	-447	1480	0.000219	387

Despite the fact that 316L steel is characterized by the highest corrosion potential (-294 mV) in solution C, it is the CoCrMo cobalt alloy that exhibits the best corrosion resistance due to its high polarization resistance (1480 kΩcm^2) and low annual loss of thickness (0.000219 mm/Y).

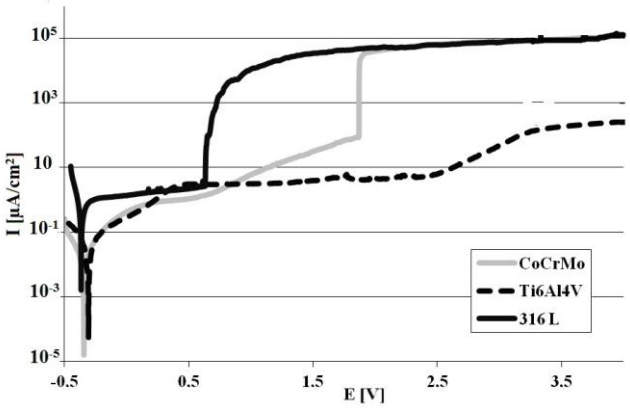

Fig. 6. Potentiodynamic curves in Solution E

Tab. 6. Corrosion properties of materials in Solution E

	E_{cor} [mV]	R_p [kΩcm^2]	Corrosion rate [mm/Y]	E_b [mV]
316 LV	-367	50	0.004851	615
Ti6Al4V	-305	1620	0.000405	2416
CoCrMo	-346	2500	0.000146	1829

Studies showed, that similarly as in the case of solution C, the cobalt alloy also exhibits the highest corrosion resistance in solution E. This solution constitutes the environment that is most aggressive to 316L steel (Fig. 6, Tab. 6). This is indicated by the low value of polarization resistance (50 kΩcm^2) and the low value of breakthrough potential (615 mV).

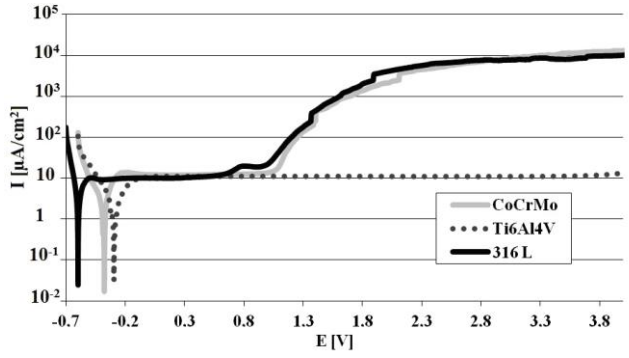

Fig. 7. Potentiodynamic curves in Solution F

Tab. 7. Corrosion properties of materials in Solution F

	E_{cor} [mV]	R_p [kΩcm^2]	Corrosion rate [mm/Y]	E_b [mV]
316 LV	-598	5	0.028970	962
Ti6Al4V	-298	14	0.009404	-
CoCrMo	-379	14	0.021660	1066

In solution F, the studied Ti6Al4V titanium alloy is characterized by the best anti-corrosion properties in comparison with other materials, as made evident by its having the greatest corrosion potential (-298 mV) and the lowest annual loss of thickness (0.009404 mm/Y). However, its polarization resistance is small and similar to the resistance of the CoCrMo cobalt alloy (14 kΩcm^2), as illustrated in Fig. 7 and Tab. 7.

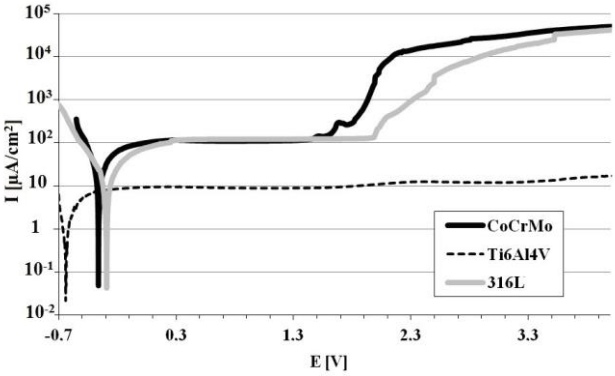

Fig. 8. Potentiodynamic curves in Solution A

Tab. 8. Corrosion properties of materials in Solution A

	E_{cor} [mV]	R_p [kΩcm^2]	Corrosion rate [mm/Y]	E_b [mV]
316 LV	-295	4	0.163700	1955
Ti6Al4V	-637	16	0.006803	-
CoCrMo	-361	2	0.402900	1733

The low polarization resistance value and high values of yearly decrement of thickness achieved through the application of Solution A (Fig. 8, Tab. 8), may be the cause of rapidly advancing corrosion processes in the studied metal alloys.

4. DISCUSSION AND CONCLUSIONS

The success of medical procedures related to the use of metallic implants is dependent on the optimal selection of utilitarian properties of biomaterials and of their physicochemical properties, because the aggressiveness of bodily fluids may lead to the initiation of corrosive processes. Metals used in the human body must be highly resistant to corrosion, which is why in vitro assessments of the corrosion resistance of implant alloys in the environment of artificial bodily fluids are being carried out in many scientific centers (Paszenda, 2010; Reza, 2011; Bellefontaine, 2010).

The authors of this work assessed the corrosion resistance of implant alloys in formulas developed by them at the Department of Materials and Biomedical Engineering. The developed preparations are meant for use by persons with salivary gland disorders

and wearing dental prostheses, particularly to reduce friction and its effects (bruxism, dental prosthetics). The saliva substitutes in which *in vitro* studies were conducted have novel formulas, and in relation to this, no articles were found in which the results of other authors could be compared to the results of this study.

Analysis of the obtained results of studies indicates that natural saliva constitutes the most aggressive environment. This is indicated by unequivocally low values of polarization resistance and high annual losses of thickness for all of the studied implant alloys. The authors' own composition – type III mucin solution in PBS, was characterized by the lowest corrosiveness and exhibited low current densities in the passive range and high polarization resistance for the selected biomaterials.

The CoCrMo cobalt alloy proved to be the most resistant to corrosion in most of the studied environments, followed closely by the Ti6Al4V titanium alloy. CoCrMo alloys have been used in implantology for many decades due to their high resistance to abrasion. The corrosion resistance of this material is improved by increasing Cr concentration or by applying films e.g. with nitrogen ions onto these alloys (Hermawan, 2011; Dobrzański, 2011).

As regards titanium and its alloys, special attention should be paid to the composition and thickness of the surface layer in contact with the human body. The following alloys are characterized by a very high polarization resistance: Ti-6Al-4V, Ti-5AL-2.5Fe and Ti-6Al-7NB (Paszenda, 2010; Hermawan, 2011; Ige, 2009). In the case of the Ti-6Al-4V alloy, there is now an increasingly visible tendency of eliminating vanadium and aluminium and replacing them with other elements e.g. niobium, iron, or zirconium.

Until recently, steels were the most commonly used implant materials, particularly 316L grade steel. Unfortunately, its application was limited because 316L steel is not suitable for long-term *in vivo* exploitation. Its low polarization resistance combined with a high and advancing loss of thickness are indicative of intensive oxidation processes and of the formation of corrosion products, which reduce the biocompatibility of steel. When using implants made from 316L grade steel, special attention is to be paid to the appropriate design and selection of materials for implants (Paszenda, 2010; Ige, 2009; Dobrzański, 2011).

On the basis of conducted corrosion studies, it can be stated that, in terms of corrosion resistance, the developed saliva substitutes may constitute competitive solutions to commercial saliva substitutes. The prepared substitutes should be studied further from the perspective of practical application for patients.

REFERENCES

1. **Adya N., Alam M., Ravindranath T., Mubeen A., Saluja B.** (2005), Corrosion In titanium dental implants: literature review, *The Journal of Indian Prosthodontic Society*, Vol 5, 3, 126-13.
2. **Amerongen A. V. N., Veerman E. C. I.** (2002), Saliva - the defender of the oral cavity, *Oral Diseases*, 8, 1, 12-22.
3. **Andrysewicz E., Dąbrowski J. R., Leonow G.** (2008), Methodological aspects of rheological testing saliva, *Twoj Prz. Stomatol.*, 10-15.
4. **Barao V. A. R., Mathew M. T., Assuncao W. G., Chia-Chun Yuan J., Wimmer M. A., Sukotjo C.** (2011), Stability of cp-Ti and Ti-6Al-4V alloy for dental implants as a function of saliva pH – an electrochemical study, *Clin Oral Impl*, 1–8.
5. **Bedi R. S., Beving D. E., Zanello L. P., Yan Y.** (2009), Biocompatibility of corrosion-resistant zeolite coatings for titanium alloy biomedical implants, *Acta Biomaterialia*, 5, 8, 3265-3271.
6. **Bellefontaine G.** (2010), *The Corrosion Of CoCrMo. Alloys For Biomedical. Applications*, University of Birmingham.
7. **Blackwood D. J.** (2010), *Corrosion In body fluid*, Singapore, 1208-1322.
8. **Brosky M. E.** (2007), The role of saliva in oral health, Strategies for prevention and management of xerostomia, *J Support Oncol*, 5(5), 215-225.
9. **Bundy K.J.** (1994), Corrosion and other electrochemical aspects of biomaterials, *Critical Reviews in Biomedical Engineering*, 22, 3-4, 139-251.
10. **Canay S., Őktemer M.** (1992), In vitro corrosion behavior of 13 prosthodontic alloys, *Quint Int.*, 23, 4, 279–87.
11. **Chaturvedi T. P.** (2009), An overview of the corrosion aspect of dental (titanium and its alloys), *Indian J Dent Res*, 20 (1), 91-98.
12. **Dobrzański L. A., Reimann Ł.** (2011), Influence of Cr and Co on hardness and corrosion resistance CoCrMo alloys used on dentures**,** *J. Achiev. Mater. Manuf. Eng.*, Vol. 49, 2, 193-199.
13. **Dodds M. W. J., Johnson D. A., Yehc Ch. K.** (2005), Health benefits of saliva: a review, *J Dent, 33*, 223–233.
14. **Grosgogeat B., Reclaru L., Lissac M., Dalard F.** (1999), Measurement and evaluation of galvanic corrosion between titanium/Ti6Al4V implants and dental alloys by electrochemical techniques and auger spectrometry, *Biomaterials*, 20, 933-941.
15. **Hansen D. C.** (2008), Metal corrosion in the human body: the ultimate bio-corrosion scenario, *The Electrochemical Society*, 31-34.
16. **Hermawan H., Ramdan D., Djuansjah J. R. P.** (2011), Metals for Biomedical Applications, Biomedical Engineering, from: http://www.intechopen.com/books/biomedical-engineering-from-theory-toapplications/metals-for-biomedical-applications.
17. **Ige O. O., Umoru L. E., Adeoye M. O., Adetunji A. R., Olorunniwo, O. E., Akomolafe I. I.** (2009), Monitoring, Control and Prevention Practices of Biomaterials Corrosion, *Trends Biomater. Artif. Organs,* Vol. 23, 2, 93-104.
18. **Jayaraman A., Cheng E. T., Earthman J. C., Wood T. K.** (1997a), Axenic aerobic biofilms inhibit corrosion of SAE 1018 steelthrough oxygen depletion*, Appl Microbiol Biotechnol*, 48, 11-17.
19. **Jayaraman A., Earthman J.C., Wood T.K.** (1997b), Corrosion inhibition by aerobic biofilms on SAE 1018 steel, *Appl Microbiol Biotechno*,l 47, 62-68.
20. **Kaczmarek U.** (2007), Treatment of mouth dryness – literature review, Czas. Stomatol. LX, 2, 88-95 (in Polish).
21. **Kocjan A., Conradi M.** (2010), The corrosion behaviour of austenitic and duplex stainless steels in artyfical body fluids, *Materials and Technology*, 44, 21-24.
22. **Lee A. K., Newman D. K.** (2003), Microbial iron respiration: impacts on corrosion processes, *Appl Microbiol Biotechnol*, 62, 134–139.
23. **Liu Y., Wang Q., Song Y., Zhang D., Yu S., Zhu X.** (2009), A study on the corrosion behavior of Ce-modified cast AZ91 magnesium alloy in the presence of sulfate-reducing bacteria, *Journal of Alloys and Compounds*, 473, 550–556.
24. **Manivasagam G., Dhinasekaran D., Rajmanickam A.** (2010), Biomedical implants: corrosion and its prevention – a review, *Recent Patents on Corrosion Science*, 2, 40-54.
25. **Marciniak J., Paszenda Z.** (2005), Biotolerance of metallic biomaterials*, Spondyloimplantologia advanced spine treatment system DERO*, Wyd. Polska Grupa DERO, Zielona Gora, 133-142.
26. **Mareci D., Romas M., Cailean A., Sutiman D.** (2011), Electrochemical studies of cobalt-chromium-molybdenum alloys in artificial saliva, *Revue Roumaine de Chimie*, 56, 697-704.
27. **Mareci D., Ungureanu G., Aelenei D. M., Rosca J. C.** (2007), Electrochemical characteristics of titanium based biomaterials in artificial saliva, *Materials and Corrosion*, 58, 848-856.
28. **Paszenda Z., Walke W., Jadacka S.** (2010), Electrochemical investigations of Ti6Al4V and Ti6Al7Nb alloys used on implants in bone burger, *Journal of Achievements in Materials and Manufacturing Engineering*, Vol. 38, 1, 24-32.
29. **PN-EN ISO 10993-15:2009**. *Biological evaluation of medical devices*, Part 15: Identification and quantification of degradation products from metals and alloys.
30. **Rajendran S., Chitradevi P., Johnmary S., Krishnaveni A., Kanchana S., Christy L., Nagalakshmi R., Narayanasamy B**. (2010),

Corrosion behaviour of SS 316L in artificial saliva in presence of electral., *Zastita Materijala*, 51, 149-158.
31. **Rantonen P.**(2003), *Salivary flow and composition in healthy and diseased adults*, University of Helsinki, Helsinki.
32. **Reclarua L., Lüthyb H., Eschlera P.-Y., Blattera A., Suszc Ch.** (2005), Corrosion behaviour of cobalt–chromium dental alloys doped with precious metals, *Biomaterials*, 26, 4358–4365.
33. **Reza H., Bidhendi A., Pouranvari M.**(2011), Corrosion, Study of Metallic Biomaterials In. Simulated Body Fluid, *Metallurgia,* Vol.17, 13-22.
34. **Santonen T., Stockmann-Juvala H., Zitting A.** (2010), *Review on toxicity of stainless stell*, 87s.Helsinki.
35. **Sharma M., Kumar A.V.R., Singh N., Adya N., Saluja B.** (2008), Electrochemical Corrosion Behavior of Dental/Implant Alloys in Artificial Saliva, *JMEPEG*, 17, 695–701
36. **Surowska B.** (2009), *Metaliic biomaterials and metal-to-ceramic of dental applications*, Wyd. Liber Duo S.C., Lublin.
37. **Świeczko-Żurek B.** (2009), *Biomaterials*, Wyd. Politechniki Gdańskiej,151.
38. **Unalan F., Aykor A., Bilhan H.** (2009), The Galvanic Interaction Between a CoCtMo Alloy, Pure Titanium and Two Different Dental Amalgams with Special Attention on the Area Size, *The open Corrosion Journal*, 2, 17-25.
39. **Upadhyay D., Panchal M. A., Dubey R. S., Srivastava V. K.** (2006), Corrosion of alloys used in dentistry: A review, *Materials Science and Engineering:* A, 432, 1–11.
40. **Wang K.** (1996), The use of titanium for medical applications in the USA, *Materials Science and Engineering:* A, 213 134-137
41. **Wataha J. C.** (2000), Biocompatibility of dental casting alloys: a review., *J Prosthet Dent*, 83, 223–34.
42. **Zalewska A. K., Waszkiel D., Kowalczyk A.** (2007), Saliva as a main component of oral cavity ecosystem, *Wiad. Lek.*, 60, 3-4.

Acknowledgement: This scientific work was financed with research funds for the years 2010-2013 as research project N507 592938.

JOINING THE COMBINATION OF AHSS STEEL AND HSLA STEEL BY RESISTANCE SPOT WELDING

Ľuboš KAŠČÁK*, Emil SPIŠÁK*, Ivan GAJDOŠ*

*Faculty of Mechanical Engineering, Department of Technology and Materials, Technical University of Košice, Letná 9, 04200 Košice, Slovakia

lubos.kascak@tuke.sk, emil.spisak@tuke.sk, ivan.gajdos@tuke.sk

Abstract: The paper deals with the optimization of parameters of resistance spot welding and quality analysis of welded joints made by combination of galvanized Advanced High Strength Steel and High Strength Low Alloy steel. It is an advanced material combination utilized in automotive industry to reduce weight of the vehicle body and consequently lowering the fuel consumption to achieve the lowest possible fuel consumption, high active and passive safety of passengers while decreasing the amount of emission. The quality of welded joints was evaluated by destructive tests and non-destructive tests. The shear tensile test according to STN 05 1122 standard was used. Some samples were prepared for metallographic analysis, where the influence of the welding parameters on the structure of welded joint and occurrence of pores in the weld metal caused by evaporation of zinc from the coating was observed.

Key words: Car Body Sheets, Spot Welding, Tensile Test, Microhardness

1. INTRODUCTION

In resistance spot welding, the weld is made by a combination of heat, pressure and time. This technique is commonly used in automotive industry due to its high efficiency in manufacturing thin metal sheets. A wide variety of metal sheets up to 3 mm thickness can be handled by the resistance spot welding method (Sevim, 2006; Spišák et al., 2011). In the last decade a change in body shell mass production has occurred in the automotive industry. In answer to the intensifying energy crisis and in order to meet customer requirements for automobiles such as weight reduction for energy saving and enhancement of passenger safety, new materials, e.g. advanced high strength steels (AHSS) have to be applied (Brauser, 2010; Mucha et al., 2011). These materials are gaining in popularity due to their high strength in combination with good ductility characteristics compared to traditional high strength steels, for example micro-alloyed steels (Tumuluru, 2006). An important AHSS representative is the so-called TRIP (Transformation Induced Plasticity) steel dominated by a ferrite matrix with retained austenite, bainite and martensite as dispersed phases, offering excellent mechanical properties due to the transformation of retained austenite into martensite during plastic straining (Lacroix, 2008). As a result, both strength and uniform strain increase owing to the appearance of a harder phase and to the additional local plastic yielding of the surrounding grains related to the transformation strain as was described in (Saleh and Priestner, 2001). The TRIP effect, which is exhibited by such materials, is characterized by the phenomenon known as strain-induced martensitic transformation (SIMT). Due to the onset of plastic straining, the retained austenite undergoes SIMT which enhances the work hardenability of such steels due to the transformation of the austenite phase to the much harder martensite phase. This brings about a resistance to local necking which explains the uniform elongation and enhanced formability observed in such steels (Sierra and Nemes, 2008).

The challenge of using the coated AHSS steels in the industry is that they are readily inclined to exhibit expulsion during the spot welding. As well, the presence of the coating results in the accelerated degradation of the welding electrodes, leading to earlier expulsion and frequent replacement or re-dressing of the electrodes (Ma et al., 2008; Williams and Parker, 2004).

HSLA steel is well-known type of steel alloy that provides many benefits over regular steel alloys. In general, HSLA alloys are much stronger and tougher than ordinary plain carbon steels. HSLA steels are so called because they only contain a very small percentage of carbon. A typical HSLA steel may contain 0.15% carbon, 1.65% manganese and low levels (under 0.035%) of phosphorous and sulphur. Most HSLA steels are furnished in the as-hot-rolled condition with ferritic-pearlitic microstructure. The exceptions are the controlled-rolled steels with an acicular ferrite microstructure and the dual-phase steels with martensite dispersed in a matrix of polygonal ferrite. These two types of HSLA steels use the formation of eutectoid structures for strengthening, while the ferritic-pearlitic HSLA steels generally require strengthening of the ferrite. Pearlite is generally an undesirable strengthening agent in structural steels because it reduces impact toughness and requires higher carbon contents. Moreover, yield strength is largely unaffected by a higher pearlite content. The ferrite in HSLA steels is typically strengthened by grain refinement, precipitation hardening, and, to a lesser extent, solid-solution strengthening. Grain refinement is the most desirable strengthening mechanism because it improves not only strength but also toughness (Gorni and Mei, 2004; Fernándes et al., 2007; Show et al., 2010).

More cracks and failures tend to occur around welds, in the heat affected zone (HAZ), because the joints are exposed to dynamic and static loads in the automobile structures. After spot wedling, important changes occur in mechanical and metallurgical properties of the spot welded areas and heat affected zones (Vural and Akkus, 2001). The investigation of these changes is very important for the safety strength of the welded joints. In some parts of the modern automobiles, galvanized AHSS steels sheets and HSLA steels sheets are joined together with resistance spot welding technique. The paper evaluates joints of combined materials made by resistance spot welding the materials utilized in automotive industry in car body production.

2. EXPERIMANTAL PROCEDURE

The combination of dissimilar steel sheets were used for resistance spot welding: high strength low alloy steel H220PD with the thickness of 0.8 mm and advanced high strength steel TRIP 40/70+ Z100MBO with the thickness of 0.77 mm. Their basic mechanical properties and chemical composition are shown in Tab. 1 and Tab. 2.

Tab. 1. Basic mechanical properties of used steel sheets

Material	$Rp_{0.2}$ [MPa]	R_m [MPa]	A_{80} [%]	n_{90}
H220PD	238	382	36	0.228
TRIP40/70	450	766	26	0.278

Tab. 2. Chemical composition (wt%) of used steel sheets

Material	C	Mn	Si	Al	Cu	Ni
H220PD	0.012	0.435	0.119	0.041	0.040	0.013
TRIP40/70	0.141	1.627	0.185	1.986	0.053	0.016
Material	**Cr**	**Ti**	**V**	**Nb**	**Mo**	**P**
H220PD	0.046	0.033	0.012	0.052	0.009	0.057
TRIP40/70	0.056	0.007	0.017	0.037	0.024	0.046

The following tests were performed for evaluation of joints` properties: tension test, microhardnesses test and a metallographical analysis. The samples with dimensions of 40 x 90 mm and 30 mm lapping according to STN 05 1122 standard were used for the experiments (Fig. 1). Five samples were prepared for every combination of sheets. Resistance spot welding was carried out in laboratory conditions on a pneumatic spot welding-machine BPK 20 of VTS ELEKTRO Bratislava. CuCr welding electrodes were used according to ON 42 3039.71 standard. The diameter of working area of the electrode was d = ø5 mm.

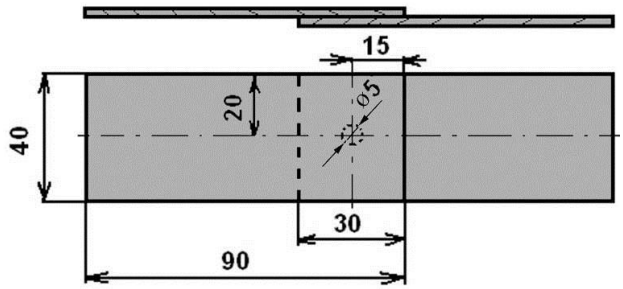

Fig. 1. Dimensions of sample for tensile test

Tab. 3. Welding parameters (I-wedling current, Fz-pressing force, T-welding time

Marking of sample	I [kA]	Fz [kN]	T [per.]	Weld diameter [mm]
A_5	5	6	10	Ø5
A_6	6	6	10	Ø5
A_7	7	6	10	Ø5
A_8	8	6	10	Ø5
A_9	9	6	10	Ø5

The used parameters of resistance spot welding for each sample including pressing force of electrodes Fz, welding time T and welding currents I are shown in Tab. 3. The samples were prepared by cutting against the direction of rolling. The surfaces of the samples were degreased in concentrated CH3COCH3.

The welding current is the most important parameter in resistance welding which determines the heat generation by a power of square as shown in the formula. The size of the weld nugget increases rapidly with increasing welding current, but too high current will result in expulsions and electrode deteriorations. The amount of weld current is controlled by two things: first, the setting of the transformer tap switch determines the maximum amount of weld current available; second, the percent of current control determines the percent of the available current to be used for making the weld. Low percent current settings are not normally recommended as this may impair the quality of the weld. The weld current should be kept as low as possible. When determining the current to be used, the current is gradually increased until weld spatter occurs between the metal sheets (Zhang and Senkara, 2006).

The carrying capacities of the spot welded joints were evaluated according to standard STN 05 1122 – Tension test of spot welded joints. This test was used for measuring the maximum carrying capacities Fmax of the joints. The test was carried out on the metal strength testing machine TIRAtest 2300 produced by VEB TIW Rauenstein, with the loading speed of 8 mm/min.

Further tests for quality evaluation of spot welded joints included the metallographical analysis. The quality of welded joints was evaluated by light microscopy on metallographical scratch patterns prepared according to ISO 6507-1 and ISO 6507-2 standards on Olympus TH 4-200 microscope.

3. RESULTS AND DISCUSSION

The values of carrying capacity of welded joints were in the range from 5224 N to 7496 N. Only one type of the joint occurs in all chosen parameters of welding – fusion welded joint. Measured values of carrying capacities of joints on welding current are shown in Fig. 2.

Dependency of carrying capacity of spot welds *Fmax* on welding current *I* can be expressed (calculation includes 5 samples for each current value):

$$Fmax = 401.49I + 3491 \quad (1)$$

with coefficient of determination R^2 = 0,8829

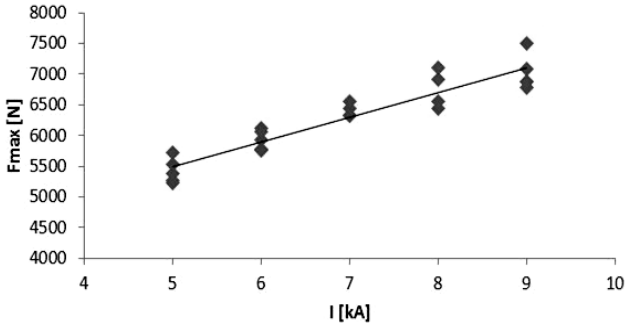

Fig. 2. Dependency of carrying capacities of spot welds Fmax [N] on welding current I [kA]

Tensile tests were executed under displacement control conditions on the specimen configurations in order to characterise the static behaviour of the joints and to estimate the ultimate tensile strength. The maximum shearing load was the most significant value obtained from the ''load-displacement'' curves as shown in Fig. 3 as well as the corresponding displacement. The form of the curves indicates the behaviour of the joints under loading, especially capacity for deformation. The measured values of carrying capacities of the spot welds are shown in Tab. 4.

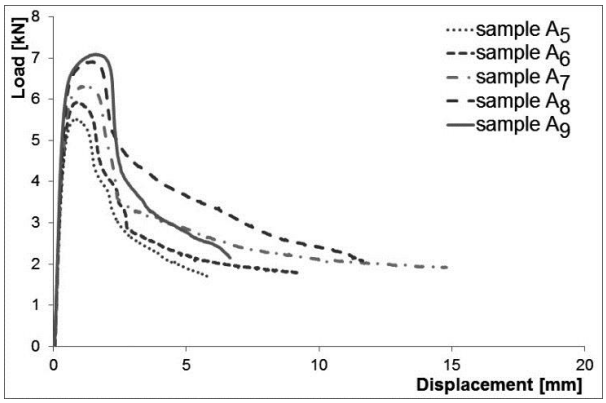

Fig. 3. Load-displacement curves and deformation of spot welded joints after tensile test

Tab. 3. Carrying capacities Fmax of the welds

Fmax [N]					
Sample No.	**A_5**	**A_6**	**A_7**	**A_8**	**A_9**
1	5263	5922	6335	6919	6978
2	5224	5763	6439	6758	7496
3	5383	5771	6562	6835	6982
4	5537	5921	6320	7098	6875
5	5520	6052	6322	6893	7090

The specimen failed partially through the periphery of the weld and partially through the base metal, which is confirmed in the failure mode of spot welded joints (Fig. 4) together with corresponding characteristic load vs. displacement curves generated in the experiments (Fig. 3). The carrying capacities of the samples are then influenced by the base metal strength.

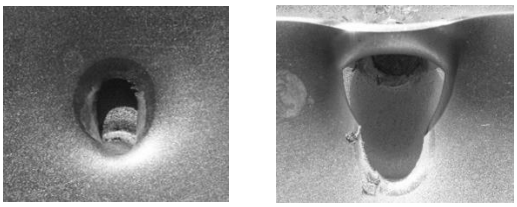

Fig. 4. Failures of spot welded joints of samples A_5 and A_9

Fig. 5 shows indentations formed by the welding electrodes. Changing the values of welding current influenced the welding electrode indentations on the surfaces of welded materials. The most obvious indentations were observed on the surfaces of samples prepared with the parameters of maximum value of welding current of 9 kA. The least obvious indentations were on the surfaces of both welded steels prepared with the minimum value of welding current of 5 kA.

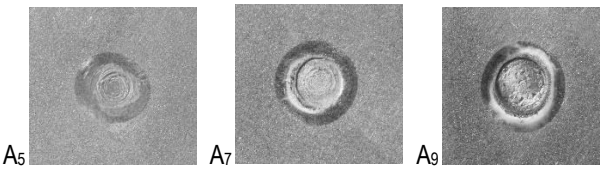

Fig. 5. Welding electrodes indentations of samples A_5 (I = 5kA), A_7 (I = 7 kA) and A_9 (I = 9 kA)

The metallographical analysis confirmed formation of fusion welded joints with characteristic areas of weld metal (WM), heat affected zone (HAZ) and base material (BM). Figure 6 shows the macrostructures of spot welded joints of samples A_5, A_7 and A_9.The size of spot welds increased with increasing values of welding current. The sample A_5 welded with the lowest value of welding current 5 kA shows the smallest weld nugget of all observed samples, with the narrow heat affected zone. The macrostructures of a weld joint show the solidification process of weld metal with a characteristic dendrite structure typical for resistance spot welds. The microscopic observation of macrostructures of the welds shows no pores and cavities occurring in the weld metal. The bigger weld nugget was observed in samples A_7, welded with the current of 7 kA. No pores and cavities occurring in the weld metal.

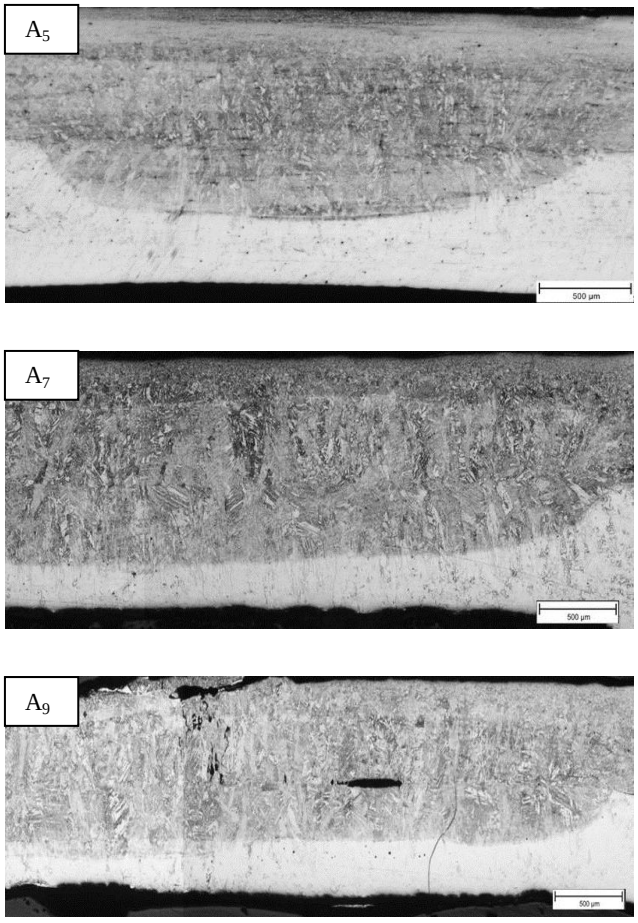

Fig. 6. Microstructures of the samples A_5, A_7 and A_9

The microstructure of weld metal consists of mostly fine-grained martensite arranged in typical lamellar formations form the side of TRIP steel. Such lamellar formations prevent the austenite from transformation; therefore the retained austenite occurs

in the microstructure. Besides martensite, also ferrite and both forms of bainite occur in the microstructure of weld metal. The microstructure of H220PD can be characterized as a fine-grained ferrite-pearlite structure. Because of heating in resistance spot welding, continual growth of grains towards the weld metal can be observed. A significant growth of pearlite grains occurs in the heat affected zone.

The sample A_9 welded with the highest values of welding current 9 kA shows the void and solidification cracks inside the biggest weld nugget. The formation of void in a spot weld is the result of nucleation and growth process during solidification of a liquid nugget after the heat source, i.e. electric current is shut off as was described in (Zhang and Senkara, 2006). The solidification cracking may form under certain condition. The cracks extended from the surface of a weld into its interior with some voids in the nugget. Such cracks may not reduce a joint`s strength if they are confined to the centre of the nugget. However, when they extend to the edges of weld nugget they can affect the weld quality.

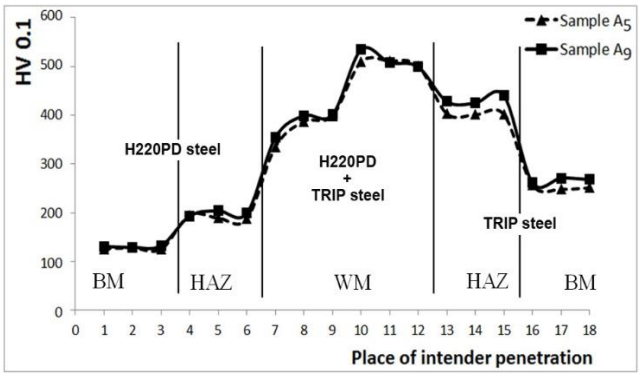

Fig. 7. The values of microstructures of samples A_5 and A_9 (BM-base material, HAZ-heat affected zone, WM-weld metal)

The measured values of microhardness are shown in Fig. 7. The measurements show the changes of the microhardness values in the areas of spot weld. The highest values were measured in the weld metal from TRIP side. The measurements show that increasing the parameters of resistance spot welding does not cause significant microhardness changes in the spot weld.

4. CONCLUSIONS

In this study, resistance spot welds of material combination of galvanized AHSS steels sheets and HSLA steels were evaluated.

On the basis of the conducted experiment, the following conclusions can be formed:

Fusion weld joints occur with all chosen parameters of resistance spot welding.

The highest tensile strength was observed in samples made with welding current of 9 kA. The average carrying capacity of samples was 7024 N. The lowest values of carrying capacity were observed in samples made with welding current of 5 kA, where the average value of carrying capacity decreased by 23 % in comparison to samples A9.

Linear dependence of carrying capacities of spot welds Fmax on welding current I was determined. Increasing values of welding current caused increasing of carrying capacity.

The metallographical analysis confirms that the chosen combination of advanced high strength steels and high strength low alloy steels is suitable for resistance spot welding. On the basis of the results it can be stated, that welding current has a determining influence on the weld joint. When using the welding current of 5 kA, weld joint was of high quality, fusible and without defects, but the weld nugget had smaller dimensions in comparison with other weld nuggets made with higher values of welding current. Welding current of 9 kA is not suitable for the examined thickness and sheet combination, because cracking was observed in the heat affected zone of multi-phase material of TRIP.

REFERENCES

1. **Brauser S., Pepke L.A., Weber G., Rethmeier M.** (2010), Deformation behaviour of spot-welded high strength steels for automotive appli-cations, *Materials Science and Engineering*, Vol. 527, 7099–7108.
2. **Fernández J., Illescas S., Guilemany J.M.** (2007), Effect of microalloying elements on the austenitic grain growth in low carbon HSLA steel, *Materials Letters*, Vol. 61, 2389-2392.
3. **Gorni A.A., Mei P.R.** (2004), Austenite transformation and age hardening of HSLA-80 and ULCB steels, *Journal of Materials Processing Technology*, Vol. 155–156, 1513–1518.
4. **Lacroix G., Pardoen T., Jacques P.J.** (2008), The fracture toughness of TRIP-assisted multiphase steels, *Acta Materialia*, Vol. 56, 3711-4124.
5. **Ma C., Chen D.L., Bhole S.D., Boudreau G.** (2008), Microstructure and fracture characteristics of spot-welded DP600 steel, *Materials Science and Engineering*, Vol. 485, 334-346.
6. **Mucha J., Kaščák Ľ., Spišák E.** (2011), Joining the car-body sheets using clinching process with various thickness and mechanical property arrangements, *Archives of civil and mechanical engineering*, Vol.11, No. 1, 135-148.
7. **Saleh M.H., Priestner R.** (2001), Retained austenite in dual-phase silicon steels and its effect on mechanical properties, *Journal of Materials Processing Technology*, Vol. 113, 587–593.
8. **Sevim I.** (2006), Effect of hardness to fracture toughness for spot welded steel sheets, *Material and Design*, Vol. 27, 21-30.
9. **Show B.K., Veerababu R., Balamuralikrishnan R., Malakondaiah G.** (2010), Effect of vanadium and titanium modification on the microstructure and mechanical properties of a microalloyed HSLA steel, *Materials Science and Engineering*, Vol. 527, 1595-1604.
10. **Sierra R., Nemes J.A.** (2008), Investigation of the mechanical behavior of multi-phase TRIP steels using finite element methods, *International Journal of Mechanical Sciences*, Vol. 50, 649-665.
11. **Spišák E., Kaščák Ľ., Viňáš J.** (2011), Research into properties of joints of combined materials made by resistance spot welding, *Chemické listy*, No. 16, 488-490.
12. **Tumuluru M.D.** (2006), Resistance spot welding of coated high-strength dualphase steels, *Welding Journal*, No. 8, 31–37.
13. **Vural M., Akkus A.** (2004), On the resistance spot weldability of galvanized interstitial free steel sheets with austenitic stainless steel sheets, *Journal of Materials Processing Technology*, Vol. 153-154, 1-6.
14. **Williams N.T., Parker J.D.** (2004), Modelling and control of weld nugget formation, *International Material Review*, No. 2, 45-75.
15. **Zhang H., Senkara J.** (2006), Resistance welding: Fundamentals and Applications, Taylor & Francis, New York.

Acknowledgment: Authors are grateful for the support of experimental works by project APVV-0682-11: “Application of progressive tool coatings for increasing the effectiveness and productivity of forming sheets made of modern materials”.

JOINING THE COMBINATION OF AHSS STEEL AND HSLA STEEL BY RESISTANCE SPOT WELDING

Ľuboš KAŠČÁK*, Emil SPIŠÁK*, Ivan GAJDOŠ*

*Faculty of Mechanical Engineering, Department of Technology and Materials, Technical University of Košice, Letná 9, 04200 Košice, Slovakia

lubos.kascak@tuke.sk, emil.spisak@tuke.sk, ivan.gajdos@tuke.sk

Abstract: The paper deals with the optimization of parameters of resistance spot welding and quality analysis of welded joints made by combination of galvanized Advanced High Strength Steel and High Strength Low Alloy steel. It is an advanced material combination utilized in automotive industry to reduce weight of the vehicle body and consequently lowering the fuel consumption to achieve the lowest possible fuel consumption, high active and passive safety of passengers while decreasing the amount of emission. The quality of welded joints was evaluated by destructive tests and non-destructive tests. The shear tensile test according to STN 05 1122 standard was used. Some samples were prepared for metallographic analysis, where the influence of the welding parameters on the structure of welded joint and occurrence of pores in the weld metal caused by evaporation of zinc from the coating was observed.

Key words: Car Body Sheets, Spot Welding, Tensile Test, Microhardness

1. INTRODUCTION

In resistance spot welding, the weld is made by a combination of heat, pressure and time. This technique is commonly used in automotive industry due to its high efficiency in manufacturing thin metal sheets. A wide variety of metal sheets up to 3 mm thickness can be handled by the resistance spot welding method (Sevim, 2006; Spišák et al., 2011). In the last decade a change in body shell mass production has occurred in the automotive industry. In answer to the intensifying energy crisis and in order to meet customer requirements for automobiles such as weight reduction for energy saving and enhancement of passenger safety, new materials, e.g. advanced high strength steels (AHSS) have to be applied (Brauser, 2010; Mucha et al., 2011). These materials are gaining in popularity due to their high strength in combination with good ductility characteristics compared to traditional high strength steels, for example micro-alloyed steels (Tumuluru, 2006). An important AHSS representative is the so-called TRIP (Transformation Induced Plasticity) steel dominated by a ferrite matrix with retained austenite, bainite and martensite as dispersed phases, offering excellent mechanical properties due to the transformation of retained austenite into martensite during plastic straining (Lacroix, 2008). As a result, both strength and uniform strain increase owing to the appearance of a harder phase and to the additional local plastic yielding of the surrounding grains related to the transformation strain as was described in (Saleh and Priestner, 2001). The TRIP effect, which is exhibited by such materials, is characterized by the phenomenon known as strain-induced martensitic transformation (SIMT). Due to the onset of plastic straining, the retained austenite undergoes SIMT which enhances the work hardenability of such steels due to the transformation of the austenite phase to the much harder martensite phase. This brings about a resistance to local necking which explains the uniform elongation and enhanced formability observed in such steels (Sierra and Nemes, 2008).

The challenge of using the coated AHSS steels in the industry is that they are readily inclined to exhibit expulsion during the spot welding. As well, the presence of the coating results in the accelerated degradation of the welding electrodes, leading to earlier expulsion and frequent replacement or re-dressing of the electrodes (Ma et al., 2008; Williams and Parker, 2004).

HSLA steel is well-known type of steel alloy that provides many benefits over regular steel alloys. In general, HSLA alloys are much stronger and tougher than ordinary plain carbon steels. HSLA steels are so called because they only contain a very small percentage of carbon. A typical HSLA steel may contain 0.15% carbon, 1.65% manganese and low levels (under 0.035%) of phosphorous and sulphur. Most HSLA steels are furnished in the as-hot-rolled condition with ferritic-pearlitic microstructure. The exceptions are the controlled-rolled steels with an acicular ferrite microstructure and the dual-phase steels with martensite dispersed in a matrix of polygonal ferrite. These two types of HSLA steels use the formation of eutectoid structures for strengthening, while the ferritic-pearlitic HSLA steels generally require strengthening of the ferrite. Pearlite is generally an undesirable strengthening agent in structural steels because it reduces impact toughness and requires higher carbon contents. Moreover, yield strength is largely unaffected by a higher pearlite content. The ferrite in HSLA steels is typically strengthened by grain refinement, precipitation hardening, and, to a lesser extent, solid-solution strengthening. Grain refinement is the most desirable strengthening mechanism because it improves not only strength but also toughness (Gorni and Mei, 2004; Fernándes et al., 2007; Show et al., 2010).

More cracks and failures tend to occur around welds, in the heat affected zone (HAZ), because the joints are exposed to dynamic and static loads in the automobile structures. After spot wedling, important changes occur in mechanical and metallurgical properties of the spot welded areas and heat affected zones (Vural and Akkus, 2001). The investigation of these changes is very important for the safety strength of the welded joints. In some parts of the modern automobiles, galvanized AHSS steels sheets and HSLA steels sheets are joined together with resistance spot welding technique. The paper evaluates joints of combined materials made by resistance spot welding the materials utilized in automotive industry in car body production.

2. EXPERIMANTAL PROCEDURE

The combination of dissimilar steel sheets were used for resistance spot welding: high strength low alloy steel H220PD with the thickness of 0.8 mm and advanced high strength steel TRIP 40/70+ Z100MBO with the thickness of 0.77 mm. Their basic mechanical properties and chemical composition are shown in Tab. 1 and Tab. 2.

Tab. 1. Basic mechanical properties of used steel sheets

Material	$Rp_{0.2}$ [MPa]	R_m [MPa]	A_{80} [%]	n_{90}
H220PD	238	382	36	0.228
TRIP40/70	450	766	26	0.278

Tab. 2. Chemical composition (wt%) of used steel sheets

Material	C	Mn	Si	Al	Cu	Ni
H220PD	0.012	0.435	0.119	0.041	0.040	0.013
TRIP40/70	0.141	1.627	0.185	1.986	0.053	0.016
Material	**Cr**	**Ti**	**V**	**Nb**	**Mo**	**P**
H220PD	0.046	0.033	0.012	0.052	0.009	0.057
TRIP40/70	0.056	0.007	0.017	0.037	0.024	0.046

The following tests were performed for evaluation of joints` properties: tension test, microhardnesses test and a metallographical analysis. The samples with dimensions of 40 x 90 mm and 30 mm lapping according to STN 05 1122 standard were used for the experiments (Fig. 1). Five samples were prepared for every combination of sheets. Resistance spot welding was carried out in laboratory conditions on a pneumatic spot welding-machine BPK 20 of VTS ELEKTRO Bratislava. CuCr welding electrodes were used according to ON 42 3039.71 standard. The diameter of working area of the electrode was d = ø5 mm.

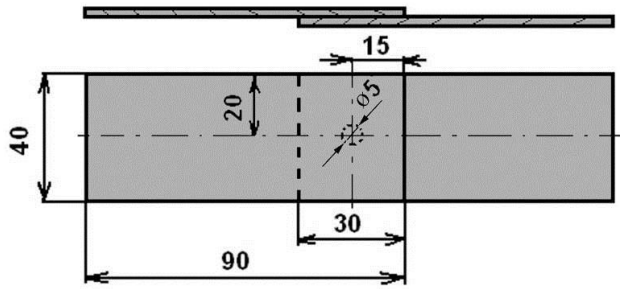

Fig. 1. Dimensions of sample for tensile test

Tab. 3. Welding parameters (I-wedling current, Fz-pressing force, T-welding time

Marking of sample	I [kA]	Fz [kN]	T [per.]	Weld diameter [mm]
A_5	5	6	10	Ø5
A_6	6	6	10	Ø5
A_7	7	6	10	Ø5
A_8	8	6	10	Ø5
A_9	9	6	10	Ø5

The used parameters of resistance spot welding for each sample including pressing force of electrodes Fz, welding time T and welding currents I are shown in Tab. 3. The samples were prepared by cutting against the direction of rolling. The surfaces of the samples were degreased in concentrated CH3COCH3.

The welding current is the most important parameter in resistance welding which determines the heat generation by a power of square as shown in the formula. The size of the weld nugget increases rapidly with increasing welding current, but too high current will result in expulsions and electrode deteriorations. The amount of weld current is controlled by two things: first, the setting of the transformer tap switch determines the maximum amount of weld current available; second, the percent of current control determines the percent of the available current to be used for making the weld. Low percent current settings are not normally recommended as this may impair the quality of the weld. The weld current should be kept as low as possible. When determining the current to be used, the current is gradually increased until weld spatter occurs between the metal sheets (Zhang and Senkara, 2006).

The carrying capacities of the spot welded joints were evaluated according to standard STN 05 1122 – Tension test of spot welded joints. This test was used for measuring the maximum carrying capacities Fmax of the joints. The test was carried out on the metal strength testing machine TIRAtest 2300 produced by VEB TIW Rauenstein, with the loading speed of 8 mm/min.

Further tests for quality evaluation of spot welded joints included the metallographical analysis. The quality of welded joints was evaluated by light microscopy on metallographical scratch patterns prepared according to ISO 6507-1 and ISO 6507-2 standards on Olympus TH 4-200 microscope.

3. RESULTS AND DISCUSSION

The values of carrying capacity of welded joints were in the range from 5224 N to 7496 N. Only one type of the joint occurs in all chosen parameters of welding – fusion welded joint. Measured values of carrying capacities of joints on welding current are shown in Fig. 2.

Dependency of carrying capacity of spot welds *Fmax* on welding current *I* can be expressed (calculation includes 5 samples for each current value):

$$Fmax = 401.49I + 3491 \quad (1)$$

with coefficient of determination R^2 = 0,8829

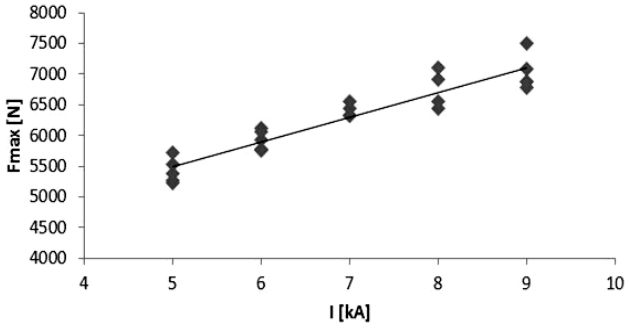

Fig. 2. Dependency of carrying capacities of spot welds Fmax [N] on welding current I [kA]

Tensile tests were executed under displacement control conditions on the specimen configurations in order to characterise the static behaviour of the joints and to estimate the ultimate tensile strength. The maximum shearing load was the most significant value obtained from the ''load-displacement'' curves as shown in Fig. 3 as well as the corresponding displacement. The form of the curves indicates the behaviour of the joints under loading, especially capacity for deformation. The measured values of carrying capacities of the spot welds are shown in Tab. 4.

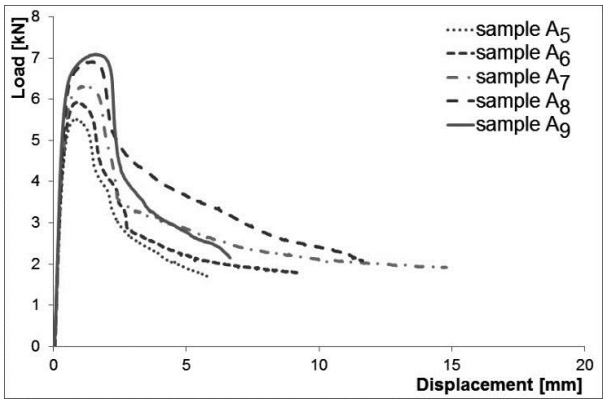

Fig. 3. Load-displacement curves and deformation of spot welded joints after tensile test

Tab. 3. Carrying capacities Fmax of the welds

Fmax [N]					
Sample No.	**A_5**	**A_6**	**A_7**	**A_8**	**A_9**
1	5263	5922	6335	6919	6978
2	5224	5763	6439	6758	7496
3	5383	5771	6562	6835	6982
4	5537	5921	6320	7098	6875
5	5520	6052	6322	6893	7090

The specimen failed partially through the periphery of the weld and partially through the base metal, which is confirmed in the failure mode of spot welded joints (Fig. 4) together with corresponding characteristic load vs. displacement curves generated in the experiments (Fig. 3). The carrying capacities of the samples are then influenced by the base metal strength.

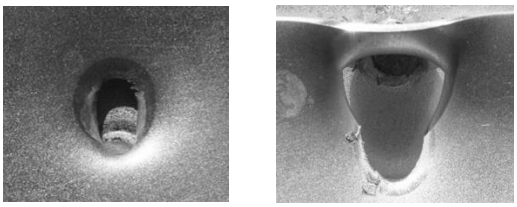

Fig. 4. Failures of spot welded joints of samples A_5 and A_9

Fig. 5 shows indentations formed by the welding electrodes. Changing the values of welding current influenced the welding electrode indentations on the surfaces of welded materials. The most obvious indentations were observed on the surfaces of samples prepared with the parameters of maximum value of welding current of 9 kA. The least obvious indentations were on the surfaces of both welded steels prepared with the minimum value of welding current of 5 kA.

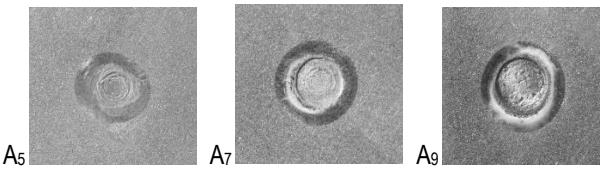

Fig. 5. Welding electrodes indentations of samples A_5 (I = 5kA), A_7 (I = 7 kA) and A_9 (I = 9 kA)

The metallographical analysis confirmed formation of fusion welded joints with characteristic areas of weld metal (WM), heat affected zone (HAZ) and base material (BM). Figure 6 shows the macrostructures of spot welded joints of samples A_5, A_7 and A_9.The size of spot welds increased with increasing values of welding current. The sample A_5 welded with the lowest value of welding current 5 kA shows the smallest weld nugget of all observed samples, with the narrow heat affected zone. The macrostructures of a weld joint show the solidification process of weld metal with a characteristic dendrite structure typical for resistance spot welds. The microscopic observation of macrostructures of the welds shows no pores and cavities occurring in the weld metal. The bigger weld nugget was observed in samples A_7, welded with the current of 7 kA. No pores and cavities occurring in the weld metal.

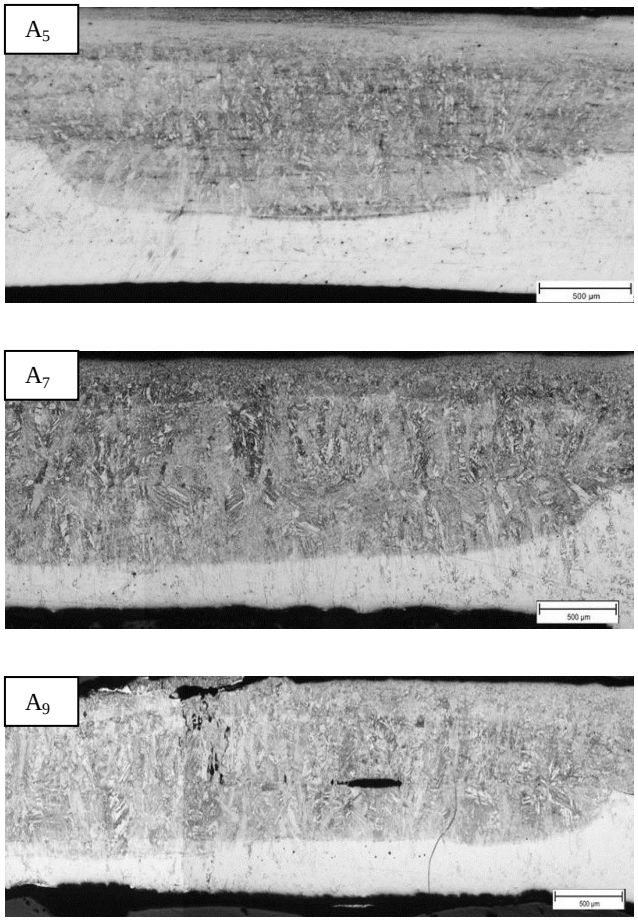

Fig. 6. Microstructures of the samples A_5, A_7 and A_9

The microstructure of weld metal consists of mostly fine-grained martensite arranged in typical lamellar formations form the side of TRIP steel. Such lamellar formations prevent the austenite from transformation; therefore the retained austenite occurs

in the microstructure. Besides martensite, also ferrite and both forms of bainite occur in the microstructure of weld metal. The microstructure of H220PD can be characterized as a fine-grained ferrite-pearlite structure. Because of heating in resistance spot welding, continual growth of grains towards the weld metal can be observed. A significant growth of pearlite grains occurs in the heat affected zone.

The sample A_9 welded with the highest values of welding current 9 kA shows the void and solidification cracks inside the biggest weld nugget. The formation of void in a spot weld is the result of nucleation and growth process during solidification of a liquid nugget after the heat source, i.e. electric current is shut off as was described in (Zhang and Senkara, 2006). The solidification cracking may form under certain condition. The cracks extended from the surface of a weld into its interior with some voids in the nugget. Such cracks may not reduce a joint`s strength if they are confined to the centre of the nugget. However, when they extend to the edges of weld nugget they can affect the weld quality.

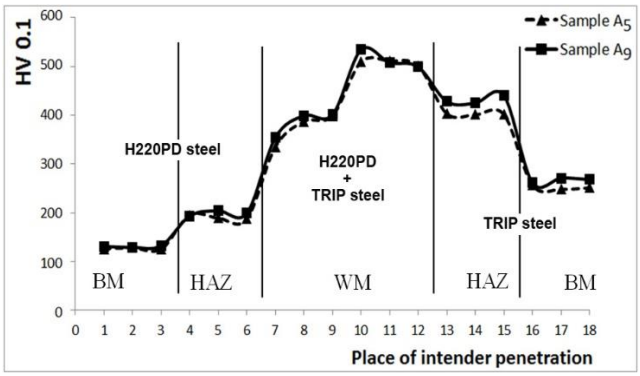

Fig. 7. The values of microstructures of samples A_5 and A_9 (BM-base material, HAZ-heat affected zone, WM-weld metal)

The measured values of microhardness are shown in Fig. 7. The measurements show the changes of the microhardness values in the areas of spot weld. The highest values were measured in the weld metal from TRIP side. The measurements show that increasing the parameters of resistance spot welding does not cause significant microhardness changes in the spot weld.

4. CONCLUSIONS

In this study, resistance spot welds of material combination of galvanized AHSS steels sheets and HSLA steels were evaluated.

On the basis of the conducted experiment, the following conclusions can be formed:

Fusion weld joints occur with all chosen parameters of resistance spot welding.

The highest tensile strength was observed in samples made with welding current of 9 kA. The average carrying capacity of samples was 7024 N. The lowest values of carrying capacity were observed in samples made with welding current of 5 kA, where the average value of carrying capacity decreased by 23 % in comparison to samples A9.

Linear dependence of carrying capacities of spot welds Fmax on welding current I was determined. Increasing values of welding current caused increasing of carrying capacity.

The metallographical analysis confirms that the chosen combination of advanced high strength steels and high strength low alloy steels is suitable for resistance spot welding. On the basis of the results it can be stated, that welding current has a determining influence on the weld joint. When using the welding current of 5 kA, weld joint was of high quality, fusible and without defects, but the weld nugget had smaller dimensions in comparison with other weld nuggets made with higher values of welding current. Welding current of 9 kA is not suitable for the examined thickness and sheet combination, because cracking was observed in the heat affected zone of multi-phase material of TRIP.

REFERENCES

1. **Brauser S., Pepke L.A., Weber G., Rethmeier M.** (2010), Deformation behaviour of spot-welded high strength steels for automotive appli-cations, *Materials Science and Engineering*, Vol. 527, 7099–7108.
2. **Fernández J., Illescas S., Guilemany J.M.** (2007), Effect of microalloying elements on the austenitic grain growth in low carbon HSLA steel, *Materials Letters*, Vol. 61, 2389-2392.
3. **Gorni A.A., Mei P.R.** (2004), Austenite transformation and age hardening of HSLA-80 and ULCB steels, *Journal of Materials Processing Technology*, Vol. 155–156, 1513–1518.
4. **Lacroix G., Pardoen T., Jacques P.J.** (2008), The fracture toughness of TRIP-assisted multiphase steels, *Acta Materialia*, Vol. 56, 3711-4124.
5. **Ma C., Chen D.L., Bhole S.D., Boudreau G.** (2008), Microstructure and fracture characteristics of spot-welded DP600 steel, *Materials Science and Engineering*, Vol. 485, 334-346.
6. **Mucha J., Kaščák Ľ., Spišák E.** (2011), Joining the car-body sheets using clinching process with various thickness and mechanical property arrangements, *Archives of civil and mechanical engineering*, Vol.11, No. 1, 135-148.
7. **Saleh M.H., Priestner R.** (2001), Retained austenite in dual-phase silicon steels and its effect on mechanical properties, *Journal of Materials Processing Technology*, Vol. 113, 587–593.
8. **Sevim I.** (2006), Effect of hardness to fracture toughness for spot welded steel sheets, *Material and Design*, Vol. 27, 21-30.
9. **Show B.K., Veerababu R., Balamuralikrishnan R., Malakondaiah G.** (2010), Effect of vanadium and titanium modification on the microstructure and mechanical properties of a microalloyed HSLA steel, *Materials Science and Engineering*, Vol. 527, 1595-1604.
10. **Sierra R., Nemes J.A.** (2008), Investigation of the mechanical behavior of multi-phase TRIP steels using finite element methods, *International Journal of Mechanical Sciences*, Vol. 50, 649-665.
11. **Spišák E., Kaščák Ľ., Viňáš J.** (2011), Research into properties of joints of combined materials made by resistance spot welding, *Chemické listy*, No. 16, 488-490.
12. **Tumuluru M.D.** (2006), Resistance spot welding of coated high-strength dualphase steels, *Welding Journal*, No. 8, 31–37.
13. **Vural M., Akkus A.** (2004), On the resistance spot weldability of galvanized interstitial free steel sheets with austenitic stainless steel sheets, *Journal of Materials Processing Technology*, Vol. 153-154, 1-6.
14. **Williams N.T., Parker J.D.** (2004), Modelling and control of weld nugget formation, *International Material Review*, No. 2, 45-75.
15. **Zhang H., Senkara J.** (2006), Resistance welding: Fundamentals and Applications, Taylor & Francis, New York.

Acknowledgment: Authors are grateful for the support of experimental works by project APVV-0682-11: “Application of progressive tool coatings for increasing the effectiveness and productivity of forming sheets made of modern materials”.

CLINCHRIVET AS AN ALTERNATIVE METHOD TO RESISTANCE SPOT WELDING

Ľuboš KAŠČÁK*, Emil SPIŠÁK*, Jacek MUCHA**

* Faculty of Mechanical Engineering, Department of Technology and Materials, Technical University of Košice, Letná 9, 042 00 Košice, Slovakia
**Faculty of Mechanical Engineering and Aeronautics, Department of Mechanical Engineering, University address Politechnika Rzeszowska, Al. Powstańców Warszawy 8, 35-959 Rzeszów, Poland

lubos.kascak@tuke.sk, emil.spisak@tuke.sk, j_mucha@prz.edu.pl

Abstract: Various materials are used in car body production which are not always possible to join by conventional joining methods such as resistance spot welding. Therefore ClinchRivet method seem to be possible alternative. The paper deals with evaluation of properties of the joints made by mechanical joining method – ClinchRivet. The joint is made with the using of a special rivet, which is pushed into the joined materials by the flat punch. Following materials were used for joining of this method: DX51D+Z and H220PD steel sheets. The tensile test for observing the carrying capacities and metallographicall analysis were used for the evaluation of joint properties. Some results of the tests of ClinchRivet joints were compared to the properties of the joints made by resistance spot welding.

Key words: Car Body Sheets, Spot Welding, Tensile Test, Microhardness

1. INTRODUCTION

The industry must meet the requirements for increased safety (product liability), the tightened regulations regarding environmental protection, as well as the requests of car drivers for more luxury features. Costly recall actions, ever increasing demands on the quality management, and the changing legal framework force the industry into an economic way of acting, especially with the harsh competitive conditions in the auto industry today (Barnes and Pashby, 2000; Buschke and Schappacher, 2006). One of the possibilities of decreasing the car weight and consequently lowering the fuel consumption is using various combinations of materials, such as combination of conventional deep-drawn steel sheet and high-strength steel sheet. Assembly and joining techniques must also be redesigned when adopting alternative materials (Mucha et al., 2011; Sun and Khaleel, 2005).

The increasing use of coated, lightweight and high-strength materials has led the automotive industry to re-examine traditional methods of component assembly. Direct welding of dissimilar sheet metals has proven to be difficult or impossible; thus, alternative joining techniques, such as mechanical fastening systems, have attracted increasing interest and applications. Mechanical fastening encompasses a broad range of methods, from threaded fasteners to different forms of rivets and mechanical interlocking methods (Mucha and Witkowski, 2013; Kaščák et al., 2010). Welding as the main joining technology in automotive industry offers unrivaled flexibility, but there are disadvantages such as processing time, fatigue weakness or thermal distortion. There are many joining technologies that are alternatives to resistance spot welding such as spot friction stir welding, adhesive bonding or new joining solutions including the plastic forming cold processes. The group of joints made of the native material with or without an additional fastener includes among the others the self-pierce riveting (SPR) joints, clinching joints and clinching joints with rivet. The main their disadvantage is lack of good double-side access for the joint forming tools. One of the alternative joining methods is the ClinchRivet process, which geometrically constrains two sheets by local deformation of the sheet metals using a punch and die, as well as the special rivet (Sevim, 2006; Szymczyk and Godzimirski, 2012).

The ClinchRivet is a cold process for joining two or more sheets by directly piercing the sheets with a special rivet. Since the ClinchRivet process does not require a pre-drilled hole unlike the conventional riveting, the joining speed is the same level with that of the spot resistance welding, and the equipment is similar (Abe, 2009; Johnson et al., 2009). The joint is formed by a rivet – Fig. 1. The punch, under the pressure conveyed by a hydraulic power device, pushes the rivet to penetrate into the top plate, and the die shape causes the rivet to flare within the lower sheet in order to form a mechanical interlock. This process therefore requires access to both sides of the joint (Kaščák et al. 2012). It is similar to Clinching process, which is used without any additional elements. Joining the steel sheets of DX51D and H220PD grades by Clinching method was described in (Kaščák and Spišák, 2012).

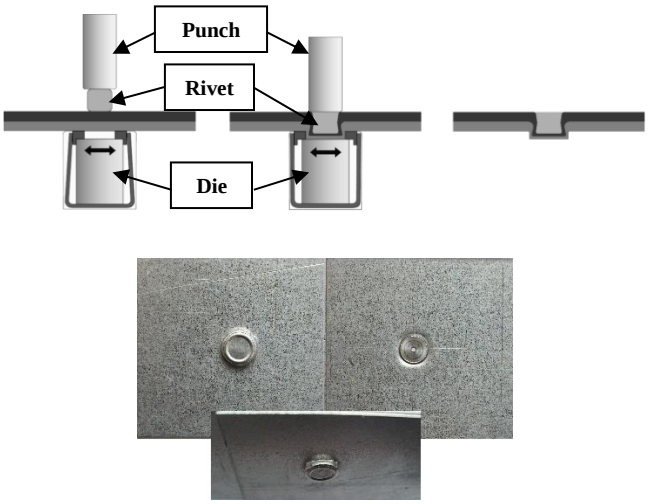

Fig. 1. Principle of ClinchRivet process

2. EXPERIMANTAL PROCEDURE

The following steel sheets were used for experimets: microalloyed steel HSLA H220PD with the thickness of 0.8 mm and deep-drawing grade steel DX51D+Z with the thickness of 0.9 mm. Basic mechanical properties and chemical composition of above mentioned materials are shown in Tab. 1 and Tab. 2. Mechanical properties of DX51D+Z steel were specified by producer.

Tab. 1. Basic mechanical properties of used steel sheets

Material	$Rp_{0.2}$ [MPa]	R_m [MPa]	A_{80} [%]	n_{90}
H220PD	238	382	36	0.228
DX51D+Z	155	270-500	23	0.24

Tab. 2. Chemical composition (wt%) of used steel sheets

Material	C	Mn	Si	Al	Cu	Ni
H220PD	0.012	0.435	0.119	0.041	0.040	0.013
DX51D+Z	0.064	0.178	0.016	0.120	0.041	0.002
Material	**Cr**	**Ti**	**V**	**Nb**	**Mo**	**P**
H220PD	0.046	0.033	0.012	0.052	0.009	0.057
DX51D+Z	0.023	0.002	0.005	0.015	0.004	0.016

In order to evaluate the properties of the ClinchRivet joints and resistance spot welded joints, the following tests were performed: tension test and metallographical analysis. All the samples with dimensions of 40 x 90 mm and 30 mm lapping according to STN 05 1122 standard were used for the experiments (Fig. 2). Six samples were prepared for both joining methods; one of them was left for metallographical analysis. It was not necessary to clean the sample surfaces before ClinchRivet joining. The ClinchRivet was carried out with the aluminium rivets (Fig. 3).

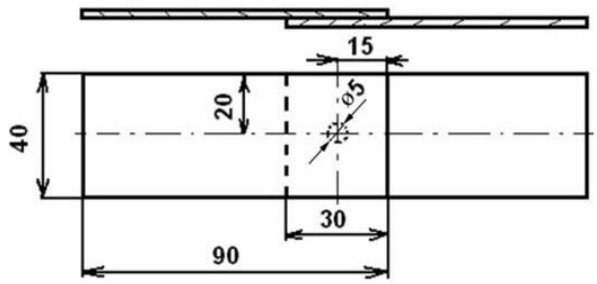

Fig. 2. Dimensions of the sample for tensile test

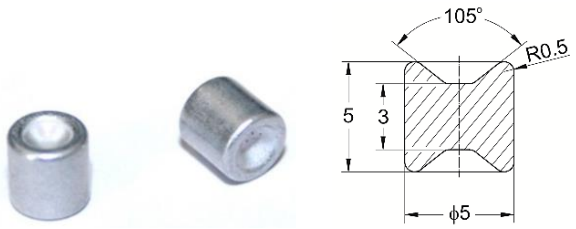

Fig. 3. Aluminium rivets for ClinchRivet method with dimensions

Resistance spot welding was carried out on a pneumatic spot welding-machine BPK 20 with the welding electrodes CuCr according to ON 42 3039.71 standard, where the diameter of ø5 mm of working area was used. The following parameters of resistance spot welding including pressing force of electrodes Fz, welding time T and welding current I were used:

Samples with H220PD steels: Fz = 3.2 kN, T = 12 cycles, I = 7.8 kA

Samples with DX51D+Z steels: Fz = 3 kN, T = 12 cycles, I = 7 kA

The parameters of resistance spot welding were determined according to the recommended welding parameters by IIW - International Institute of Welding and adapted to welding machine BPK 20. The surfaces of the samples for resistance spot welding were degreased in concentrated CH3COCH3.

The carrying capacities (Fmax) of the ClinchRivet joints as well as spot welded joints were measured according to standard STN 05 1122 - Welding: Tensile test on spot - and complete penetration welds. The test was carried out on the testing machine TIRAtest 2300 with the loading speed of 8 mm/min.

Further tests for quality evaluation of ClinchRivet joints and spot welded joints included the metallographical analysis. The quality of welded joints was evaluated by light microscopy on metallographical scratch patterns prepared according to ISO 6507-1 and ISO 6507-2 standards on Olympus TH 4-200 microscope.

3. RESULTS AND DISCUSSION

The measured values of carrying capacities of ClinchRivet (CR) joints and resistance spot welded (RSW) joints made by are shown in Tab. 3.

Tab. 3. Carrying capacities „Fmax" of CR joints and RSW joints

H220PD		DX51D+Z	
CR	**RSW**	**CR**	**RSW**
4952	5377	5020	7635
4820	5487	4695	7840
4703	5653	4667	7560
4763	5492	4554	6947
4725	5796	4911	7764

Tensile tests were executed under displacement control conditions on the specimen configurations in order to characterise the static behaviour of the joints. The maximum shearing load was the most significant value that was obtained from the "shear force-displacement" curves - Fig.4 and Fig.5. The form of the curves indicates the behaviour of the joints under loading. The shearing load is higher for RSW joints than for CR joints in all observed combinations of joined materials.

All observed samples of RSW joints had higher values of carrying capacities in comparison to CR joints. The carrying capacity values of CR joints were similar in cases of both tested materials. However, in case of RSW samples, there was a significant difference. The carrying capacity of DX51D+Z joints was approximately 2000 N higher than the carrying capacity of welds joining H220PD material.

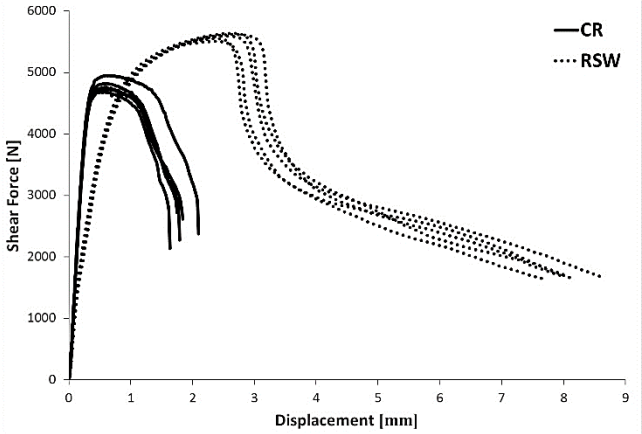

Fig. 4. Shear Force-displacement curves and deformation of the CR and RSW joints after tensile test with H220PD materials

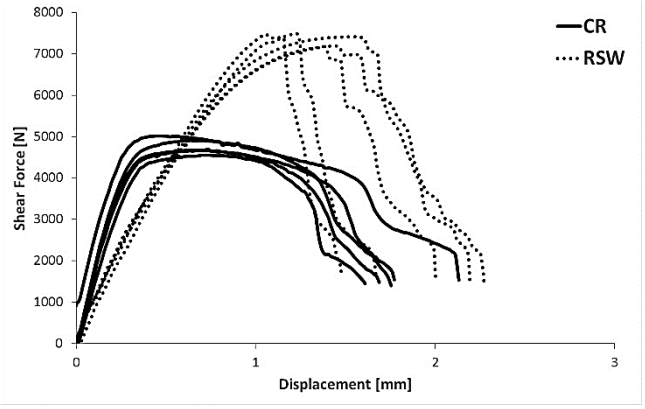

Fig. 5. Shear Force -displacement curves and deformation of the CR and RSW joints after tensile test with DX51D+Z materials

The average maximum shearing load of ClinchRivet joint was: for samples with H220PD material around 4900 N with the displacement about 0.5 mm and for samples with DX51D materials around 5000 N with the displacement about 0.5 mm. During the ClicnhRivet process the rivet and the riveted sheets undergo massive deformation to form the mechanical interlock. This energy is stored within the interlock leading to higher energy absorption.

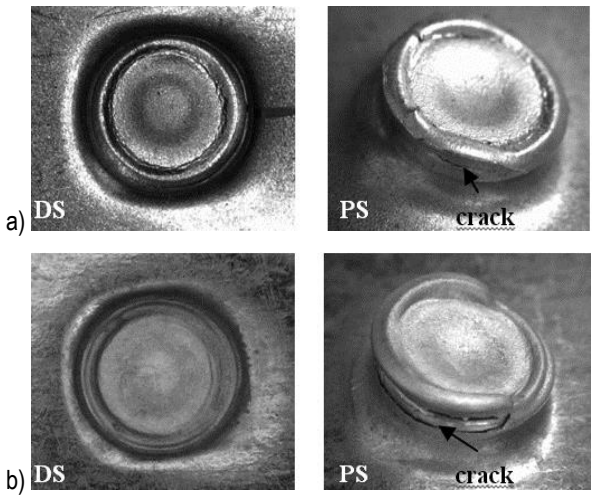

Fig. 6. ClinchRivet joints after tensile test: a) H220PD, b) DX51D+Z (DS – die side, PS – punch side)

Joints made by ClinchRivet method failed in the manner of a press-stud in combination with the mode of one edge of the joint fails. This method results in a loosening of the joint after quite small displacements. The upper sheet was then pull out form the joint with the significant crack in the critical area - failed at the neck. There is insufficient material in the neck of the joint, and loading will result in failure in the neck; excessive elongation in the region of the joint neck causing cracks formation – Fig. 6.

Metallographical analysis confirmed suitability of the ClinchRivet method for joining the observed materials. Using the rivet in this method led to significant hardening of the joint in the critical area (Fig. 7).

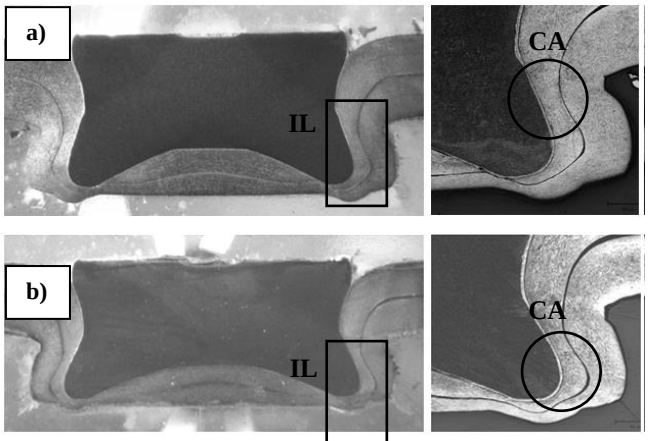

Fig. 7. ClinchRivet joints with interlocking and critical areas: a) H220PD, b) DX51D+Z (IL – interlocking, CA – critical area)

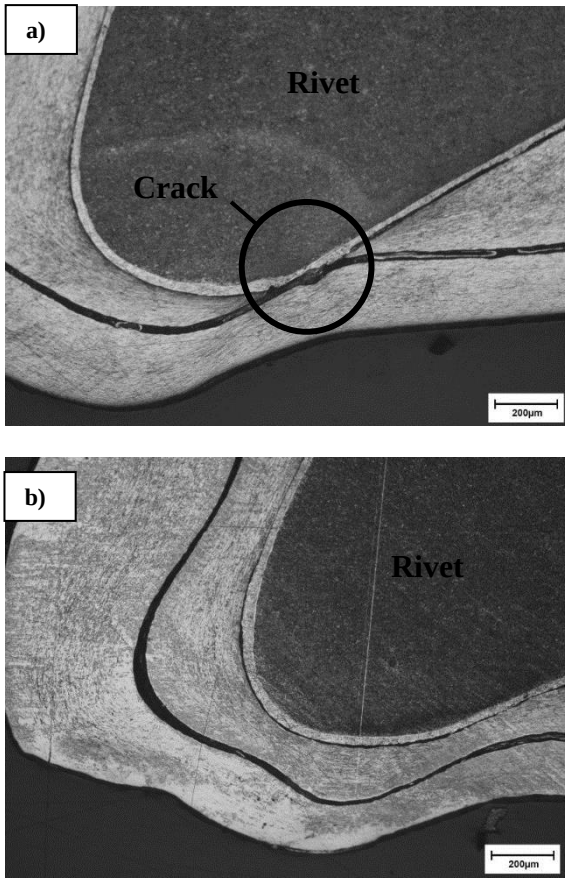

Fig. 8. Bottoms of the ClinchRivet joints: a) H220PD, b) DX51D+Z

Fig. 8 shows the place of the transition from the bottom of the ClinchRivet joint into the bulge on the bottom's edges of both joined materials. The crack in this area was observed on the upper sheet (from the side of the punch) when H220PD steel sheets were joined – Fig. 8a. The rivet bears a major part of the load, therefore the crack created during the joining process does not have as significant influence on the carrying capacity of the joint as in the case of the clinching, where no rivets are used.

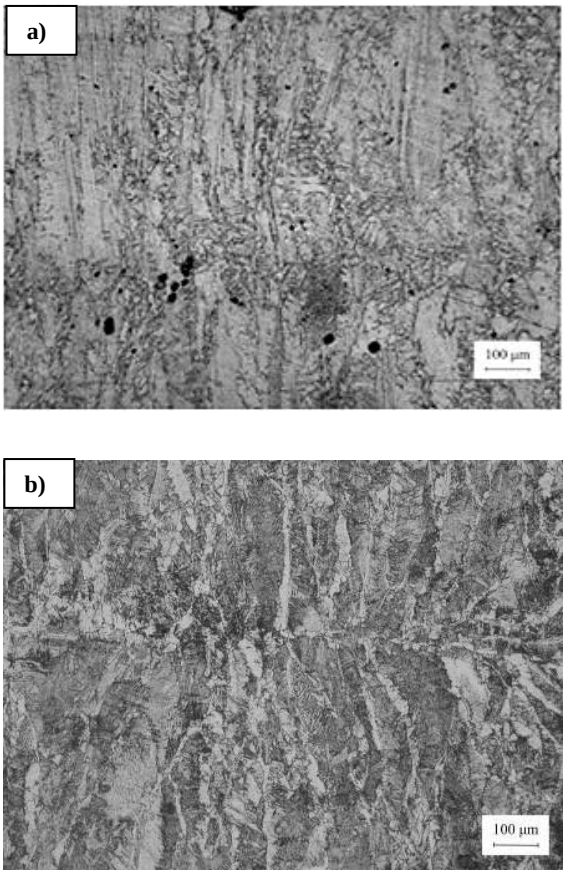

Fig. 9. Microstructures of welded materials in the area of weld nugget: a) H220PD, b) DX51D+Z

The metallographical analysis of resistance spot welded joints confirmed formation of fusion welded joints with characteristic areas of weld metal (WM), heat affected zone (HAZ) and base material (BM) – Fig. 9. The macrostructures show the solidification process of weld metal with a characteristic dendrite structure typical for resistance spot welds. No pores or cavities occurred in the weld metal of samples with DX51D materials. Some pores were observed in the area of weld nugget in the samples with H220PD materials as shown in Fig. 9a.

4. CONCLUSIONS

Although the high-speed mechanical fastening technique ClinchRivet is a young joining method, it has become more and more popular during the last decades. Most authors focus on the ClinchRivet process using steel rivets. The ClinchRivet using aluminium rivets is indeed a challenging task, since the strength of aluminium alloys are much weaker than that of steels. The aluminium rivet can be easily deformed when compressed into the plates, and hence no interlock is formed.

The ClinchRivet method using aluminium rivets is suitable for joining the tested materials. The carrying capacities of CR samples were sufficient and the metallographical analysis confirmed no occurrence of cracks or failures in the area of CR joints during joining process.

The main advantage of ClinchRivet technology is low running costs due to the fact that the processed components need not be heated. Only a die and a punch are used to press the sheet components to finish the whole joining process. The incomparable advantages of CR in practical production are as follows: no joining hot-stress has been produced, no poisonous gas has been given off, there is little noise in the process, the energy consumption is low, and this process leads to no damage to surface coating and does not require any premanufacturing of holes to the joined materials.

REFERENCES

1. **Abe Y., Kato T., Mori.** (2009), Self-piercing riveting of high tensile strength steel and aluminium alloy sheets using conventional rivet and die, *Journal of Materials Processing Technology*, Vol. 209, 3914–3922.
2. **Barnes T.A., Pashby I.R.** (2000), Joining techniques for aluminium spaceframes used in automobiles: Part II — adhesive bonding and mechanical fasteners, *Journal of Material Processing Technology*, Vol. 99, 72-79.
3. **Buschke P., Schappacher W.** (2006), Trends in the automotive industry steer new NDT applications, *ECNDT-Fr.1.6.2*, 1-12.
4. **Johnson P., Cullen J.D., Sharples L., Shaw A., Al-Shamma'a A.I.** (2009), Online visual measurement of self-pierce riveting systems to help determine the quality of the mechanical interlock, Measurement, Vol. 42, 661–667.
5. **Kaščák Ľ., Spišák E.** (2012), Clinching as a non-standard method for joining materials of dissimilar properties, *Zeszyty Naukowe Politechniki Rzeszowskiej: Mechanika*, Vol. 84, 31-41.
6. **Kaščák Ľ., Spišák E., Mucha J.** (2012), Evaluation of properties of joints made by clinching and self-piercing riveting methods, *Acta Metallurgica Slovaca*, Vol. 18, 172-180.
7. **Kaščák Ľ., Spišák E., Mucha J.** (2010), Joining of steel sheets for automotive industry using press joining method, *Zeszyty Naukowe Politechniki Rzeszowskiej*, No. 273, 121-126.
8. **Mucha J., Spišák E., Kaščák Ľ.** (2011), Non-standard car body element joining process with solid self-piercing rivet, *The Archives of Automotive Engineering*, Vol. 52, 57-67.
9. **Mucha J., Witkowski, W.** (2013), The experimental analysis of the double joint type change effect on the joint destruction process in uniaxial shearing test, *Thin-Walled Structures*, Vol. 66, 39-49.
10. **Sevim I.** (2006), Effect of hardness to fracture toughness for spot welded steel sheets, *Material and Design*, Vol. 27, 21-30.
11. **Sun X., Khaleel M.A.** (2005), Performance optimization of self-piercing rivets through analytical rivet strength estimation, *Journal of Manufacturing Processes*, Vol. 7, 83-93.
12. **Szymczyk E., Godzimirski, J.** (2012), The influence of riveting process on sheets fatigue life – the stress state analysis, *Acta Mechanica et Automatica*, Vol. 6, 74-81.

Acknowledgment: Authors are grateful for the support of experimental works by project VEGA No.1/0396/11: "Research and optimization of evaluation methods of strength and plastic properties of thin tinplates".

THIN-WALLED EPOXY-GLASS FIBRE BEAMS SUBJECTED TO PURE BENDING

Tomasz KUBIAK*, Zbigniew KOŁAKOWSKI*

*Mechanical Engineering Faculty, Department of Strength of Materials, Lodz University of Technology, ul. Stefanowskiego 1/15, 90-924 Lódź, Poland

tomasz.kubiak@p.lodz.pl, zbigniew.kolakowski@p.lodz.pl

Abstract: Buckling and postbuckling behaviour of thin-walled channel section beam made of epoxy-glass composite have been considered. The beams under analysis was subjected to pure bending. The main aim was check the influence of ply arrangement on buckling load and postbuckling behaviour and validate the authors analytical-numerical method by commercial finite element method software. Mentioned analytical-numerical method has been developed for more than 25 years in Department of Strength of Materials. This method uses asymptotic Koiter theory for conservative systems in the second order approximation modified by Byskov and Hutchinson. Additionally, using the finite element method software the influence of ply arrangement on failure load were checked.

Key words: Thin-Walled Structures, Composite Structures, Stability, Postbuckling Behaviour

1. INTRODUCTION

The thin-walled structure is a structure which consists of one or several thin plates or shells connected together at their common edges. Among thin-walled structures, plates, girders, beams, columns and shells are included. It is almost impossible to draw precisely the borderline between thin-walled elements and elements with average thickness. In the literature, one can find the information that the thin-walled rod is the one in which the wall thickness is at least 10 times smaller than the smallest cross-sectional dimension

Buckling and postbuckling of thin-walled structures subjected to static load have been investigated by many authors for more than one hundred years. The following scientists: Euler (1910), Timoshenko (1961) and Volmir (1967) should be included in the group of precursors of the investigations on stability of the thin-walled structure problem.

In the world wide literature, papers dealing with nonlinear problems of stability of thin-walled structures made of orthotropic materials can be found easily. The oldest work on this subject was published almost 80 years ago. Seydel (1933), Smith (1944) dealt with orthotropic plate buckling. Reissner and Stavsky (1961) published a study on the critical stress for anisotropic laminated plates with arbitrarily stacked layers. The theoretical background for buckling of composite and anisotropic plates was published by Lekhnitskii (1947), Ambartsumyan (1970), Ashton and Whitney (1970) or Vinson and Chon (1975). In the literature, there are many works on anisotropic plates – among them, March's (1942) and Thielmann's (1950) works are worth mentioning. Fraser and Miller (1970) established the critical load for orthotropic plates using the Ritz method. Mandell (1968) presented the results of experimental studies on buckling of anisotropic rectangular plates with simply supported or clamped edges. Chailleux et al. (1975) delivered the results of experimental studies on the stability of columns and square laminate plates. Noor (1975) in his work presented a comparison between the classical theory of plates, the theory of linear shear and a 3-D theory for elastic stability of orthotropic laminated plates. Chandra and Raju (1973) published a study on the postbuckling behaviour of orthotropic rectangular plates with simply supported edges. They analysed plates subjected to load causing uniform shortening of edges. They compared the results of their study with the previously published works. A similar problem was solved by Prahakara and Chia (1973). They carried out a theoretical analysis of the postbuckling behaviour of orthotropic, rectangular plates with simply supported edges and subjected to biaxial compression. To describe the deformation, a double Fourier series was used. Massey (1971) and Brunelle (1983) looked for areas of instability for orthotropic plates subjected to pure shear. Libove (1983) and Ting with co-authors (1987) analysed the unstable behaviour of orthotropic plates under biaxial load.

The employed analytical-numerical method, developed in Department of Strength of Materials of Lodz University of Technology, was presented in monograph edited by Kołakowski and Kowal-Michalska (1999). In mentioned above monograph the results of calculation for plates and beam-columns made of orthotropic materials can be found. The analysed structures are made of homogeneous orthotropic material. In contrast of that models in this publication layered composites were considered.

The latest work dealing with buckling and postbuckling behaviour of thin-walled columns made of epoxy-carbon composite subjected to compression was published by Dębski, Kubiak and Teter (2013). They compare finite element method, analytical-numerical method and experimental results. The beam-columns made of composite material subjected to bending can be found in paper written by Kołakowski and Mania (2013), who introduced the semi analytical method for determined the postbuckling behaviour of multilayered composite. The same method was also used in this paper.

Thin-walled structures especially made of composite materials have an ability to form freely the cross-section as well as a ply arrangement and, thus, to maximize strength and load carrying capacity. Therefore, they have been more and more often used in many industries for example they are used in sport and automotive industry and aerospace. As an example of such structural elements, a snowboard, a ski or poles can be mentioned, as well

as all kinds of crane girders, structural components of automobiles (a car body sheathing and all longitudinal members), aircraft fuselages and wings.

It should be remember that the thin-walled structures exhaust their carrying capacity not by exceeding allowable stresses but by a stability loss. Therefore, not only the critical load but also the postbuckling behaviour provides essential knowledge for designers.

The Authors of this paper decided to adapt previously developed analytical-numerical method to analyse postbuckling behaviour of thin-walled structures made of multilayered fibre composite. As an example of the considerations the multi-layer glass fibre composite channel section beam was taken. It was assumed that the beam is made of eight-ply laminate, where each can have different orientation but finally quasi-isotropic arrangement.

The main goal of the study was choosing a few ply arrangements that will be used in the samples (channel section profiles) to the experimental studies, that in turn will allow to validate the results of calculations.

The epoxy-glass fibre composite have been used as a material of considered thin-walled channel section beams subjected to pure bending. The buckling load and the postbuckling behaviour have been analysed.

2. METHODS OF SOLUTION

Two method of solution have been employed. The commercial software ANSYS® based on finite element method and analytical-numerical method. The results obtained by two mentioned above method was compared.

The finite element method commercial software (ANSYS®) was employed to validate the results obtained from analytical-numerical method.

The finite element method have been also used to determine the failure load.

2.1. Analytical-numerical method

The analytical-numerical method (Kolakowski and Kowal-Michalska 1999, 2012, Kubiak 2001) have been employed to analyse the static buckling, post buckling behaviour of thin-walled structures composed of plates made of orthotropic or composite materials.

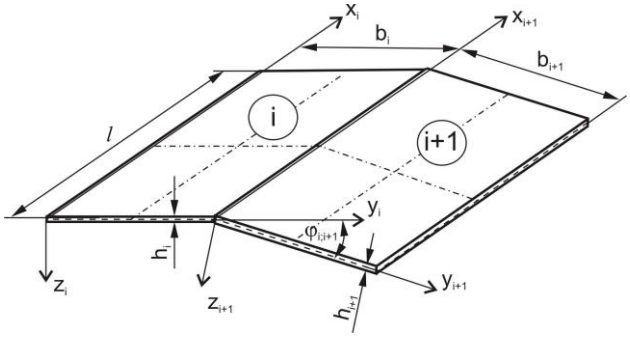

Fig. 1. Geometrical dimensions and local coordinate systems of adjacent plates

In the employed method the beams under analysis are simply supported at loaded ends. The beam's wall are rectangular and can be orthotropic with the principal axes of orthotropy parallel to the plate edges or have a quasi-isotropic ply arrangement. It was assumed that the considered beams are made of a material that governed by Hooks Law. The loaded edges remain straight and parallel during loading. Additionally, it is assumed that normal and shear forces disappear along the unloaded edges.

Thin-walled prismatic columns of a length l composed of rectangular plate segments (Fig. 1) interconnected along longitudinal edges are considered.

For the *i*-th plate component, precise geometrical relationships are assumed in order to enable the consideration of both out-of-plane and in-plane bending of each plate (Kolakowski, Kowal-Michalska 1999, 2012, Kubiak 2001):

$$\begin{aligned}
&\varepsilon_{ix} = u_{i,x} + \tfrac{1}{2}(w_{i,x}^2 + u_{i,x}^2 + v_{i,x}^2),\\
&\varepsilon_{iy} = v_{i,y} + \tfrac{1}{2}(w_{i,y}^2 + u_{i,y}^2 + v_{i,y}^2),\\
&2\varepsilon_{ixy} = \gamma_{ixy} = u_{i,y} + v_{i,x} + w_{i,x}w_{i,y} + u_{i,x}u_{i,y} + v_{i,x}v_{i,y},
\end{aligned} \tag{1}$$

where: u_i, v_i, w_i - displacement components of the middle surface of the *i*-th plate in the x_i, y_i, and z_i directions, correspondingly.

The differential equilibrium equations (2) have been obtained taking into account Lagrange's description, full Green's strain tensor for thin plates and Kirchhoff's stress tensor.

$$\begin{aligned}
&N_{xi,x} + N_{xyi,y} +\\
&+\left(N_{yi}u_{i,y}\right)_{,y} + \left(N_{xi}u_{i,x}\right)_{,x} + \left(N_{xyi}u_{i,x}\right)_{,y} + \left(N_{xyi}u_{i,y}\right)_{,x} = 0,\\
&N_{xyi,x} + N_{yi,y} +\\
&+\left(N_{xi}v_{i,x}\right)_{,x} + \left(N_{yi}v_{i,y}\right)_{,y} + \left(N_{xyi}v_{i,x}\right)_{,y} + \left(N_{xyi}v_{i,y}\right)_{,x} = 0,\\
&\left(N_{xi,x} + N_{xyi,y}\right)w_{i,x} + \left(N_{yi,y} + N_{xyi,x}\right)w_{i,y} + N_{xi}w_{i,xx} +\\
&+ N_{yi}w_{i,yy} + 2N_{xyi}w_{i,xy} + M_{xi,xx} + 2M_{xyi,xy} + M_{yi,yy} = 0,
\end{aligned} \tag{2}$$

where N and M are sectional forces and moments.

After expanding the fields of displacements **U** and the fields of sectional forces **N** into a power series with respect to the mode amplitudes ξ (the dimensionless amplitude of the buckling mode), Koiter's asymptotic theory has been employed (Koiter, 1976):

$$\begin{aligned}
&\mathbf{U}_i = \lambda\mathbf{U}_i^{(0)} + \xi\mathbf{U}_i^{(s)} + \xi^2\mathbf{U}_i^{(ss)} + ...\\
&\mathbf{N}_i = \lambda\mathbf{N}_i^{(0)} + \xi\mathbf{N}_i^{(s)} + \xi^2\mathbf{N}_i^{(ss)} + ...
\end{aligned} \tag{3}$$

where: λ is the load parameter; $\mathbf{U}^{(0)}$, $\mathbf{N}^{(0)}$ the pre-buckling state fields for *i*-th wall and $\mathbf{U}^{(s)}$, $\mathbf{N}^{(s)}$ the buckling mode fields, and $\mathbf{U}^{(ss)}$, $\mathbf{N}^{(ss)}$ are the post-buckling fields (the second order approximation) for the *i*-th plate. The non-linear problem was solved with the Byskov and Huchinson (1977) asymptotic theory application. By substituting displacements obtained from assumed expansion of the fields of displacements (3) into equations of equilibrium (2), the junction conditions and the boundary conditions, the boundary problems of zero, first and second order could be obtained. The first and second order approximations in the middle plate plane have been solved with a modified transition matrix method. The state vector at the final edge based on the state vector at the initial edge has been found by a numerical integration of differential equations (2) along the transverse direction using the Runge-Kutta formulae by means of the Godunov orthogonalization method. The above-mentioned method allows for finding the nonlinear

postbuckling coefficients a_{sss} and b_{ssss} applied in the equation describing the postbuckling equilibrium path (Kubiak 2001):

$$\left(1-\frac{\lambda}{\lambda_s}\right)\xi + a_{sss}\xi^2 + b_{ssss}\xi^3 + \ldots = \xi^* \frac{\lambda}{\lambda_s}; \tag{4}$$

where: λ_s is the critical load corresponding to the s-th mode and coefficient a_{sss}, b_{ssss} are:

$$a_{sss} = \frac{\boldsymbol{\sigma}^{(i)} * L_{11}(\mathbf{U}^{(s)}, \mathbf{U}^{(s)}) + 0.5\boldsymbol{\sigma}^{(s)} * L_{11}(\mathbf{U}^{(s)}, \mathbf{U}^{(s)})}{-\lambda_s \boldsymbol{\sigma}^{(0)} * L_2(\mathbf{U}^{(s)})},$$

$$b_{ssss} = \frac{2\boldsymbol{\sigma}^{(s)} * L_{11}(\mathbf{U}^{(ss)}, \mathbf{U}^{(s)}) + \boldsymbol{\sigma}^{(ss)} * L_{11}(\mathbf{U}^{(s)}, \mathbf{U}^{(s)})}{-\lambda_s \boldsymbol{\sigma}^{(0)} * L_2(\mathbf{U}^{(s)})}, \tag{5}$$

where: L_{11} is a bilinear operator, L_2 is a quadratic operator, and $\sigma^{(s)}$, $\sigma^{(ss)}$ are stress field tensors in the first and second order.
The postbuckling static equilibrium paths (4) for the lowest (s = 1) uncoupled buckling load $\lambda_s = \lambda_{cr}$ has the form:

$$\left(1-\frac{\lambda}{\lambda_{cr}}\right)\xi + a_{111}\xi^2 + b_{1111}\xi^3 = \xi^* \frac{\lambda}{\lambda_{cr}} \tag{6}$$

Till now in developed analytical-numerical method the second order approximation for multilayer composite plate or beams wall is not included. However, Kolakowski proposed the semi analytical method allowing to find coefficient b_{1111}, which according to (Kołakowski and Kowal-Michalska, 2012; Kołakowski and Mania 2013) is:

$$b_{1111} \approx \boldsymbol{\sigma}^{(11)} L_2\left(\mathbf{U}^{(1)}\right) + \frac{\lambda_{cr}\boldsymbol{\sigma}^{(0)} L_2\left(\mathbf{U}^{(1)}\right)}{2\boldsymbol{\sigma}^{(0)}\boldsymbol{\varepsilon}^{(0)}}. \tag{7}$$

2.2. Finite element method

The ANSYS® software based on finite element method was used to perform nonlinear buckling analysis and determine the postbuckling behaviour of channel sections beams subjected to pure bending.

To solve the nonlinear problem the iterative Newton-Raphson method is employed.

In numerical (FEM) model the four-node shell element with six degrees of freedom at each node have been taken to discretisation the considered channel section beam. The number of elements has been assumed on the basis of experience (e.g. Kolakowski and Kubiak, 2005) – the mesh density has been assumed in such a way as not to limit the deformation of the beam.

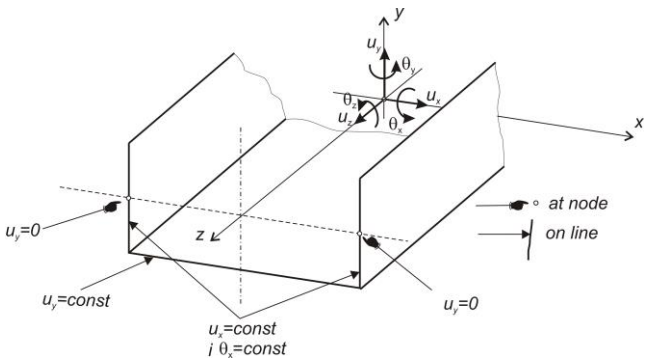

Fig. 2. Assumed boundary conditions

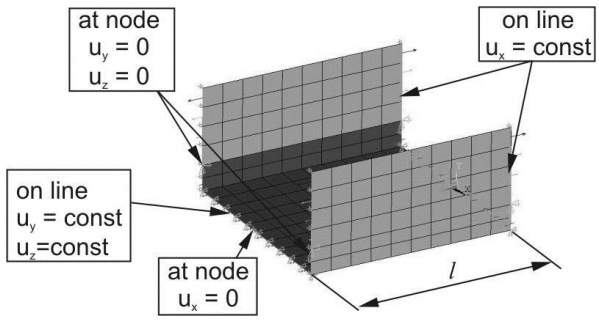

Fig. 3. Assumed boundary conditions

The assumed boundary conditions are presented in Figs. 2 and 3.

It was assumed that bending (the flexural buckling mode) occurred around the axis for which the second moment of area is the smallest, thus the FEM model was prepared in such a way that nodes in which the displacement in the y direction was set to zero were on the neutral axis of ending sections. Straightness of the loaded edges of the considered beam-column is provided by requiring equal displacements of all nodes lying on the edge of the beam-column in the direction normal to its walls. To ensure that deformations are compatible with the deflection in bending (the global flexural buckling mode), the edges normal to the neutral axis remained straight in the plane containing the wall of the column. In addition, for all nodes lying on those edges, the constant rotation around the axis parallel to the axis of the neutral section was presupposed.

The bending load was applied as a stress distribution, which was modelled in the form of the pressure distribution acting along the loaded edges of the structure (Fig. 4).

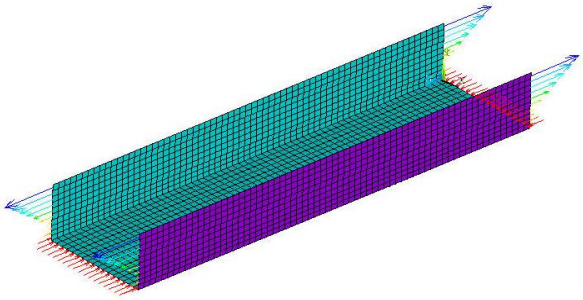

Fig. 4. Assumed FEM model of load

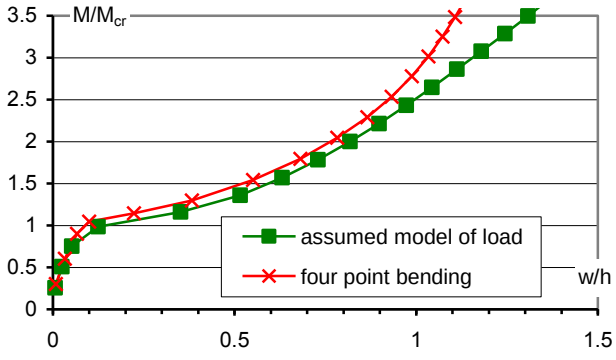

Fig. 5. Postbuckling equilibrium path for the channel section 50×25×1 beam of the length l = 200 mm

It should be noted that the assumed load is non-conservative – pressure is always perpendicular to the area to which it is applied – but for load which are less then two times the buckling load the differences in results can be neglected (Fig. 5).

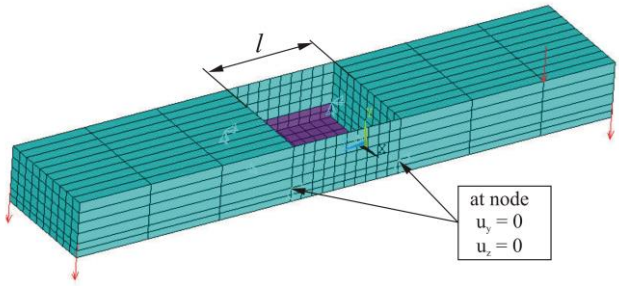

Fig. 6. FEM model for four point bending

The assumed FEM model for four point bending test is presented in Fig. 6.

3. RESULTS OF CALCULATIONS

The calculations have been performed using FEM and analytical-numerical method (ANM). The channel section composite beam (Fig. 7) with different ply arrangement and length l = 80 mm was considered. The following ply arrangement was taken into account:

- C1: $[0/-45/45/90]_S$;
- C2: $[90/-45/45/0]_S$;
- C3: $[90/0/90/0]_S$;
- C4: $[0/90/0/90]_S$;
- C5: $[45/-45/45/-45]_S$;
- C6: $[45/-45/45/0]_S$;
- C7: $[45/-45/90/0]_S$.

The initial geometrical imperfection amplitude equals 0.01 of wall thickness was assumed.

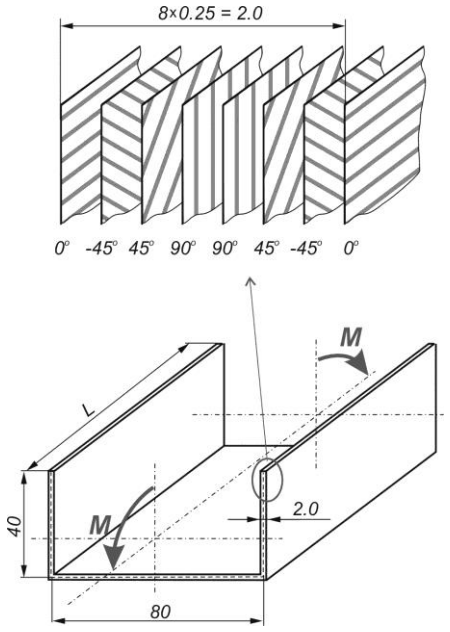

Fig. 7. Load, dimension and exemplary ply arrangement of considered channel section beam

The ply arrangement influence on buckling load and postbuckling behaviour have been analysed. The buckling loads comparison are presented in Tab. 1. The lengths L_{cr} of beams for which the lowest critical moment corresponding to local buckling and one half-wave in longitudinal direction have been calculated are also listed in Tab. 1. The buckling load obtained by two employed method are in very good agreement.

Tab. 1. Buckling load M_{cr} and critical length L_{cr} corresponding to local buckling mode

ply arrangements	ANM M_{cr} [kNm]	FEM M_{cr} [kNm]	length of one half-wave L_{cr} [mm]
C1: $[0/-45/45/90]_S$	6.2	6.2	80
C2: $[90/-45/45/0]_S$	6.3	6.2	52
C3: $[90/0/90/0]_S$	6.2	6.2	67
C4: $[0/90/0/90]_S$	6.1	6.1	71
C5: $[45/-45/45/-45]_S$	6.9	7.2	63
C6: $[45/-45/45/0]_S$	6.9	7.1	63
C7: $[45/-45/90/0]_S$	6.9	7.2	60

The postbuckling equilibrium paths obtained with analytical-numerical method are shown in Fig. 8. There are three groups of ply arrangements (1st: C2 and C3; 2nd: C4, C6 and C7; 3rd: C1 and C5) and in each of these the course of equilibrium paths are similar. Taking above into account further calculation was made for ply arrangement denoted as C1, C2 and C4.

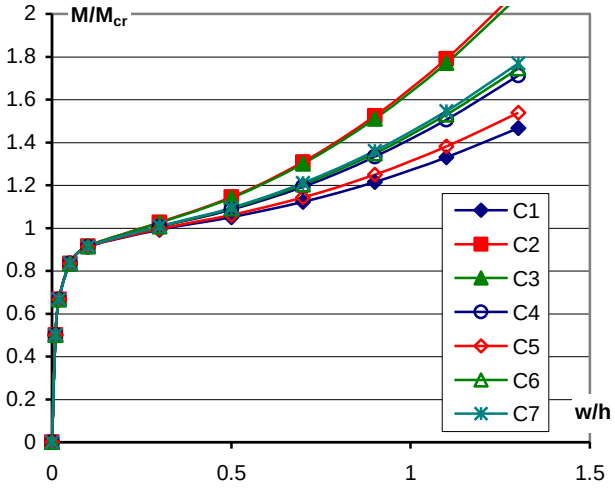

Fig. 8. Postbuckling equilibrium paths for channel section beam with different ply arrangement

The comparison of courses of postbuckling equilibrium paths for different ply arrangement denoted by C1, C2 and C4 obtained with FEM and ANM for beams of length L = 80 mm are presented in Fig. 9. The differences in dimensionless load M/M_{cr} for given dimensionless deflection w/h = 1 reach as much as 20% for beams with ply arrangement C2. These differences growing with increasing dimensionless deflection w/h. Taking above into account and knowing that the Koiter approach does not take into account stiffening the structure associated with the fact that part of the section is tensed it was decide to check the influence of ten-

sile stress on beam stiffness - checking the change of course of postbuckling paths. The differences depending on approach are presented in Fig. 10.

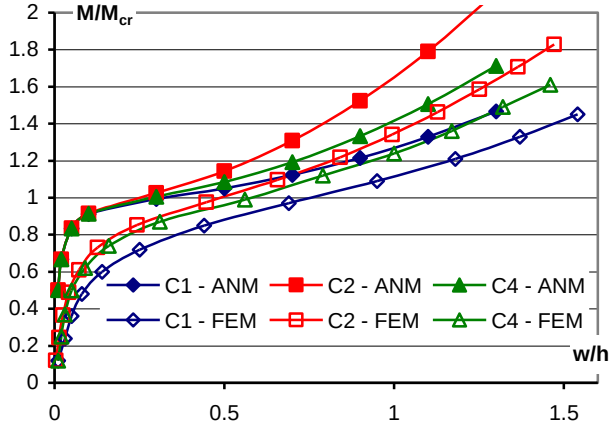

Fig. 9. FEM and ANM results comparison for channel section beam with different ply arrangement

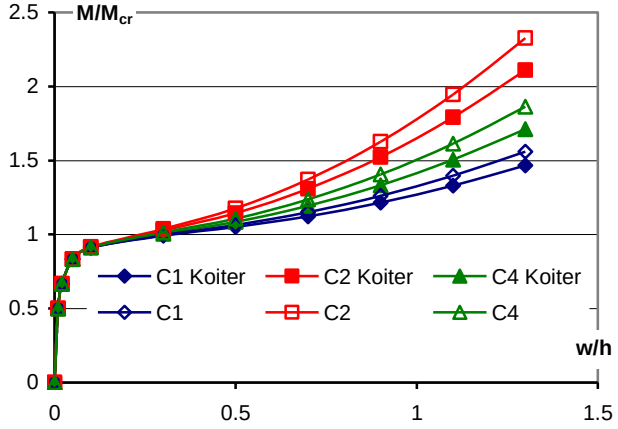

Fig. 10. Postbuckling equilibrium paths obtained with Koiter or authors approach

Taking into account the stiffening beams caused by sectional tension forces the differences between results obtained with analytical-numerical method and finite element method are greater than presented in Fig. 9 - the results comparison for beam of length L = 150 mm with layers arrangement C2 are shown in Fig. 11. First of all it should be noted that the results obtained with analytical-numerical method correspond to local buckling, so for easier comparison the curve denoted by "FEM local" was obtained for beam with length $L = L_{cr}$ = 52mm (see Tab.1). The beam deflection corresponding to local and global buckling mode and obtained for dimensionless load M/M_{cr} = 2.4 are presented in Fig. 12.

As it is presented in Fig. 13 the postbuckling equilibrium paths depend not only on the length of the beam but also depend on the chosen point in which the displacement for increasing load are collected. The curve denoted by number from 1 to 3 correspond to point presented in Fig. 12 in which the displacements are measured.

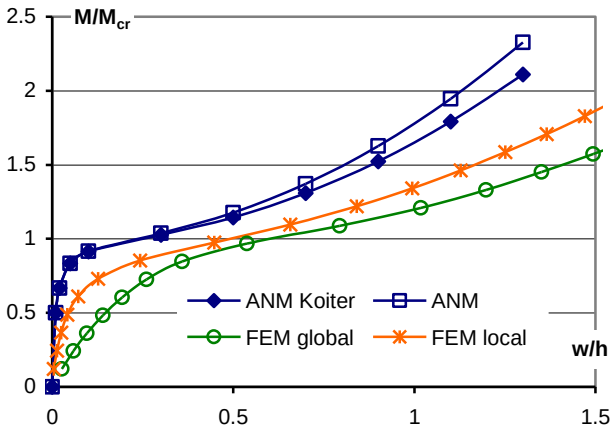

Fig. 11. Postbuckling equilibrium paths for channel section beam with ply arrangement C2 obtained with ANM and FEM

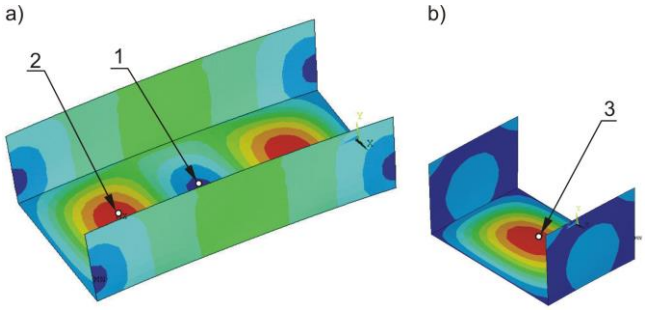

Fig. 12. Deflection obtained with FEM for beam of length L =150 mm corresponding to global mode (a) and for beam with L =52 mm corresponding local mode (b)

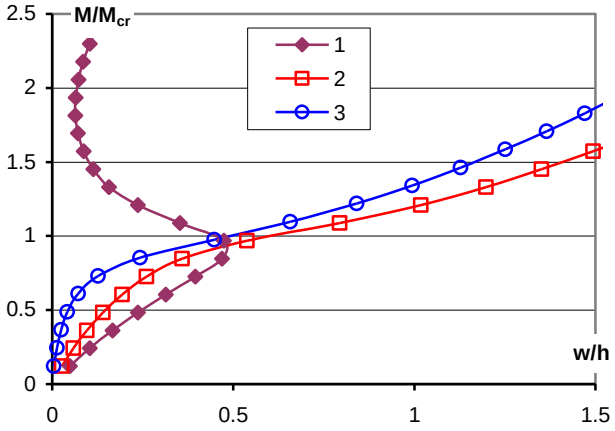

Fig. 13. Comparison postbuckling equilibrium paths for channel section beam with ply arrangement C2 obtained with FEM

Observing the coarse of the postbuckling equilibrium paths, especially the curve denoted by 1 (Fig. 13) it can be said that considered beam are bended – edge does not remain straight. Displacement of point 1 (Fig. 12) are in opposite direction than the edge of the channel section. When the displacement measured on the middle of the web (point 1 in Fig 12a) starts grows the collected displacement decrease for increasing load (curve 1 - Fig. 13) – it happens for load corresponding to buckling load M/M_{cr} = 0.9 for channel section beam with geometrical imperfection.

4. CONCLUSIONS

The results of calculation obtained using employed methods differ even about 20%. Such a big differences shows that the experimental tests are necessary for numerical model validation.

The results show that the critical load for all analysed beams are similar, and their behaviour after the loss of stability depends strongly on the layers arrangement.

Differences in the results obtained with both employed methods depend on assumptions and because the prebuckling bending have not been taken into account in the analytical-numerical method.

The one of the aims of presented investigation was to choose the ply arrangement of produced channel sections samples which will be used in experimental tests.

The results of calculations for beams with seven different ply arrangements shows, that is enough to choose only three of them for which the postbuckling equilibrium paths differ in the most.

REFERENCES

1. **Ambartsumyan S.A.** (1970), *Theory of anisotropic plates*, Technomic.
2. **Ashton J.E., Whitney J.M.** (1970), *Theory of Laminated plates*, Technomic.
3. **Bernoulli J., Euler L.** (1910), *Abhandlungen uber das Gleichegewicht und die Schwingungen der Ebenen Elastischen Kurven*, Wilhelm Engelmann, 175, Leipzig.
4. **Brunelle E.J., Oyibo G.A.** (1983), Generic buckling curves for specially orthotropic rectangular plates, *AIAA* 21, 8, 1150-115.
5. **Byskov E., Hutchinson J. W.** (1977), Mode interaction in axially stiffened cylindrical shells, *AIAA* 15(7), 941-948
6. **Chailleux A., Hans Y., Verchery G.** (1975), Experimental study of the buckling of laminated composite columns and plates*, Int. J. Mechanical Science* 17, 489–498.
7. **Chandra R., Raju B.** (1973), Postbuckling analysis for rectangular orthotropic plates, *Int. J of Mechanical Science* 16, 81–97.
8. **Dębski H., Kubiak T., Teter A.** (2013), Buckling and postbuckling behaviour of thin-walled composite channel section column, *Composite Structures* 100, 195–204
9. **Fraser Jr., H.R., Miller R.E.** (1970), Bifurcation type of buckling of generally orthotropic clamped plates, *AIAA* 8, 4, 707-712.
10. **Gupta R.K., Rao K.P.** (1985), Instability of laminated composite thin-walled open-section beams, *Composite Materials* 4, 299–313.
11. **Koiter W.T.** (1976), *General theory of mode interaction in stiffened plate and shell structures*, WTHD, Report 590, Delf.
12. **Kołakowski Z., Kowal-Michalska K. (eds),** (1999), *Selected problems of instabilities in composite structures* A series of monographes, Technical University of Lodz Press.
13. **Kolakowski Z., Kubiak T.** (2005), Load-carrying capacity of thin-walled composite structures, *Composite Structures* 67, 417–426.
14. **Kolakowski Z., Kowal-Michalska K. (eds),** (2012), *Static, dynamic and stability of structures, Vol. 2, Statics, dynamics and stability of structural elements and systems*, A series of monographs, Technical University of Lodz Press, Lodz.
15. **Kolakowski Z., Mania R.J.** (2013), Semi analytical method versus the FEM for analysis of the local post-buckling of thin-walled composite structure, *Composite Structures* 97, 99–106.
16. **Kubiak T.** (2001), Postbuckling behavior of thin-walled girders with orthotropy varying widthwise*, Int. J. Solid and Structures* 38, 28–29, 4839–4856.
17. **Lekhnitskii S.** (1947), *Anisotropnyje plastinki*, Moscow-Leningrad.
18. **Libove C.**, (1983), Buckle pattern of biaxially compressed simply supported orthotropic plates, *Jnt. of Comp. Materials* 17, 45-48.
19. **Mandell J.M.** (1968), *An experimental study of the postbuckling of anisotropic plates*, M.S. thesis, Case Western Reserve University.
20. **March H.** (1942), *Buckling of flat plywood plates in compression, shear or combined compression and shear, Forest Products Laboratory*, Rep. 1316.
21. **Massey C.** (1971), The elastic buckling of orthotropic rectangular plates, *Civ. Eng. Trans.* CE13, 1, 63-65.
22. **Noor A.K.** (1975), Stability of multilayered composite plates, *Fibre Science and Technology* 8, 81–89.
23. **Prahakara M.K. Chia C.Y.** (1973), Postbuckling behaviour of rectangular orthotropic plates, *Jnl. Mech. Eng. Sci.* 17, 25-33.
24. **Reissner. E., Stavsky. Y.** (1961), Bending and stretching of certain types of heterogeneous aelotropic elastic plates*, Trans ASME Jnl. of Appl. Mech.* 9, 402-408.
25. **Seydel E.** (1933), *The critical shear load of rectangular plate*, NACA TM 705.
26. **Smith R.C.T.** (1944), The buckling of flat plywood plate in compression, *Australian Council for Aeonautics* Rep. 12.
27. **Thielemann W.** (1950), *Contributions to the problem of buckling of orthotropic plates with special reference to plywood*, NACA TM 1263.
28. **Timoshenko S.P., Gere J.M.** (1961), *Theory of elastic stability*, McGraw-Hill.
29. **Ting T.K. Surdenans J.** (1987), Buckling of rectangular orthotropic plates under biaxial loading, *Jnl of Comp. Materials*, 21, 124-128.
30. **Vinson J.R. Chou T.W.** (1975), *Composite Materials and their use in structures*, Applied Science Publisher Ltd.
31. **Volmir S.A.** (1967), *Stability of Deformation Systems*, Science, Moscow /in Russian/.

The paper has been written under research project financed by the National Centre for Science - decision No DEC-2011/03/B/ST8/06447.

AIR FLOW ANALYSIS FOR ELECTRICAL MOTOR'S COOLING SYSTEM WITH AUTODESK SIMULATION CFD 2013 PROGRAM

Jerzy MADEJ[*], Bartłomiej BĘDKOWSKI[**]

[*]Faculty of Mechanical Engineering and Computer Science, University of Bielsko-Biala, ul. Willowa 2, 43-309 Bielsko-Biała, Poland
[**]Institute Research & Development Centre of Electrical Machines "KOMEL", 188 Rożdzieńskiego Ave., 40-203 Katowice, Poland

juma@ath.bielsko.pl, b.bedkowski@komel.katowice.pl

Abstract: In the article the analysis of airflow through electrical motor was conducted and optimal design solution was chosen in order to increase cooling efficiency. Numerical simulations allow to determine the areas of temperature occurrence which may have destructive influence on electrical motor parts and on its safe operation. The numerical calculations of airflow was carried out for two different types of fans as well as for two different housings. An analysis of the construction was carried out by CFD method using Autodesk Simulation CFD 2013. Community results of the analysis, we can conclude that the better solution for machines with fixed direction of rotation is to use instead of the radial the axial fan. For axial fan the motor temperature in the same condition was lower by about 5°C.

Key words: Gas And Thermal Flow Analysis, Electrical Motors, Cooling Systems, CFD

1. INTRODUCTION

The modern design studies demand higher efficiency and miniaturization of electrical motors at low production costs. Mechanical and electrical losses and efficiency of these types of devices are directly connected with operation temperature, and these values decide about technical and economical indexes of electrical machines.

The use of elements sensitive to high temperature such as permanent magnets, encoders, seal or bearings as well as growing variety of operating conditions are the main causes for giving more attention to the phenomenon of flow and heat transfer and implementing such constructions, which will ensure optimal machine operation. Hence, it is important to find the nature of the flow phenomena that occurs in mechanical structures.

Making effective analyzes of heat transfer, gases and liquids flows around the device, and inside of it are now possible thanks to the use of specialized computing systems based on CFD algorithms, such analysis of electric machines we can find in the works of other authors (Będkowski and Madej, 2012; Boglietti et al., 2009; Chang et al., 2010; Dorrell et al., 2006; Hongmin, 2009, 2010; Lim et al., 2010; Szczypior and Jakubowski, 2009). The CFD analysis of impellers we can see in the works (Kelly and Gigas, 2003; Murthy et al., 2007). For this type of analysis The Autodesk Simulation CFD deserves attention.

2. PURPOSE AND SCOPE OF WORK

The purpose of this study was to calculate the parameters of the airflow, heat transfer and the cooling system efficiency of the electrical motor depending on the type of the fan and the changes made in the housing construction. The motor of the high of 80 mm and the power of 1 kW, operating at 1500 rpm speed was the object of discussion. The simplified model is shown in Fig. 1.

The view of exploded motor assembly with an indication of the parts' material uses for the calculation is shown in Fig. 2.

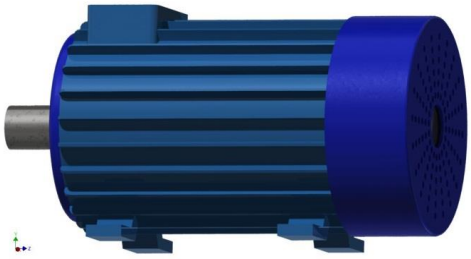

Fig. 1. The model of motor with short fan cover

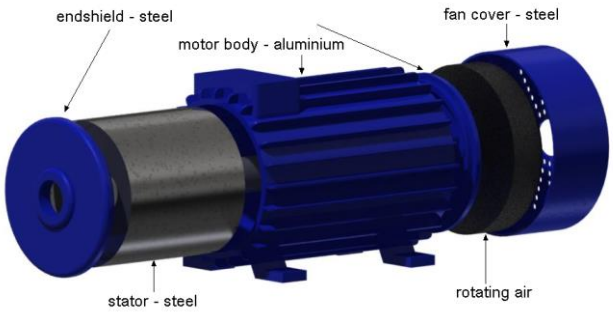

Fig. 2. The view of exploded motor assembly

It was assumed that the initial temperature of the ambient air of the motor is 20°C, and of the same, constant temperature is the air flowing into the fan case. It was also assumed that the only source of heat energy of 250W is the stator body. It includes the losses of iron ΔP_{Fe} and losses in the stator windings ΔP_{Cu} (from passage of current in the winding). The fan and bearings' mechanical losses and electrical losses in the rotor, which for perma-

nent magnet machines working with these rotational speeds are usually negligible, were omitted.

To assess efficient cooling, the two types of six blades fans' (shown in Fig. 3) calculations were performed.

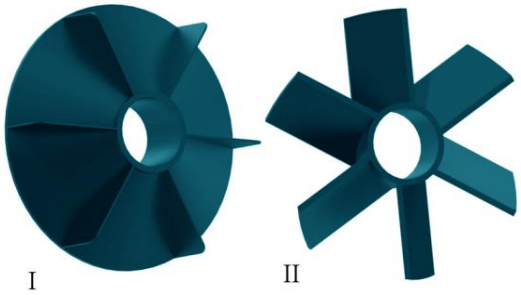

Fig. 3. Types of considered fans

3. NUMERICAL SIMULATIONS

The numerical calculations were made with Autodesk Simulation CFD 2013 program which is intended for flow and heat transfer analyzes. In this program, the simulation of the airflow from rotating fan was conducted as a transient analysis. This type of analysis requires time-consuming calculations and high computing power, but it has an important advantage - a continuous recording and presentation of the airflow distribution parameters at any time during study. It is of great importance for the subsequent experimental verification of obtained calculations.

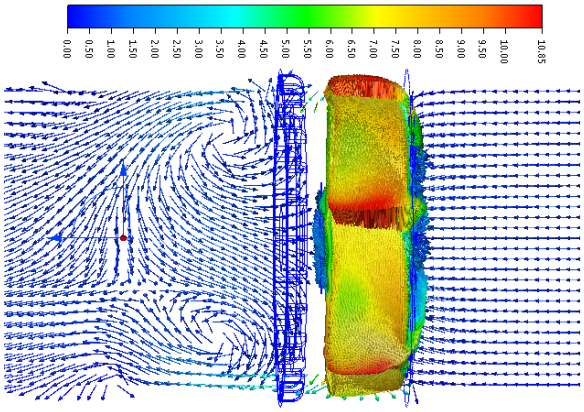

Fig. 4. The airflow view for fan I

Initial simulations revealed that in the complicated discrete model, simultaneous calculations of the airflow and heat transfer are practically impossible because of the problem with solution convergence.

Consequently, repeated attempts made to obtain stable solutions led to developing a two-step methodology for the calculation. In the first stage of the calculation, as a result of a transient analysis, fan volume flow rate parameters were obtained with the assumption about the flow resistance of the electrical motor cooling system.

The obtained results of the airflow for both types of the fans are shown in Fig. 4 and 5. The carried out calculations showed that the $5.5*10^6$ mm^3/s volume flow rates for first type of the fan and the $6.7*10^6$ mm^3/s for the second type of the fan were reached. These values were input data to the calculations carried out in the second phase. Steady State analyzes of cooling and airflow along motor body were included in the second stage.

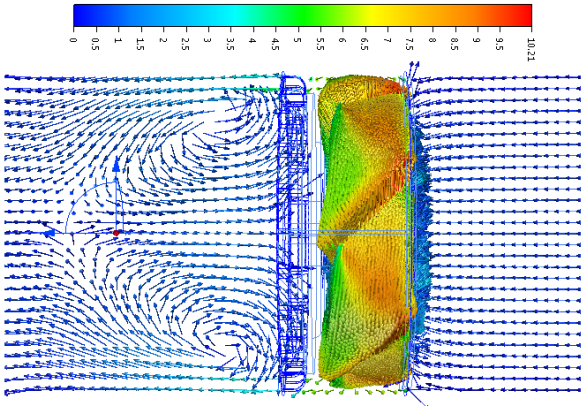

Fig. 5. The airflow view for fan II

3.1. The typical motor with short fan cover

As a result of the simulation performed in the second phase for the motor with short fan case (shown in Fig. 1), the airflow and temperature distribution with the use of both types of fans were obtained.

The vertical cross-section view of steady state airflow with velocity vectors along motor body is shown in Fig. 6.

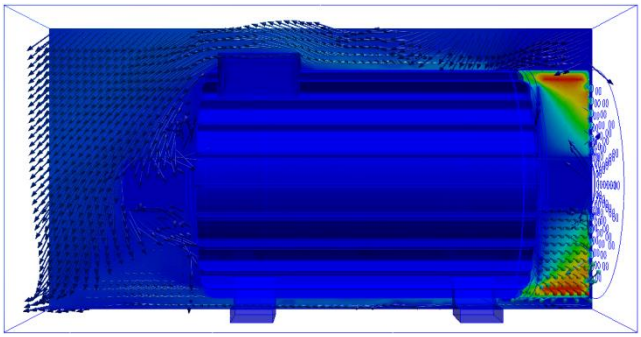

Fig. 6. The airflow with velocity vectors along motor body (vertical cross-section

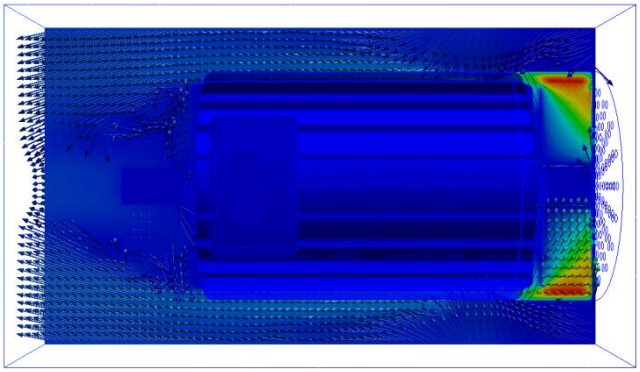

Fig. 7. The airflow with velocity vectors along motor body (horizontal cross-section)

Fig. 7 shows the airflow with velocity vectors along the motor body in the horizontal cross-section view.

The air flow pattern for both types of fans was the same. Only volume flow rate was different than one assumed for calculations. In accordance to the assumptions previously described for the second stage of the calculation.

While analyzing the obtained results, it can be seen that the cooling airflow at the fan's cover outlet is turbulent and along the body it is of low speed. Much of the airflow dissipates to the sides, which can affect the cooling efficiency.

The steady-state temperature distribution of electric motor for the first type of fan is shown in Fig. 8. The steady-state corresponds to 40 minutes of operation at full power, which was tested by solving a transient problem. The 76.3°C maximum temperature inside the motor was reached.

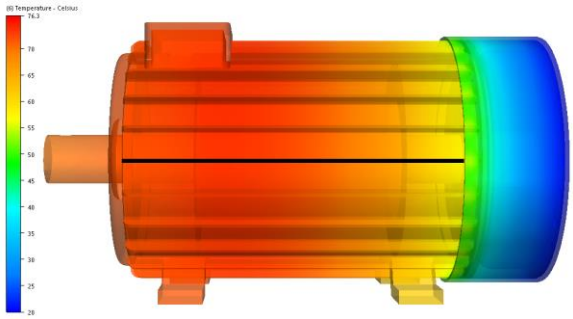

Fig. 8. The temperature profile of motor side

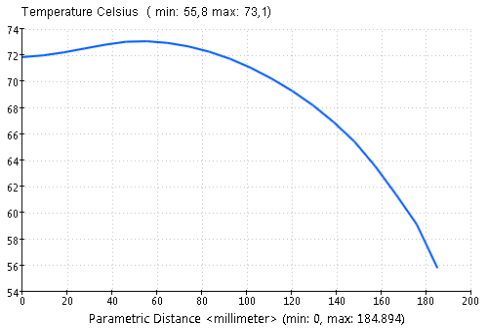

Fig. 9. The temperature diagram along cooling fin edge

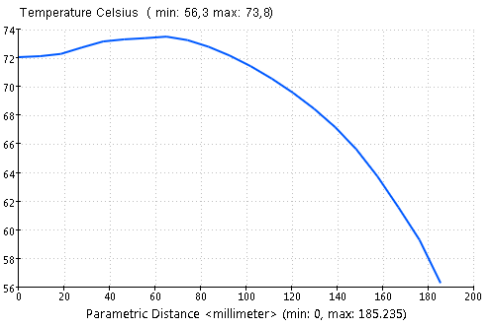

Fig. 10. The temperature diagram along cooling fin edge on the upper motor side

Fig. 9 shows the distribution of temperature registered along cooling fin edge highlighted in Fig. 8 in black. The maximum temperature reached at the fin edge was 73.1°C, the minimum temperature was 55.8°C.

Fig. 10 shows the analogous distribution of temperature along cooling fin edge on the upper motor side. Temperature difference was small. The maximum temperature was 73.8°C and the minimum temperature was 56.3°C.

For the second type of fan maximum temperature reached inside the motor was lower and reached 71.2°C. The maximum temperature reached at the fin edge (shown in Fig. 8) was 67.9°C, the minimum 51.3°C and in the upper part of the motor it respectively reached 68.2°C and 52.1°C (see tab.1).

Tab. 1. Compare temperatures for both fan types

	Fan I	**Fan II**
T_{max} [°C] for motor	76.3	71.2
T_{max} /T_{min} [°C] on radiator of the lateral motor side	73.1 / 55.8	67.9 / 51.3
T_{max}/T_{min} [°C] on radiator of the upper motor side	73.8 / 65.3	68.2 / 52.1

This data shows that the efficiency of the motor cooling fan depends on its geometry which seems to be a fairly obvious conclusion.

3.2. The motor with additional housing

Motor cooling efficiency depends on the fan built in it. It seems that lower motor temperature can be reached by the various design modifications. By directional airflow stream we can attain and increase the airflow speed along the motor body without changing the rotational parameters of the fan. The lengthening of the front of the motor body additional housing (Fig. 11) can be one of such proposals.

Fig. 11. The model of motor with additional housing

This modification compared to previous solutions caused a change in the structural character of the cooling airflow. The airflow character for motor with additional housing is shown In Fig. 12-13.

The airflow for the first type of fan caused an increase of the maximum temperature inside the motor. Compared to the previous solution which reached about 10°C (84°C - cf., Fig. 14) and for the second type of fan 6°C (76.9°C). Which has certainly negative effect on electric motor components.

However, the maximum temperature on the surface of the side of additional housing for the solution with first type of fan was 64.2°C, which was lower by about 9°C, and the minimum temperature was higher by 2°C as it was 57.9°C. On the top surface, the average rise of temperature was about 3°C (maximum 78.3°C, minimum 59.0°C).

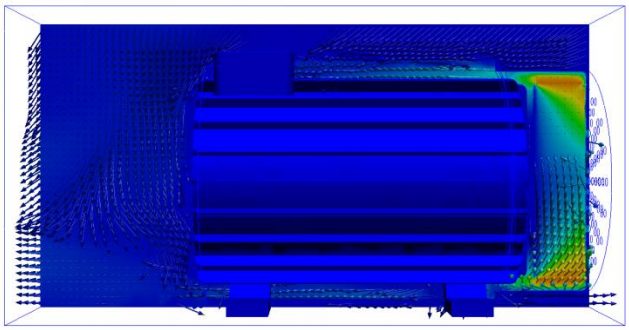

Fig. 12. The airflow with velocity vectors along motor body (vertical cross-section)

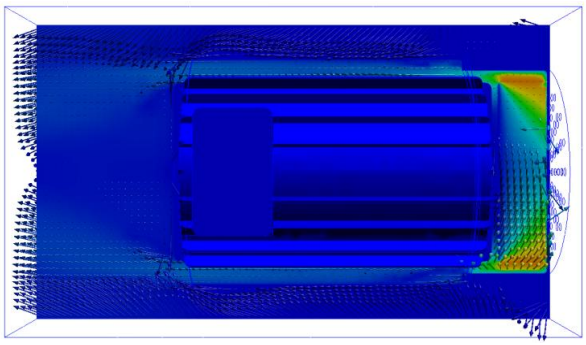

Fig. 13. The airflow with velocity vectors along motor body (horizontal cross-section)

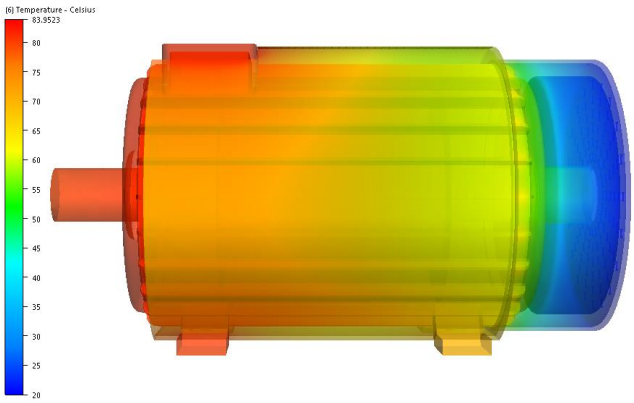

Fig. 14. The temperature profile of motor with additional housing

For solutions with the second type of fan on the side surface of the additional housing the maximum temperature was lower of almost 11°C (57.0°C) and the minimum temperature was the same, and on the top surface the maximum temperature was higher of about 4°C (72.0°C) and the minimum temperature was almost the same (Tab 2).

Tab. 2. Compare temperatures for the two types of housing using fan II

T_{max} [°C] for fan II	Motor with clasical housing	Motor with additional housing
	71.2	76.9
On surface of the lateral housing side		57.0
On surface of the upper housing side		72.0
On radiator of the lateral side	67.9	
On radiator of the upper side	68.2	

It seems likely that better results in terms of cooling can be achieved by modeling the cover in the form of a cone extended towards the front of the motor.

Obtaining a lower temperature on the housing can have a positive impact on the safety of the device usage.

4. SUMMARY

Numerical simulations confirm that the cooling efficiency of the electrical motors depends on the type of the cooling fan used. The first type of fan which is widely used in electric motors is not optimal in cooling system and it is sufficient only for a temporary work with full power or permanent work with a low load. The second type of the fans considered is a more effective solution, as it is much lighter and easier to build. It seems that, regardless of the fan design, to make proper cooling system for permanent work machine, we must use the rotational airflow from rotating fan.

The results of the analysis of the airflow and temperature parameters for the various constructions may be useful for the diagnosis and the design of cooling systems of electrical motors. What is more, thanks to the results of numerical analyzes, the actual state of the machine can be better known. That allows to predict optimal machine's operation in various conditions. The results of numerical analysis will be soon subjected to rigorous experimental verification.

REFERENCES

1. **Będkowski B., Madej J.** (2012), The potential of 3D FEM and CFD methods for cooling systems analysis of electrical machines - the premises, *Zeszyty Problemowe Maszyny Elektryczne*, BOBRME Komel, No. 3, 139-143.
2. **Boglietti A., Cavagnino A., Staton D., Shanel M., Mueller M., Mejuto C.** (2009), Evolution and Modern Approaches for Thermal Analysis of Electrical Machine, *IEEE Trans. Ind. Electron*., Vol. 56, 3, 871-882.
3. **Chang C.C., Kuo Y.F., Wang J.C., Chen S.L.**(2010), Air cooling for a large-scale motor, *Applied Thermal Engineering*, Vol. 30, 11–12, 1360-1368.
4. **Dorrell D. G., Staton D. A., Hahout J., Hawkins D., McGilp M. I.** (2006), *Linked Electromagnetic and Thermal Modelling of a Permanent Magnet Motor*, PEMD Servo Motor Thermal Analysis.
5. **Hongmin Li**. (2009), Flow driven by a stamped metal cooling fan – Numerical model and validation, *Experimental Thermal and Fluid Science*, Vol. 33, 4, 683-694.
6. **Hongmin Li**. (2010), Cooling of a permanent magnet electric motor with a centrifugal impeller, *International Journal of Heat and Mass Transfer*, Vol. 53, 4, 31, 797-810.
7. **Kelly W., Gigas B.** (2003), Using CFD to predict the behavior of power law fluids near axial-flow impellers operating in the transitional flow regime, *Chemical Engineering Science*, Vol. 58, 10, 2141-2152.
8. **Murthy B.N., Deshmukh N.A., Patwardhan A.W., Joshi J.B.** (2007), Hollow self-inducing impellers: Flow visualization and CFD simulation, *Chemical Engineering Science*, Vol. 62, 14, 3839-3848.
9. **Lim C.H., Airoldi G., Bumby J.R., Dominy R.G., Ingram G.I., Mahkamov K., Brown N.L., Mebarki A., Shanel M.** (2010), Experimental and CFD investigation of a lumped parameter thermal model of a single-sided, slotted axial flux generator, *International Journal of Thermal Sciences*, Vol. 49, 9, 1732-1741.
10. **Szczypior J., Jakubowski R.** (2009), Calculation of heat storage in the coreless machine with permanent magnet with direct cooling, *Zeszyty Problemowe Maszyny Elektryczne*, BOBRME Komel, No. 83, 59-66.

INFLUENCE OF TEMPERATURE AND LOADING PROGRAM ON THE FATIGUE LIFE OF STEEL P91

Stanisław MROZIŃSKI*, Michał PIOTROWSKI*

*Faculty of Mechanical Engineering, University of Technology and Life Sciences in Bydgoszcz, Prof. Kaliskiego 7, 85-796 Bydgoszcz, Poland

stanislaw.mrozinski@utp.edu.pl, m.piotrowski@utp.edu.pl

Abstract: In this paper there are shown the results of low-cycle fatigue testing of steel P91 samples. During the testing there was conducted a fixed amplitude loading testing as well as programmed loading with various sequence degrees of the program. The testing was done in two temperatures: T=20°C and T=600ºC. During the testing a cyclic steel weakening was observed without a clear period of stabilization. Greater changes of the cyclic properties were observed in temperature T=600ºC. The influence of temperature on the fatigue life was determined in this paper. This influence is dependent on the degree of strain. It's a minor one in the range of big strain and increases in the process of decreasing the degree of strain. Furthermore, the impact of the loading program type was determined on the test results and fatigue life calculations.

Keywords: Cyclic Properties, Fatigue Life, Programmed Loading, Cyclic Hardening and Weakening

1. INTRODUCTION

Predicting the fatigue life of technical objects during operations in increased temperatures has been a problem of many research institutes. This problem is especially relevant in the electronics industry where there is a need to renovate electric blocks, which in turn results in enormous costs. That is why it is vital to plan them optimally from the engineering stand point. Despite the fact that the process of damaging of technical objects operated in conditions of thermal and mechanical strains has been written about numerous times this issue still remains unresolved (Nagode and Zingsheim, 2004; Byrne et al. 1999; Nagesha et al. 2002).The calculation of fatigue life are related to the question of cumulative fatigue damage and the need to adopt appropriate hypothesis of summation fatigue damage. Description of the hypothesis dealing with summing up fatigue damage and the possibility of their use are discussed in detail in (Manson and Halford, 1986; Fatemi and Yang, 1998; Szala, 1988). Currently, renovations of power units are planned usually on the basis of the results of low cycle fatigue tests, and the results of calculations using the stability of the Palmgren-Miner hypothesis dealing with summing up fatigue damage (Palmgren, 1924; Miner, 1945). This hypothesis doesn't include the loading history (Mroziński, 2011). Aim of this work is the experimental verification of the hypothesis dealing with summing up fatigue damage in the programmed load conditions at elevated temperatures.

2. TESTING DESCRIPTION

Samples for the experiment were made out of steel P91 used in heating plants according to (Palmgren A., 1924). The samples were extracted from a heating pipe like depicted in Fig. 1a and their final dimensions – Fig. 1b.

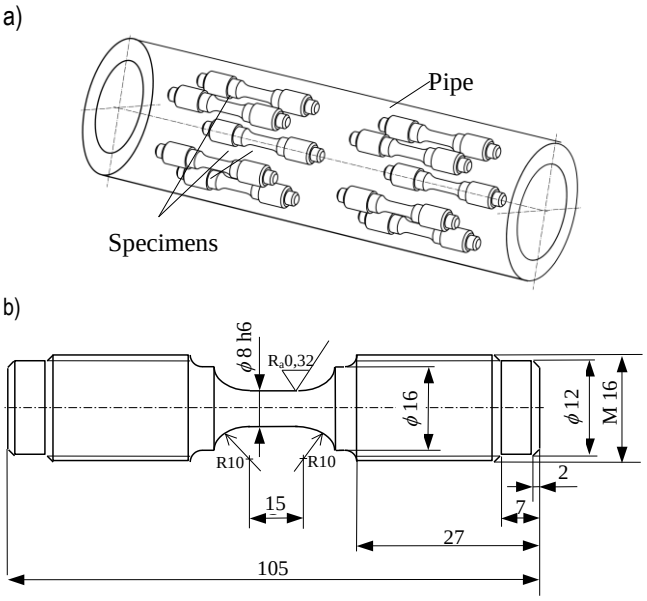

Fig. 1. Sample for testing: a) extraction places, b) sample's dimensions

The fatigue life tests were conducted in the conditions of fixed amplitude and programmed load in the two temperatures (T=20ºC, T=600ºC). Fixed amplitude tests were done on five levels of full strain (Table 1) in the conditions of controlled strain amplitude (ε_{at}=const). There were carried out two types of programmed load: L-H and H-L. The diagrams of the programs are shown in Tab.1.

Tab. 1. Parameters of loading programs

Name	Stress graph	Specifications
Fixed amplitude load	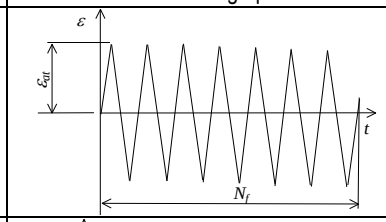	ε_{at} = 0.25%, ε_{at} =0.30%, ε_{at} =0.35%, ε_{at}=0.50%, ε_{at} =0.60%
L-H	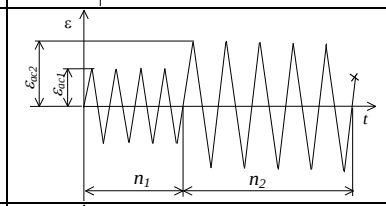	n_1=0.25N_f, n_1=0.5N_f, n_1=0.75N_f $\varepsilon_{at(1)}$=0.30%, $\varepsilon_{at(2)}$ =0.60%
H-L	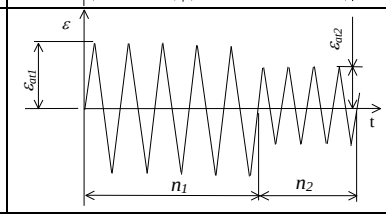	n_1=0.25N_1, n_1=0.5N_f, n_1=0.75N_f $\varepsilon_{at(1)}$=0.60%, $\varepsilon_{at(2)}$ =0.30%

3. TEST RESULTS AND ANALYSIS

3.1. Fixed amplitude fatigue life testing

a)

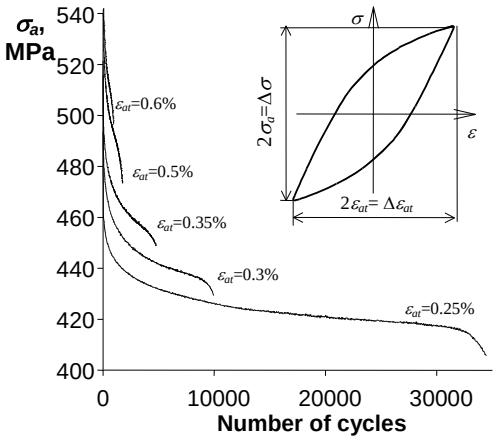

b)

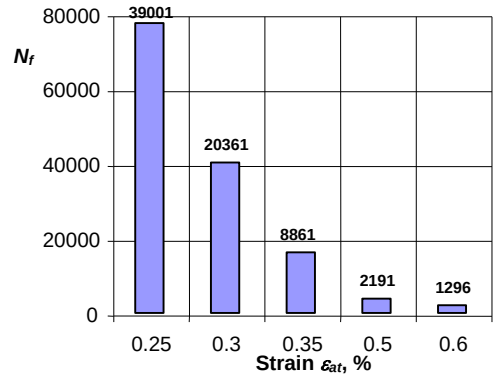

Fig. 2. Results of fatigue tests of steel P91 in temperature T=20ºC:
a) stress σ_a in the function of cycle numbers,
b) fatigue life N_f in relation to ε_{at}

The results of the fatigue life testing in the fixed amplitude conditions were analyzed using two parameters of hysteresis loops used during concluding the results of a low-cycle fatigue testing according to (ASTM E606-92). These parameters include amplitude stress σ_a and the range of plastic strain changes ε_{ap} (Fig. 2a). Considering the final size of this article the results of fixed amplitude fatige life testing in the two temperatures were shown in Fig. 2 and 3 in the form of example graphs of the change of one of the parameters of a hysteresis loop (stress σ_a) in the function of the numbers of loading cycles.

a)

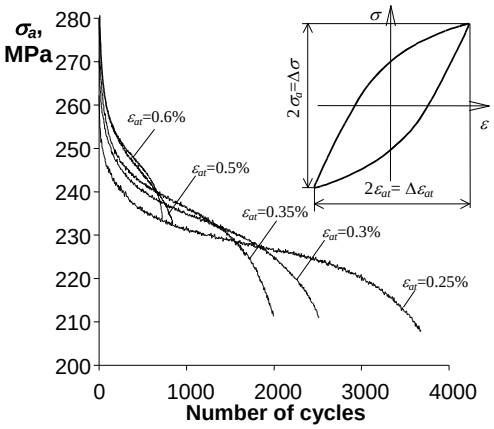

b)

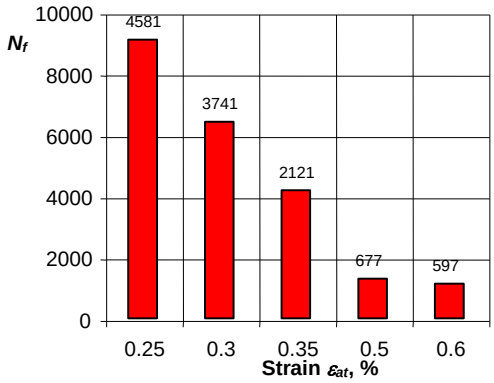

Fig. 3. Results of fatigue tests of steel P91 in temperature T=600ºC:
a) stress σ_a in the function of cycle numbers,
b) fatigue life N_f in relation to ε_{at}

Upon an analysis of the graphs in Fig. 2 and 3 it can be stated that irrespective of the temperature on all of the levels of strain steel P91 undergoes a process of cyclic weakening. A proof of the existence of this process is a constant decrease of stress amplitude σ_a alongside the number of live loading cycles. The cyclic weakening in the ambient and elevated temperatures were also proved by the authors to be present in the tests of cast steel (Mroziński and Skocki, 2012).

In order to illustrate the influence of temperature on the cyclic properties of steel P91, in Fig. 4 there are grouped example function graphs of changes σ_a in the function of cycle numbers on the two levels of total strain ε_{at} (ε_{at}=0.3% and ε_{at}=0.60%). In Fig. 4 there are additionally marked hysteresis loops from three fatigue life periods. These were as follows: loop no. *1* for the first cycle, loop no. *2* from the period corresponding to the halfway point of the fatigue life and loop no. *3* for the last cycle on the given strain level.

Upon an analysis of the graphs (Fig. 4) it can be stated that temporary cyclic properties (parameters of hysteresis loops) depend on the degree of fatigue damage (number of loading cycles) as well as on the temperature. The function graphs of the parameters of hysteresis loops can be divided into three characteristic stages, marked in a diagrammatic form in Fig. 4b as I, II and III.

a)

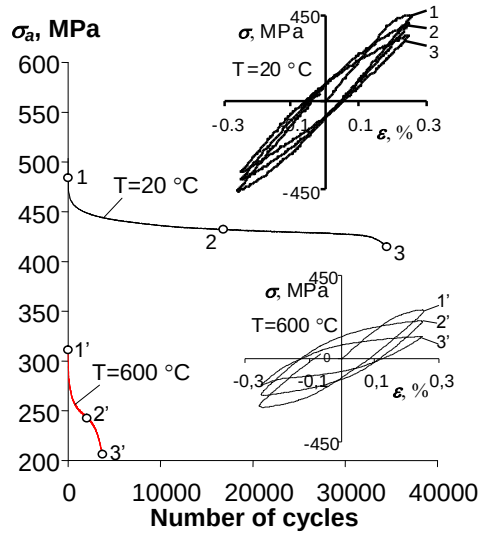

b)

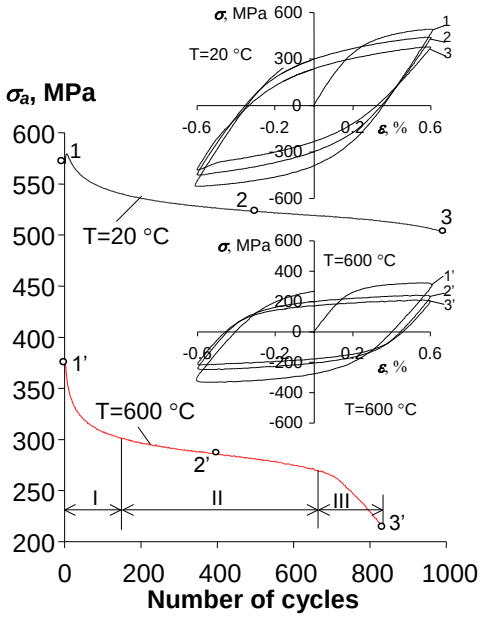

Fig. 4. Changes of σ_a during the fixed amplitude loading of steel P91: a) ε_{at}=0.3%, b) ε_{at}=0.6%

Stage I – steel P91 is weakened greatly. It can be observed during the set level of total strain as a significant reduction of stress σ. The length of this stage depends on the level of strain and the test temperature. Stage II – steel weakens futher. The reduction of stress is much lower than in stage I. Stage III – further siginificant stress reduction. The changes of the properties are caused by microcracks which occur and add up in the material. A crack is initiated which then grows until a fatigue crack occurs.

These significant changes of the cyclic properties of steel P91 in the function of the number of cycles made it difficult to form an analytical description of the material data of the steel in the temperatures of 20 i 600ºC. In order to illustrate this in Fig. 5 there are shown the results of an analytical approximation of the material data of steel P91 in three different fatigue life periods (points 1,2,3 and 1´,2´,3´- Fig. 4). The graph of cyclic strain in the three mentioned cycles was described using the Ramberg-Osgood equation:

$$\varepsilon_a = \frac{\sigma_a}{E} + \left(\frac{\sigma_a}{K'}\right)^{\frac{1}{n'}} \tag{1}$$

a)

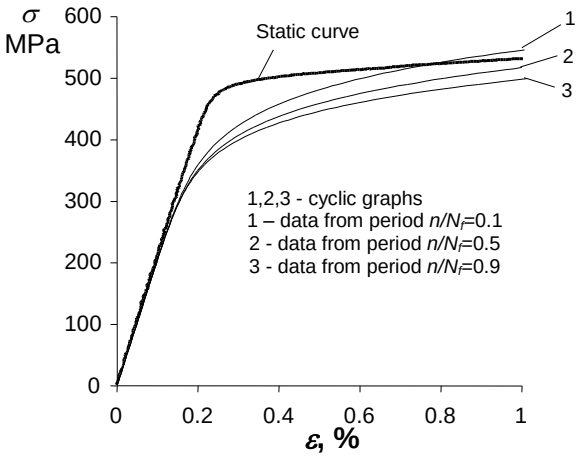

b)

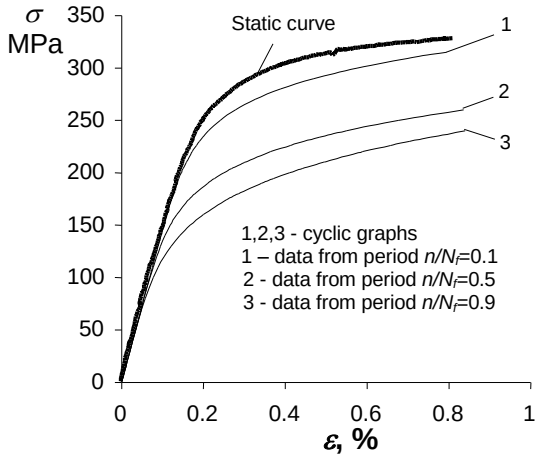

Fig. 5. Grouped graphs of static and cyclic strain: a) T=20°C, b) T=600°C

The graphs of cyclic strain are positioned below the graphs of static strain. The aforementioned fact is a proof of the cyclic weakening of the tested steel. Furthermore, this process is not affected by the test temperature. On the basis of the cyclic strain graphs depicted in Fig. 5 it can be stated that in the case of lack of a stabilization period of the cyclic properties there is used only temporary material data for the fatigue life calculations. The result of such approach can be a significant variance in the fatigue life values obtained from the calculations and from the testing. This fact gets much more important in the case of using this approach to determine the cyclic properties of cast steel in elevated temperatures where the range of changes in the cyclic

properties is larger than in ambient temperatures. The proof of this is a much bigger diversification of the cyclic strain graphs in the temperature 600 ºC (Fig. 5b)

During the testing there was also observed a significant impact of the temperature on the fatigue life. In accordance with (Palmgren, 1924) the fatigue life graphs in the bilogarithmic system were approximated using the equation:

$$\frac{\Delta\varepsilon_{at}}{2}=\frac{\Delta\varepsilon_{ae}}{2}+\frac{\Delta\varepsilon_{ap}}{2}=\frac{\sigma_f'}{E}\left(2N_f\right)^b+\varepsilon_f'\left(2N_f\right)^c \quad (2)$$

where: b - exponent of fatigue life, c - exponent of cyclic strain, σ_f'- coefficient of fatigue life MPa, ε_f' - coefficient of cyclic plastic strain, E- Young's modulus determined from tensile testing MPa.

The exponents and coefficients present in the equation (2) were determined by taking the parameters of the hysteresis loop from the halfway point of the fatigue life (n/N_f=0.5- points 2 i 2' in Fig. 4). The fatigue life graphs obtained from the results of the approximation process of the fatigue life conducted in the two temperatures are shown in Fig. 6.

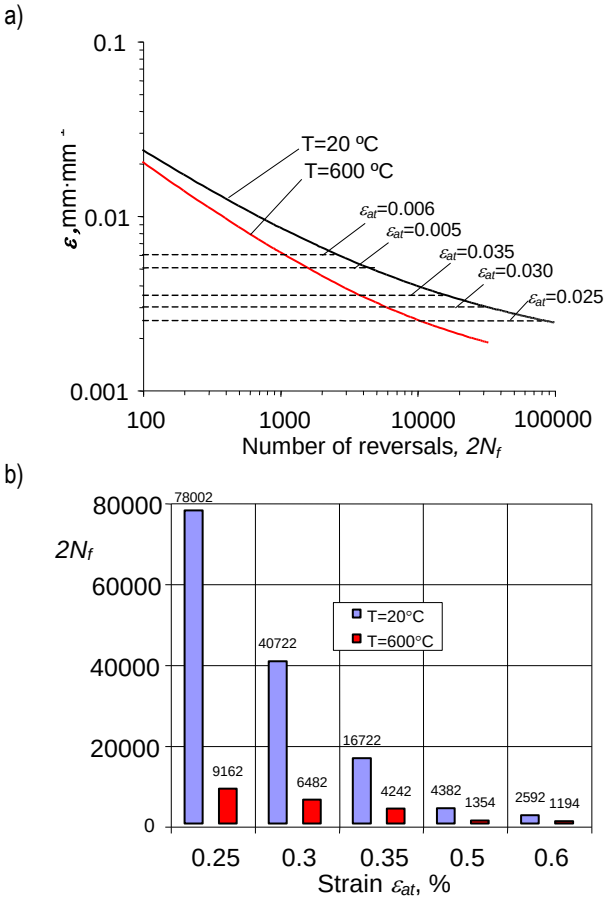

Fig. 6. Influence of temperature and degree of strain on the fatigue life: a) fatigue life graphs, b) quantitative comparison of the fatigue life

On the basis of the above graphs it can be stated that the test temperature has a great influence on the fatigue life. This influence depends on the degree of the full strain amplitude. Also, the temperature's influence is slight in the area of the biggest strain and increases with the decrease of the degree of strain.

3.2. Programmed fatigue life testing

The test results in the conditions of programmed stress were analyzed in the context of the basic changes of the parameters of the hysteresis loop before and after the change of the degree of the program. Similar to the fixed amplitude testing there were observed changes of the basic parameters of the hysteresis loop and a lack of a clear stabilization period. In Fig. 7 and 8 there are shown example function graphs of stress amplitude changes in the function of the number of cycles during the realization of the loading program L-H and H-L in temperatures T=20ºC and 600ºC.

The changes of the cyclic properties of steel P91 after each test can be assessed up to the point of a change of the strain degree and after a change of the deformation. The function of the cyclic properties is the same in the case of the change of the strain degree like in the fixed amplitude loading. Its distinct characteristic is a strong cyclic weakening. A change of the degree of strain took place in the second stage of the changes of the cyclic properties (stage II – see section 3.1).

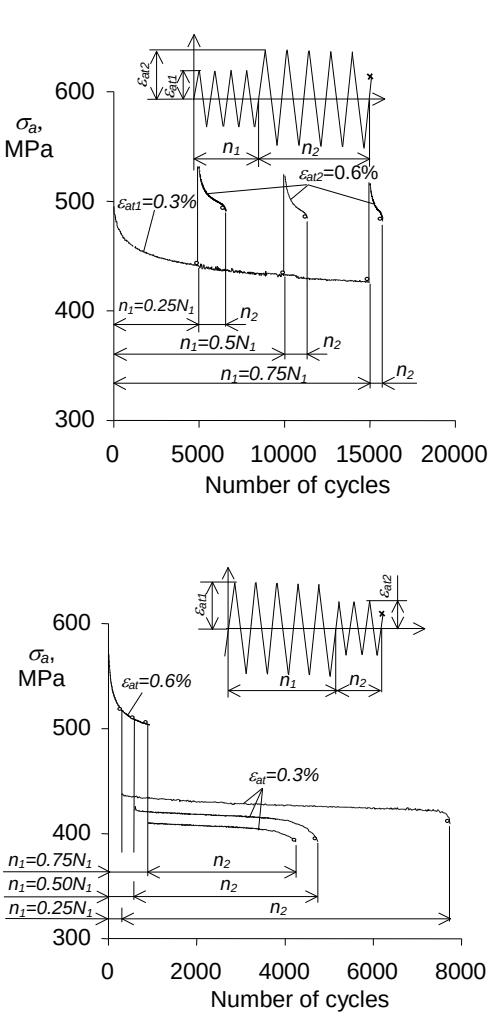

Fig. 7. Changes of σ_a in the programmed loading conditions T=20ºC): a) L-H, b) H-L

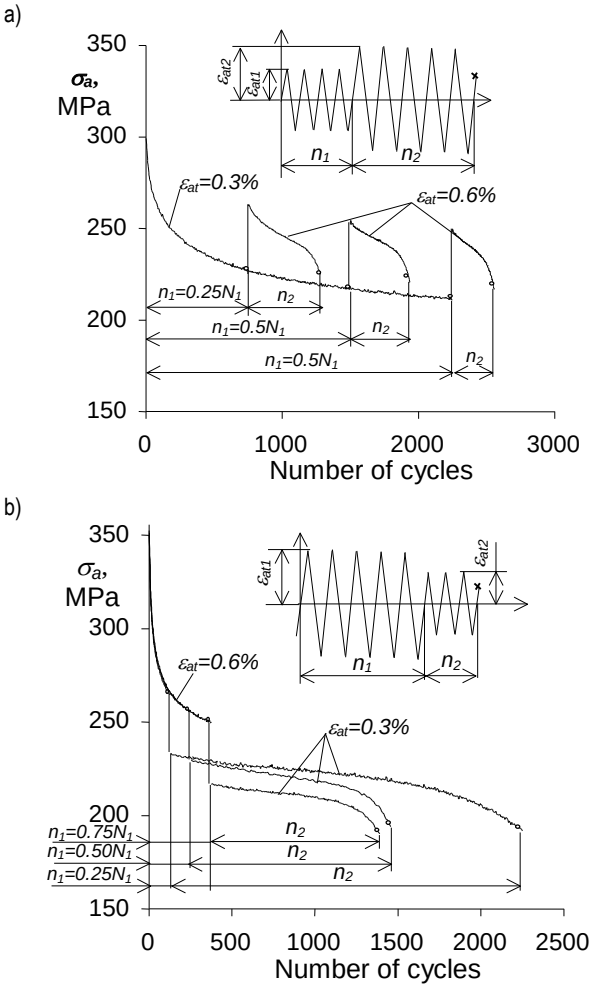

Fig. 8. Changes σ_a in the programmed loading conditions (T=600ºC): a) L-H, b) H-L

On the basis of the depicted graphs it can be stated that the cyclic properties after the change of the degree depend on the number of loading cycles realized on the first level of the program. In the case of the analyzed parameter of the hysteresis loop with the increase of the number of cycles n_1 the stress amplitude σ_a gets smaller on the first degree after the change of the strain level. After this change of the strain level the steel gets more weakened. It applies to temperature T=20°C as well as T=600°C. As expected, alongside the increase of the number of cycles n_1 on the first level, on the second level the number of cycles decreases. Nevertheless, during the testing there could be observed a distinct influence of the sequence of the loading program and temperature on the fatigue life. Higher values were observed for the sequence of program L-H.

In this paper there was conducted an experimental analysis of the Palmger-Miner (PM) hypothesis. According to the PM hypothesis a crack on the sample should occur when:

$$\sum \frac{n_i}{N_i} = \frac{n_1}{N_1} + \frac{n_2}{N_2} = 1 \tag{3}$$

where: N_1–number of cycles till the crack for the fixed amplitude loading on level ε_{at1}, N_2–number of cycles till the crack for the fixed amplitude loading on level ε_{at2}.

The results of the verification are schematically shown in Fig. 9.

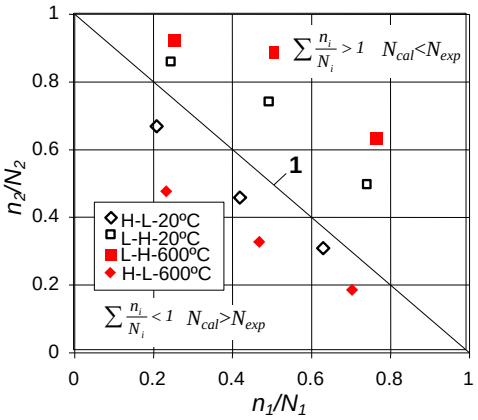

Fig. 9. Results of the verification of the hypothesis of summing up damage PM

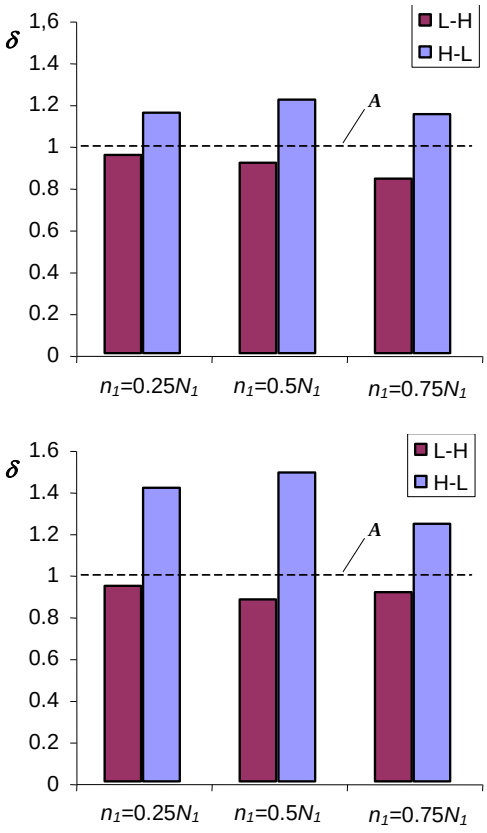

Fig. 10. Values of coeffiecient δ for the different programs: a) T=20 ºC, b) T=600 ºC

The location of the test results on diagonal line 1 of the graph corresponds to the sum of damages $\Sigma n_i/N_i$=1 and indicates that the test results and the results of the calculations are the equal. It also shows lack of any influence of the sequence of the loading program on the fatigue life. The fact that the sum $\Sigma n_i/N_i \neq 1$ was obtained for the two sequences of the programs indicates the influence of the loading history on the results of the fatigue life. Upon the analysis of the obtained fatigue life results (Fig. 9) it has been concluded that for all the sequences L-H the fatigue

life values which were calculated are lower than the values determined from the testing ($N_{cal}<N_{exp}$). On the other hand, the calculated fatigue life values for all the program sequences H-L are higher than the ones obtained from the testing ($N_{cal}>N_{exp}$). In order to arrive at the quantitative assessment of the obtained results of the fatigue life from the calculations (N_{cal}) and from the testing (N_{exp}) a coefficient was introduced:

$$\delta = \frac{N_{cal}}{N_{exp}} \tag{4}$$

The values of coeffiecient δ are shown in the form of graphs in Fig. 10.

The values of coeffiecient δ which equal to unity (line A) simultnaeously mean that the damages sum which was calculated using the equation (3) is also equal to unity and is in accordance to the results obtained from the calculations and the testing. The damages sum $\Sigma n_i/N_i \neq 1$ obtained from the two loading program sequences L-H i H-L lead to an existing influence of the loading history on the fatigue life calculations. On the basis of the conducted testing it has been stated that the influence of the loading history increases in temperature 600ºC.

Results obtained in the operation results are proof steel P91 published inter alia in Junak and Cieśla (2010, 2011).

4. CONCLUSIONS

Upon an analysis of the obtained results the following conclusions can be drawn:

1. Steel P91 during the low-cycle fatigue test in temperatures 20 i 600°C undergoes a cyclic weakening and does not exhibit a clear stabilization period.
2. Level of strain and temperature impact the degree of changes of the cyclic properties. In temperature 600°C the degree of the changes of the cyclic properties is much greater than in temperature 20°C.
3. Level of strain as well as the test temperature influence the steel's fatigue life. The influence of the temperature on the fatigue life depends on the strain level. This influence is slight in the area of very big loads and increases alongside the decrease of the strain level.
4. The occurring changes of the cyclic properties (parameters of the hysteresis loop) and a lack of a clear stabilization period of cast steel in temperatures 20 and 600°C make it difficult to determine the basic material data. The data's values depend on the fatigue life period taken for their calculations. The act of taking them from the halfway point of the fatigue life cause them to be only the temporary cyclic properties of cast steel from this fatigue life period.
5. The loading history has a significant impact on the fatigue life. The experimental verification of the Palmgren-Miner hypothesis indicated that its effectiveness is influenced by the loading history and the test temperature. Alongside an increase in the temperature the linear hypothesis' effectiveness decrease.

REFERENCES

1. **ASTM E606-92**: Standard Practice for Strain -Controlled Fatigue.
2. **Byrne J., Kan N. Y. K.** (1999), Hussey I.W., Harrison G.F.: Influence of sub-surface defects on low-cycle fatigue life in a gas turbine disc alloy at elevated temperature, *International Journal of Fatigue*, 21, 195-206
3. **Fatemi A., Yang L**. (1998), Cumulative Fatigue Damage and Life Prediction Theories: A Survey of the State of the Art for Homogeneous Materials, *International Journal of Fatigue*, 20, 9-34.
4. **Junak G., Cieśla M**. (2010), Low cycle life at graded load for steel in power generators, *Energetyka*, 21, 74-77 (in Polish).
5. **Junak G., Cieśla M**. (2011), Effect of graded loads on low cycle durability of steel P91 i P92 used in power generation, *Inżynieria materiałowa*, 32, 5, 862-867 (in Polish).
6. **Junak G., Cieśla M**. (2011), Low-cycle fatigue of P91 and P92 steels used in the power engineering industry, *Archives of Materials Science and Engineering*, vol. 48 nr 1, 19-24.
7. **Manson S. S., Halford G. R**. (1986), Re-Examination of Cumulative Fatigue Damage Analysis – an Engineering Perspective, *Engineering Fracture Mechanics*, 25(5/6), 539-571.
8. **Miner M. A**. (1945), Cumulative Damage in Fatigue, *Transactions of the American Society of Mechanicals Engineers Journal of Applied Mechanics*, 67, 159-164.
9. **Mroziński S**. (2011), The influence of loading program on the course of fatigue damage cumulation, *Journal of Theoretical and Applied Mechanics*, 49, 1, 83-95.
10. **Mroziński S., Skocki R.** (2012), Influence of temperature on the cyclic properties of martensitic cast steel, *Materials Science Forum*, Vol. 726, 150-155.
11. **Nagesha A., Valsan M., Kannan R., Bhanu Sankara Rao K., Mannan S.L**. (2002), Influence of temperature on the low cycle fatigue behaviour of a modified 9Cr-1 Mo ferritic steel, *International Journal of Fatigue*, 24, 1285-1293.
12. **Nagode M., Zingsheim M**. (2004), An online algorithm for temperature influenced fatigue life estimation: strain-life approach, *International Journal of Fatigue*, 26, 155-161.
13. **Palmgren A**. (1924), *Die Lebensdauer von Kugellagem Verfahrenstechnik*, Berlin, 68, 339-341.
14. **Szala J**., *Fatigue damage summation hypothesis*, University ATR in Bydgoszcz (in Polish).

Acknowledgements: Scientific work funded by the Ministry of Education and Science in the years 2011÷2013 as a research project No 1215/B/T02/2011/40.

DAMAGE MODELING IN GRADED LAYER SYSTEM

Michał PETAŚ*, Krzysztof MRÓZ*, Krzysztof DOLIŃSKI*

*Reliability and Optimization, Department of Computational Science, IPPT PAN, ul. Pawińskego 5B, 02-106 Warszawa, Poland

mpetas@ippt.pan.pl, kmroz@ippt.pan.pl, kdolin@ippt.pan.pl

Abstract: The simplified approach to the modelling of low cycle fatigue (LCF) of functionally graded materials (FGM) based on the continuum mechanics is presented. The fatigue damage model takes into account the mechanical part of the load and a constant service temperature. The concept of FGM as a particle-reinforced metal-matrix composite with gradual change of the reinforcement fraction is used. The FGM is considered as a material consisting of homogeneous layers containing different volume fractions of the reinforcement. The variation of the reinforcement fraction changes the material properties for each layer. The different material properties are obtained according to modified rule of mixture. Since the fatigue damage of metal matrix composites is strongly influenced by the inelastic deformation of the metallic matrix, the constitutive equations of LCF damage model are taken into consideration. The combined isotropic/kinematic hardening model with linear behaviour of isotropic and kinematic parts of hardening is adopted. The damage scalar parameter is associated with the plastic energy dissipation which is used to update the material properties. The fatigue damage model presented in this paper is applied to the fatigue damage analysis of the cooling channel of thruster used in space shuttles and rockets.

Key words: Fatigue Damage, Low Cycle Fatigue, Functionally Graded Materials, Layers

1. INTRODUCTION

The main objective of this work is to present the damage model of the Low Cycle Fatigue (LCF) for a special kind of Particle-Reinforced Metal-Matrix Composites (PR-MMC) with heterogeneous structure. This heterogeneity is assumed to be distributed in one direction within the entire volume of a material. These materials known as Functionally Graded Materials (FGMs) are a new class of the composites that have been developed recently for various engineering applications. The application of this concept to PR-MMC leads to the development of materials/components designed with the purpose of being selectively reinforced only in regions requiring increased strength and/or wear resistance. It extends essentially the industrial applications of the considered materials.

Most of structural elements are subjected to cyclic loading under service conditions. The elaboration of the methods to fatigue life analysis of FGMs is a challenge for modern industry, because the problem of the cumulative fatigue damage has not been resolved yet despite the fact that the history of fatigue damage modeling is dated back to 1920s and 1930s. Therefore, the attention in this paper is devoted to the numerical modeling of low cycle fatigue induced by mechanical loading. The damage model of LCF is based on the accumulated plastic strain energy dissipation. On the assumption that the stresses in LCF are close or above the yield limit and global plasticity will be dominating cause of fatigue damage in FGMs, the linear isotropic/kinematic hardening model in combination with the Huber-von Misses yield surface is used to calculate plastic energy dissipation for each loading cycle. On the basis of the energy approach, the damage parameter D is calculated. Use of the damage parameter is aimed at updating the material properties to simulate cyclic behaviour of FGM composite. The micro-structural parameters, such as the volume fractions are taken into account to calculate material properties of FGM composite. The FGM is considered as a material consisting of homogeneous layers containing different volume fractions of the reinforcement. The fatigue damage model presented in this paper is applied to fatigue damage analysis of cooling channel of thruster used in space shuttles and rockets with the assumption that delamination of layers is not possible.

2. APPROACHES TO FATIGUE DAMAGE

Palmgren (1924) was the first who introduced the concept of linear summation of fatigue damage. This concept known as Linear Damage Rule (LDR) was represented first time in mathematical form by Miner (1945). In the LDR the measure of damage is simply the cycle ratio with a basic assumption of the constant work absorption per cycle and characteristic amount of work absorbed at failure. The energy accumulation, therefore, leads to a linear summation of cycle ratio or damage. The main deficiencies with LDR are its load-level independence, load-sequence independence and lack of load-interaction accountability. Machlin (1949) proposed a metallurgically based cumulative theory which is basically another form of LDR. In 1950s, Coffin and co-workers (Coffin, 1956; Baldwin et al., 1957) expressed the LDR in terms of plastic strain range which is related to fatigue life though the Coffin-Manson relation. However, due to the inherent deficiencies of the LDR, no matter which version is used, life prediction based on this rule is often unsatisfactory. To remedy the deficiencies associated with LDR Richart and Newmark (1948) introduced the concept of damage curve and speculated that such curve of damage parameter and cycle ratio ought to be different at different stress-levels. Upon this concept and the results of load sequence experiments, Marco and Starkey (1954) proposed in 1954 the first nonlinear load-dependent damage theory represented by a power relationship.

Next concept of fatigue damage is theory based on endurance limit reduction. French (1933) was the first who reported the significant investigation of the overstress effect on endurance limit. In 1938 Kommers (1945) and Bennet (1946) suggested the change of the endurance limit as a damage measure but they did not correlate this measure to the life fraction. This kind of correlation was for the first time deduced by Henry (1955) and later by Gatts (1961, 1962) and Bluhm (1962). All of these damage models based on endurance limit reduction are nonlinear and able to account for the load sequence effect. None of these models take into account load interaction effects. Early theories accounting for load interaction effects are based on Corten-Dolon model (Corten and Dolon, 1956) and Freudenthal-Heller (Freudenthal, 1956; Freudenthal and Heller, 1956) approach. Both theories are based on the modification of the stress-cycles diagram, which is simply a clockwise rotation of the original stress-cycles line. Langer (1937) was the first who proposed to separate the fatigue damage process into two stages, namely: the crack initiation and crack propagation. The linear rule was proposed for each stage. Following Langer's concept Grover (1960) considered cycle ratios for two separate stages in the fatigue damage process under constant stress amplitude. Manson (1966) reverted to Grover's work and proposed the Double Linear Damage Rule called DLDR.

Another approach in cumulative fatigue damage analysis is the crack growth concept. On the basis of the mechanism of progressive unbounding of atoms as a result of reversed slip induced by stress cycling Shanley (1952) introduced a damage theory by defining crack length as measure. It was suggested that the crack growth rate varies with the applied stress level in either a linear or an exponential manner. Valluri (1961a, b) presented a crack growth damage model in a differential form. The quantitative develoment of the theory is based on concepts derived from dislocation theory and a synthesis of the macroscopic elasto-plastic fracture theory. On the basis of the DLDR and crack growth approaches Manson and Halford (1981) presented damage curve approach (DCA) to refine the original DLDR through a reliable physical basis. They empirically formulated the 'effective crack growth' model based on phenomenological recognition that the major manifestation of damage is crack growth which involves many complicated processes such as dislocation agglomeration, subcell formation, multiple micro-crack formation and the independent growth of these cracks until they link and form a dominant crack. Manson and Halford and co-workers (Bizon et al., 1985; Halford and Manson, 1985; Manson and Halford, 1981, 1983) developed DCA approach by adding a linear term to the DCA equation with some mathematical manipulation and called it Double-Damage curve model (DDCA). The models developed by Manson and Halford are all load-level dependent, but do not account for the load interaction effect and small-amplitude cycle damage. In 1971 Bui-Quoc and colleagues presented their work dealing with cumulative fatigue damage under stress-controlled (Bui-Quoc, 1981) and strain-controlled (Bui-Quoc et al., 1971) conditions. Both theories were combined into 'unified theory' (Dubuc et al., 1971). The theory for stress-controlled fatigue was first developed from the hybridization of four prior damage models by Henry (1955), Gatts (1961), Shanley (1952) and Valluri (1961). Bui-Quoc and coworkers (Bernard-Connolly, 1983; Biron and Bui-Quoc, 1981; Bui-Quoc, 1981, 1982 a,b) modified their damage models to account for the load interaction effect under cyclic loading involving several stress levels. After the early 1970s, new fatigue damage theories have been developed based on the microcrack grow concept. Most of these newer models better explain the physics of the damage than those developed before 1970s. A popular macro fatigue crack growth retardation model (Wheeler, 1972) is formulated by Wheeler. This model assumes the crack growth rate to be related to the interaction of crack-tip plastic zones under residual compressive stresses created by overloads. A similar model based on crack tip plasticity is Willenborg model (Willenborg et al., 1971). This model uses an effective stress intensity factor at the crack tip to reduce the applied crack tip stress intensity factor due to the increased crack tip residual compressive stress induced by the overloads.

Next fatigue damage concept is energy based approach. Since Inglis presented the report (Inglis, 1927) of connection between hysteresis energy and fatigue behaviour many studies on energy methods have been carried out. Several failure criteria based on strain energy were established by Morrow (1965), Halfrod (1966), Glinka et al. (1995), Lagoda (2001), Seweryn et al. (2008), Zuchowsky (1989) and Leis (1997). Some energy-based damage parameters have been proposed. It has been realized that an energy-based damage parameter can unify the damage caused by different types of loading such as thermal cycling, creep, and fatigue. Energy-based damage models can also include mean stress and multiaxial loads since multiaxial fatigue parameters based on strain energy have been developed. Kujawsky and Ellyin [38] developed a damage model by using plastic strain energy density as a parameter. It was later found that some inefficiency were associated with plastic strain energy approach. For example, the effect of mean stress cannot be directly incorporated in the determination of the hysteresis energy. Also, for the low strain high-cycle fatigue, the plastic strain energy density is very small. In some cases the macroscopic (bulk) response of the material is elastic or quasi-elastic, microscopic (local) plastic deformation may still exist in the material due to the nonuniformity of local strain distribution and/or due to the strain concentration by high prestraining. Golos and Ellyin (1987, 1988, 1989) modified the plastic strain energy-based model using total strain energy density. The total strain energy density combines both plastic and elastic portions. The elastic portion is thought to be associated with the tensile mode and can facilitate crack growth. A power function analogous to stress-cycles relation is employed to describe the energy-life relation, which is a straight line in a log frame. Leis (1988) proposed an energy-based nonlinear history-dependent damage model which links the damage parameter to fatigue life. He speculated that the instantaneous strain-hardening exponent can be characterized as a function of accumulation of plastic strain. The model created by Leis is therefore an analytical formulation in terms of the deformation history. Clearly, properly defining the function of strain-hardening exponent is crucial in the application of this damage model. Niu (1987) and Niu et al. (1987) found the cyclic strain hardening coefficient to change during the cyclic process while the cyclic strain hardening exponent had a negligible change. In this model, the energy accumulation is defined by introducing a parameter called fraction of plastic strain energy. The model represented by Niu et al. is a nonlinear, load-dependent damage accumulation model. It accounts for the load interaction effect and the change in strain hardening through the stress response. This model is especially suitable for materials which exhibit cyclic hardening. Radhakrishnan [60,61] postulated that the crack growth rate is proportional to the plastic strain energy density which is linearly accumulated to failure. His formulation of damage equation implies that failure occurs when the accumulated plastic energy reaches the value of total plastic energy in the last loading stage

under constant amplitude cycling. This implication excludes the influence of load interaction effect on total plastic energy.

Another approach of fatigue damage is based on Continuum Damage Mechanics (CDM). CDM deals with the mechanical behavior of a deteriorating medium at the continuum scale. This approach is developed based on the original concepts of Kachanov (1969) and Rabotnov (1969) in treating creep damage problems. The success of CDM application in modelling the creep damage process has encouraged many researches to extend this approach to ductile plastic damage, creep-fatigue interaction, brittle fracture and fatigue damage. In addition to metallic materials CDM can also be applied to composites and concrete materials. Chaboche (1974) postulated that fatigue damage evolution per cycle for one-dimensional case can be generalized by a function of the load condition and damage state. Tests conducted under completely reversed strain-controlled conditions provided supportive information. By measuring the changes in tensile load-carrying capacity and using the effective stress concept he formulated a nonlinear damage evolution law (Chaboche, 1974, 1982). This damage model is highly nonlinear in damage evolution and is able to account for the mean stress effect. It is, therefore, called a Nonlinear-Continuous-Damage (NLCD) model (Chaboche and Lesne, 1988). This model has three main advantages. First, it allows for the growth of damage below the initial fatigue limit, when the material is subjected to prior cycling above the fatigue limit (Chaboche and Lesne, 1988). Second, the model is able to take into account the influence of initial hardening effect by introducing a new internal variable which keeps memory of the largest plastic strain range in the prior loading history (Chaboche and Kaczmarek, 1981; Chaboche and Lesne, 1988). Third, mean stress effect is directly incorporated in the model. Based on the CDM concept, many other forms of fatigue damage equations have been developed after Chaboche's work (Chaboche, 1974). Such models include those proposed by Lemaitre and Chaboche (1978, 1990), Lemaire and Plumtree (1979) and Li et al. (1989). Basically, all these CDM-based approaches are very similar to Chaboche NLCD model in both form and nature. The main differences lie in the number and the characteristics of the parameters used in the model, in the requirements for additional experiments, and in their applicability. Socie and co-workers (Socie, 1983; Weinacht and Socie, 1987) applied the Lemaitre-Plumtree model to the fatigue damage analysis of cast iron to account for the influence of defects on fatigue life. They reported improved life predictions as compared to the Miner rule (Socie et al., 1983). Plumtree and O'Connor (1989) attempted to analyze damage accumulation and fatigue crack propagation in aluminum alloy using a modified Lemaitre-Plumtree model. Hua and Socie (1984) also evaluated the Chaboche and Lemaitre-Plumtree models in their investigations of biaxial fatigue. They found the Chaboche model to be better than Lemaitre-Plumtree model for fatigue damage assessment.

Though many damage models have been developed, unfortunately, none of them enjoys universal acceptance. Each damage model can only account for one or several phenomenological factors, such as load dependence, multiple damage stages, nonlinear damage evolution, load sequence and interaction effects, overload effects, small amplitude cycles below fatigue limit and mean stress. Due to the complexity of the problem none of the existing predictive models can encompass all of these factors. Therefore, more efforts in the study of cumulative fatigue damage are needed in order to provide design engineers with a general and reliable fatigue damage analysis and life prediction model.

3. MODEL DESCRIPTION

3.1. Flow Hardening and Damage Rules

The fatigue damage concept presented in this paper is developed by using micromechanical and continuum mechanics approaches in combination with Finite Element Method. Implementation of the damage model is made in Abaqus UMAT subroutine. The gradual change in composite is modelled by assuming that the FGM material consists of layers of the various volume fraction of the uniformly distributed reinforcement. The same sizes of reinforcement particles within each layer are assumed.

Low cycle fatigue damage of metal matrix composites is strongly influenced by the inelastic deformation in metallic matrix (LLorca, 2002). Therefore, the constitutive equations of LCF damage model take into account the most important effects of inelastic deformation, such as the increase of yield stress with rising deformation, rate- and time-dependency, yield stress reduction after a change of the straining direction known as Bausinger-effect and the hysteresis loops resulting from cyclic loadings conditions. The model consists of elastic and plastic constitutive laws in the context of infinite deformation theory. Elasticity is considered isotropic and linear. Simulation of plasticity effects is possible by using the combined isotropic/kinematic hardening model with linear behaviour of isotropic and kinematic parts of hardening. This feature is particularly appropriate for applications to cyclic plasticity within an individual cycle where kinematic hardening is the dominant hardening process reflected in the Bauschinger effect, but over quite large numbers of cycles the material also hardens isotropically leading to the eventual saturation of the inelastic energy (Dunne and Petrinic, 2005). The hardening model is used in combination with the Huber-von Misses Yield criterion which is applicable for analysis of plastic deformation for ductile materials such as metals. It can be also adapted to metal-matrix composites. On the basis of Huber-von Misses criterion the effective stress is determined to identify the yield condition for multiaxial load. If this stress is equal or greater than yield stress then the material yields. Otherwise, the material behaviour is elastic. The effective stress is obtained from the following equation:

$$\sigma_{\mathrm{e}} = \sqrt{\frac{3}{2}(\mathrm{S_{ij}} - \alpha_{\mathrm{ij}}) : (\mathrm{S_{ij}} - \alpha_{\mathrm{ij}})}, \tag{1}$$

where: σ_e – is the equivalent stress, S_{ij} – denotes the stress deviator tensor, α_{ij} – is the shift tensor (backstress tensor).

The Huber-von Misses yield criterion for combined hardening model is defined by:

$$f = \sigma_e - r - \sigma_y = 0, \tag{2}$$

where: f – yield function, r – isotropic hardening function, σ_y – initial yield stress of a composite material obtained from static tensile characteristics. After substituting eq. (1) to eq. (2) the yield function becomes:

$$f = \sqrt{\frac{3}{2}(\mathrm{S_{ij}} - \alpha_{\mathrm{ij}}) : (\mathrm{S_{ij}} - \alpha_{\mathrm{ij}})} - r - \sigma_y = 0. \tag{3}$$

When the plastic deformation occurs ($f = 0$) and loading continues the associated plastic flow law determines the direction of increment of the plastic strain tensor. This direction is normal to the yield surface at the load point. The equation of the associ-

ated plastic flow law is written as follows:

$$\dot{\varepsilon}^p = \dot{\lambda}\frac{\partial f}{\partial \sigma} = \dot{\lambda}\cdot \nabla f\ ,\ d\varepsilon^p = d\lambda\frac{\partial f}{\partial \sigma} = d\lambda\cdot \nabla f, \tag{4}$$

where: $\dot{\varepsilon}^p$ – plastic strain rate, $\dot{\lambda}$ – plastic multiplier (strain rates), $d\varepsilon^p$ – plastic strain increment, $d\lambda$ – plastic multiplier (strain increments), ∇f – direction of the plastic strain increment. The equation of plastic flow can be written in terms of the deviatoric stress, equivalent stress and equivalent plastic strain:

$$\dot{\varepsilon}^p = \frac{3}{2}\dot{\varepsilon}^{eq}\frac{\boldsymbol{S}}{\sigma_e}\ ,\ \ d\varepsilon^p = \frac{3}{2}d\varepsilon^{eq}\frac{\boldsymbol{S}}{\sigma_e}, \tag{5}$$

where: $\dot{\varepsilon}^{eq}$ – equivalent plastic strain rate, $d\varepsilon^{eq}$ – equivalent plastic strain increment, $\boldsymbol{S}$ – deviator of a stress tensor. The equations of equivalent plastic strain rate and equivalent plastic increment are given in following forms:

$$\dot{\varepsilon}^{eq} = \sqrt{\frac{2}{3}\dot{\varepsilon}^p : \dot{\varepsilon}^p}\ ,\ \ d\varepsilon^{eq} = \sqrt{\frac{2}{3}d\varepsilon^p : d\varepsilon^p}, \tag{6}$$

where: $\dot{\varepsilon}^p$ – plastic strain rate tensor, $d\varepsilon^p$ – plastic strain increment tensor.

During LCF loading, energy is absorbed mainly because of plastic deformation. The majority of this mechanical energy is converted into heat while the remaining part of the energy causes damage in the material. The magnitude of damage experienced by the material during fatigue cycles is strongly dependent on the loading inputs and fatigue resistance of the material and is directly related to the material capacity for absorption of the energy input (Sutton, 2009). Determination of the plastic cyclic strain energy for described model is based on the tensile characteristics and calculated equivalent data. On the basis of the plastic energy dissipation the fatigue damage parameter is determined to describe the cyclic behaviour of composite.

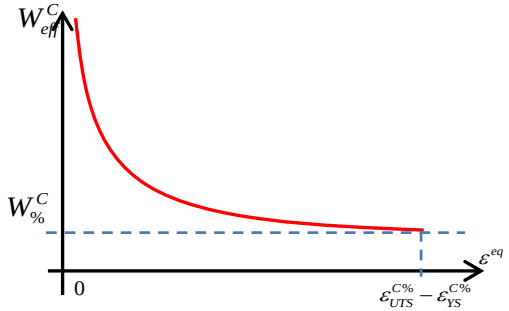

Fig. 1. The critical dissipation energy values function.

Calculation of the increment of damage parameter (D) is based on the following equations:

$$dD = \frac{1}{W^C_{eff}}dW = \frac{1}{f(\varepsilon^{eq})W^C_{\%}}dW = \frac{1}{\left(1+ln\frac{\varepsilon^{C\%}_{UTS}-\varepsilon^{C\%}_{YS}}{\varepsilon^{eq}}\right)W^C_{\%}}dW, \tag{7}$$

where dW is the increment of the plastic strain energy density and can be written as:

$$dW = \sigma_e d\varepsilon^{eq}, \tag{8}$$

W^C_{eff} is the disspation energy value function (Fig. 1), $W^C_{\%}$ – is the critical value of the dissipation energy calculated on the basis of the monotonic tensile stress-strain curve and $\varepsilon^{C\%}_{UTS}, \varepsilon^{C\%}_{YS}$ are the monotonic composite strain values (Fig. 4). When monotonic tensile loading is applied $f(\varepsilon^{eq}) = 1$ and $W^C_{eff} = W^C_{\%}$.

The simulation of cyclic behaviour is possible by updating data of static tensile characteristics (Fig. 2) for a point of the material in which damage occurs. The updating operation is performed at the beginning of every loading cycle. All peak stress values (yield stress, ultimate tensile stress) are updated as follows:

$$\sigma_i = \sigma_{i-1}(1 - D_i), \tag{9}$$

where: σ_i– updated peak stress value, σ_{i-1} – previous peak stress value while the tangent modulus is kept constant. The drop in peak values follows accumulated damage which is calculated from the following equation:

$$D_i = D_{i-1} + \Delta D_{i-1}, \tag{10}$$

where: D_i– accumulated damage in current cycle, D_{i-1} – accumulated damage from previous cycle, ΔD_{i-1} – damage increment from previous cycle (associated with energy dissipation in each cycle). If the parameter D reaches the unit value then failure occurs in the material element.

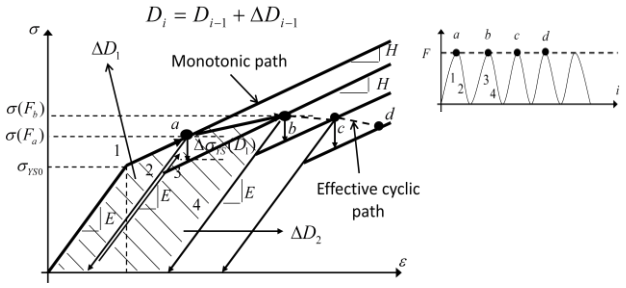

Fig. 2. The cyclic curve with damage approximation

3.2. Effective Stiffness and Hardening Moduli

Stress-strain curve and properties of a composite material are obtained on the basis of modified rule of mixture, named TTO (Tamura-Tomota-Ozawa) (Tamura et al., 1973), related to the spatial distribution of its components and adapted to FGMs by Williamson et al. (1993).

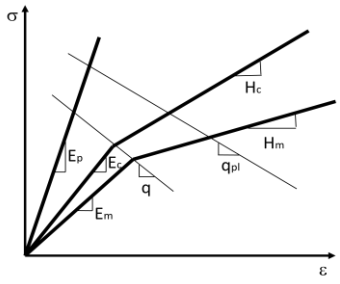

Fig. 3. Stress-strain curves for FGM system using mixture theory

The TTO model relates the uniaxial stress and strain of a two-phase composite, (Fig. 3), to the corresponding average uniaxial stresses and strains of the two constituent materials by:

$$\sigma = V_p\sigma_p + V_m\sigma_m,\ \varepsilon = V_p\varepsilon_p + V_m\varepsilon_m,\ V_p + V_m = 1, \tag{11}$$

where: σ_i and ε_i $(i = p, m)$ – are the average stresses and strains of constituent phases, respectively, V_i $(i = p, m)$ – the

volume fractions of constituent phases. In the TTO model an additional parameter q is introduced which represents the ratio of stress to strain transfer:

$$q = \frac{\sigma_p - \sigma_m}{|\varepsilon_p - \varepsilon_m|}, \tag{12}$$

where: q – ratio of stress to strain transfer.

The value of the q parameter depends on the constituent material properties and the microstructural interaction in the composite. For example, $q \to \infty$ if the constituent elements deform identically in the loading direction, while $q = 0$ if the constituent elements experience the same stress level. In general, the constituent elements in a composite undergo neither equal strain nor equal stress due to the complicated microstructure (variations in particle shape, orientation, volume fraction and so on). A nonzero finite value of q approximately reflects those effects. Note that:

$$\sigma_i = E_i \varepsilon_i, \tag{13}$$

where: $E_i \ (i = p, m)$ – Young's moduli of the constituent phases. Then:

$$\frac{\varepsilon_p}{\varepsilon_m} = \frac{q - E_m}{q - E_p}, \tag{14}$$

or

$$\frac{\sigma_p}{\sigma_m} = \frac{E_p E_m - q E_p}{E_p E_m - q E_m}. \tag{15}$$

The Young's modulus of the composite may be obtained as follows:

$$E^{C\%} = \frac{\sigma}{\varepsilon} = \frac{V_p E_p \frac{q - E_m}{q - E_p} + V_m E_m}{V_p \frac{q - E_m}{q - E_p} + V_m}, \tag{16}$$

where: $E^{C\%}$ – Young's modulus of the composite. The Poisson ratio of the composite ν just follows a rule of mixtures in the TTO model:

$$\nu = \nu_p V_p + \nu_m V_m, \tag{17}$$

where: $\nu_i \ (i = p, m)$ – Poisson's ratio of the constituent phases. For applications involving plastic deformation of ceramic/metal (brittle/ductile) composites the TTO model assumes that the composite yields once the metal constituent yields. The yield stress of the composite, $\sigma_{YS}^{C\%}$, is thus determined as follows:

$$\sigma_{YS}^{C\%} = V_p \sigma_p + V_m \sigma_{YS}^m = \sigma_{YS}^m \left[V_m + \frac{E_m - q}{E_p - q} \frac{E_p}{E_m} (1 - V_m) \right], \tag{18}$$

$$\varepsilon_{el}^{C\%} = \sigma_{YS}^{C\%} / E^{C\%}, \tag{19}$$

where: σ_{YS}^m – yield stress of the metal matrix. The above equation indicates that the yield stress of the composite depends on the yield stress of the metal matrix, the volume fraction of the metal, the Young's moduli of the constituent phases, and the parameter q. Carpenter et al. (1993) chose arbitrarily a q value equal to 4.5 GPa for Ti/TiB FGM system. This value has been previously used for dual phase steels and Al_2O_3-Ni (Williamson et al., 1993). Ideally this parameter should be determined experimentally from the uniaxial stress-strain curve for composite.

Since the ratio of stress to strain transfer for plastic behaviour of matrix is changing, it is postulated to use the second stress to strain transfer parameter as q_{pl}. Then the tangent modulus of composite follows a bilinear response as:

$$H^{C\%} = \frac{V_p E_p \frac{q_{pl} - H_m}{q_{pl} - E_p} + V_m H_m}{V_p \frac{q_{pl} - H_m}{q_{pl} - E_p} + V_m}. \tag{20}$$

If the value of tangent modulus H^{Cx} (Fig. 4), for one composite (two material with different relation) is known it is possible to calculate q_{pl} parameter and to obtain H^{Cy} for different combination of consistent materials. Consequently, the ultimate tensile stress, $\sigma_{UTS}^{C\%}$ can be approximated by:

$$\sigma_{UTS}^{C\%} = V_p \sigma_{UTS}^p + V_m \sigma_{UTS}^m \tag{21}$$

and

$$\varepsilon_{UTS}^{C\%} = \frac{\varepsilon_{el}^{C\%} H^{C\%} + \sigma_{UTS}^{C\%} - \sigma_{YS}^{C\%}}{H^{C\%}}. \tag{22}$$

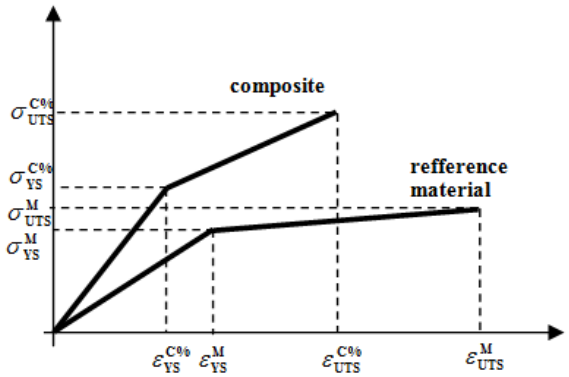

Fig. 4. Stress-strain curves for different combination of consistent materials

4. MODEL APPLICATION

In the aerospace thruster application the currently used material is CuAg3Zr0.5 alloy (no gradient). Fine channels are milled in the thruster basic structure for transporting the fuel (liquid oxygen and hydrogen) as cooling agents (Fig. 5). Unfortunately, in the structures the thinning of the cooling passage wall, bulging of the wall toward the thrust chamber centerline and, finally, failure by a crack ('dog-house' failure mode) is observed under the cyclic plastic deformation at elevated temperature, (Fig. 6). Consequently, the analysis of the single loading is not sufficient for the prediction of the life time of thrusters and the fatigue analysis is needed. In the UE MATRANS project it was proposed to use FGM materials (Al_2O_3-Cu) with gradually changing volume fraction of alumina within Cu matrix as depicted in Fig. 5. The advantage of FGM solution is that by the gradual alumina contents the thermal stresses in the thruster inner wall can be reduced due to different thermal expansion while improving a number of key properties.

In the Tab. 1 the effective experimental and predicted material parameters are presented for the room temperature (RT) and 700K based on the mixture theory.

In order to illustrate the evolution of the fatigue damage process under mechanical cyclic loading in the constant high temperature (700K) a comparison between the references material CuAg3Zr0.5 and graded material Al_2O_3-Cu was made by using the fatigue damage model described in the chapter 3 and the mechanical loading based on Andrews and Armstrong (1974) data (Fig. 8). In Fig. 7 an examined part of the structure is shown. The maximum of the loading conditions (temperature and pressure) for time 2.25s was assumed as a critical one.

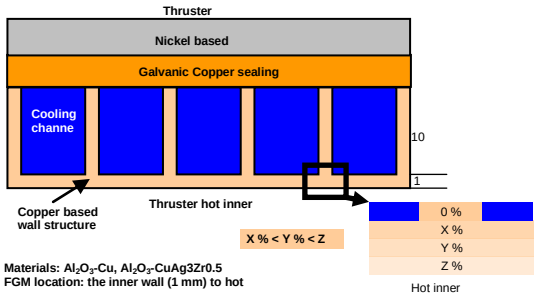

Fig. 5. Basic principle of thruster structure and the proposed FGM solution

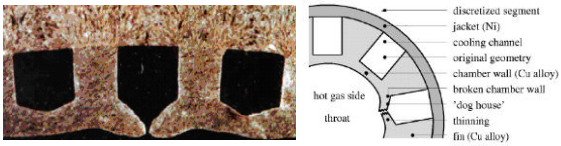

Fig. 6. 'Dog-house' failure mode

Tab. 1. The effective experimental (underlined) and predicted material parameters for the room temperature (RT) and 700K based on mixture theory

	• for RT					• for 700 K (427°C)				
$Cu+\%Al_2O_3$	ν	E	σ_{YS}	σ_{UTS}	ε_{UTS}	ν	E	σ_{YS}	σ_{UTS}	ε_{UTS}
[%]	-	[GPa]	[MPa]	[MPa]	[%]	-	[GPa]	[MPa]	[MPa]	[%]
0	0.33	118	100	230	45	0.34	50	50	75	50
1	0.329	129	113	239	25	0.339	55	55	80	44
2	0.328	139	126	248	17	0.338	60	60	85	39
3.5	0.326	145	145	261	11	0.336	66	67.5	92.5	33.5
5	0.325	166	165	275	8	0.334	73	75	100	29
10	0.32	200	230	320	3.5	0.33	95	100	125	20
CuAg3Zr0.5	ν	E	σ_{YS}	σ_{UTS}	ε_{UTS}	ν	E	σ_{YS}	σ_{UTS}	ε_{UTS}
Ref.	-	[GPa]	[MPa]	[MPa]	[%]	-	[GPa]	[MPa]	[MPa]	[%]
Mat.	0.34	320	140	260	30	0.345	290	110	150	40

* The underlined results were obtained by EADS Innovation Works within the EU FP7 Project 'MATRANS'.

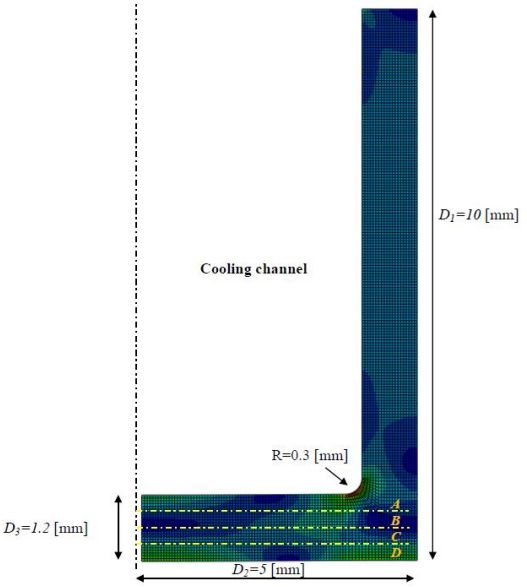

Fig. 7. The considered part of the thruster

The considered part of the thruster consists of 4 parts of materials. The part *A* is made of the base matrix material (OFHC Copper), the layers *B, C* and *D* contain 2%, 3% and 5% of the ceramic particles (Al_2O_3), respectively. The calculations show that the number of cycles to first failure of any single element (N_{in}) in the graded structure is equal to 39,7 % of that number for the references material, i.e.

$$q = \frac{N_{in}}{N_{in\,Ref}}100\%=39{,}7\%, \tag{23}$$

where: N_{in} – number of cycles to first failure of an element in the graded structure, N_{inRef} – number of cycles to first failure of an element in the references material (CuAg3Zr0.5 alloy).

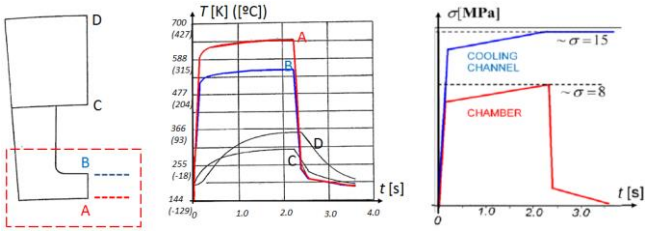

Fig. 8. The thermal-mechanical loading cycle, based on Andrew and Armstrong (1974)

In Fig. 9 the damage comparsion between the references material and the graded material is presened. In the initial phase of the fatigue process the fatigue damage is localized mainly in the corner of the cooling channel. Whereas the number of cycles to total failure of the considered structure associated with the damage of all elements across the structure section (N_f) appears to be much smaller than that number for the reference material.

5. CONCLUSIONS

The presented analysis is aimed at application of the simplified approach based on the continuum mechanics to modelling of the low cycle fatigue of functionally graded materials. The simulation of cyclic behaviour is assumed as updating data of static tensile characteristics for a point of the material in which damage occurs. All peak stress values (yield stress, ultimate tensile stress) are reduced follows accumulated damage rule associated with the plastic energy dissipation while the tangent modulus is kept constant.

The concept of FGM as a particle-reinforced metal-matrix composite with gradual change of the reinforcement fraction is used. The FGM is considered as a material consisting of homogeneous layers containing different volume fractions of the reinforcement. The variation of the reinforcement fraction changes the material properties for each layer. The different material properties are obtained according to modified rule of mixture.

The model was applied to the cooling channel of thruster used in space shuttles and rockets. The cooling system is actually subjected simultaneously to the thermo-mechanical loading. However, the mechanical cyclic loading was only considered at the constant maximum high temperature, 700K. The reasons for the “dog house” failure mode have been revealed. In the initial phase of the fatigue process the failure begins in the corner of the cooling channel. Next the damage appears at the inner hot surface and develops upwards towards the cold cooling channel. It leads to necking of the layer and results to totally failure of the cooling channel. In conclusion, the proposed FGM material

structure shows the shorter mechanical fatigue life than reference $CuAg_3Zr_{0.5}$ material.

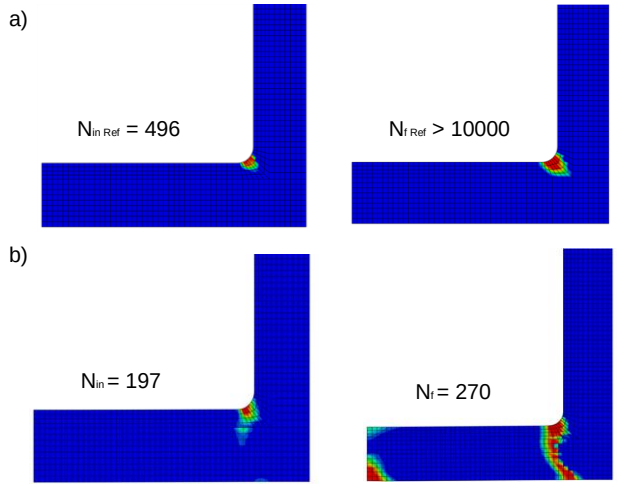

Fig. 9. The damage comparsion based on fatigue cycles between the references material and graded material: a) $CuAg_3Zr_{0.5}$ - references material; b) Al_2O_3-Cu - graded material

It should be pointed out that in the analysis presented in this paper some material deterioration due to erosion and blanching, say, that developes during the thruster service life and could have a significant effect on the fatigue life time were not considered. Since the resistance of the layered FGM with Al_2O_3 particles newly proposed for the thruster to those deteriorating actions is much greater than the resistance of the currently used $CuAg_3Zr_{0.5}$ material the relation between the actual fatigue life times for both materials might be quite different or even reversed to that given in Eq. (23).

REFERENCES

1. **Andrews J.S., Armstrong W. H**, (1974), Thrust Chamber Life Prediction, Boeing AeroSspace Company, (NASA-CB-144048).
2. **Baldwin E. E., Sokol G. J., Coffin L. E** (1957), Cyclic strain fatigue studies on AISI 347 stainless steel, *Proceedings, American Society for Testing and Materials*, 57, 567-586.
3. **Bennett J. A.** (1946), A study of the damaging effect of fatigue stressing on X4130 steel, *Proceedings, American Society for Testing and Materials*, 46, 693-714.
4. **Bernard-Connolly M., Bui-Quoc T., Biron A.** (1983), Multilevel strain controlled fatigue on a type 304 stainless steel, *ASME Journal of Engineering Materials and Technology*, 105, 188-194.
5. **Biron A., Bui-Quoc T.** (1981), Cumulative damage concepts with interaction effect consideration for fatigue or creep; a perspective, *In Transactions of the 6th International Conference on Structural Mechanical Reaction Technology*, Paris, France, L9/1.1-7.
6. **Bizon P. T., Thoma D. J., Halford G. R.** (1985), Interaction of high cycle and low cycle fatigue of Haynes 188 at 1400 F, *In Structure Integrity and Durability of Reusable Space Propulsion Systems*, NASA CP-2381. NASA Lewis Research Center, Cleveland, OH, pp. 129-138.
7. **Bluhm J.** (1962), A note on fatigue damage, *Materials Research and Standards*.
8. **Bui-Quoc T., Dubuc J., Bazergui A., Biron A.** (1971), Cumulative fatigue damage under strain controlled conditions, *Journal of Materials*, 6, 3, 718-737.
9. **Bui-Quoc T.** (1981), An interaction effect consideration in cumulative damage on a mild steel under torsion loading, Proceedings of the 5th International Conference on Fracture, *Pergamon Press*, 5, 2625-2633.
10. **Bui-Quoc T.** (1982), Cumulative damage with interaction effect due to fatigue under torsion loading, *Experimental Mechanics*, 22, 180-187.
11. **Bui-Quoc T.** (1982), A simplified model for cumulative fatigue damage with interaction effects, In Proceedings of the 1982 Joint Conference on Experimental Mechanics, *Society for Experimental Stress Analysis*, Brookfield Center, CT, 144-149.
12. **Carpenter R. D., Rabin B. H., Drake J.T.** (1993), Finite Element Analysis of Thermal residual Stresses at Graded Ceramic-Metal Interface, Part I. Model Description and Geometrical Effects, *J. Appl. Phys.*, Vol. 74, 2, 13010-1320.
13. **Chaboche J. L.** (1974), A differential law for nonlinear cumulative fatigue damage, In Materials and Building Research, Paris Institut Technique Du Batiment Et Des Travaus Publies, *Annales de l'ITBTP*, HS No. 39, 117-124.
14. **Chaboche J. L., Kaczmarek H.** (1981), On the interaction of hardening and fatigue damage in the 316 stainless steel, In Proceedings of the 5th International Conference on Fracture (ICF 5), Cannes, Vol. 3, *Pergamon Press*, Oxford, 1381-1393.
15. **Chaboche J. L.** (1982), Lifetime predictions and cumulative damage under high-temperature conditioned, *In Low-cycle Fatigue and Life Prediction*, ASTM STP 770, eds. C, Amzallag, B. N, Leis and P. Rabbe, *American Society for Testing and Materials*, Philadelphia, PA, 81-103.
16. **Chaboche J. L., Lesne P. M.** (1988), A non-linear continuous fatigue damage model, *Fatigue and Fracture of Engineering Materials and Structures*, 11, 1, 1-7.
17. **Coffin L. F.** (1956), Design aspects of high-temperature fatigue with particular reference to thermal stresses, *Transactions of the ASME*, 78, 527-532.
18. **Corten H. T., Dolon T. J.** (1956), Cumulative fatigue damage. In Proceedings of the International Conference on Fatigue of Metals, *Institution of Mechanical Engineering and American Society of Mechanical Engineers*, 235-246.
19. **Dubuc J., Bui-Quoc T., Bazergui A., Biron A.** (1971), Unified theory of cumulative damage in metal fatigue. W.R. C. Bulletin, 162, 1-20.
20. **Dunne F., Petrinic N.** (2005), Introduction to Computational Plasticity,Oxford University Press, New York
21. **French H. J.** (1933), Fatigue and hardening of steels, *Transactions, American Society of Steel Treating*, 21, 899-946.
22. **Freudenthal A. M.** (1956), Physical and statistical aspects of cumulative damage, *Springer-Verlag*, Berlin, 53-62.
23. **Freudenthal A. M., Heller R. A.** (1959), On stress interaction in fatigue and a cumulative damage rule, *Journal of the Aerospace Sciences*, 26, 7, 431-442.
24. **Gatts R. R.** (1961), Application of a cumulative damage concept to fatigue, *ASME Journal of Basic Engineering*,83,529-540.
25. **Gatts R. R.** (1962), Cumulative fatigue damage with random loading, *ASME Journal of Basic Engineering*, 84, 403-409.
26. **Glinka G, Shen G, Plumtree A.** (1995), A multiaxial fatigue strain energy density parameter related to the critical plane, *Fatigue Fract Eng Mater Struct*; 18:37–46.
27. **Golos K., Ellyin F.** (1987), Generalization of cumulative damage criterion to multilevel cyclic loading, *Theoretical and Applied Fracture Mechanics*, 7, 169-176.
28. **Golos K., Ellyin F.** (1988), A total strain energy density theory for cumulative fatigue damage, *ASME Journal of Pressure Vessel Technology*, 110, 36-41.
29. **Golos K., Ellyin F.** (1989), Total strain energy density as a fatigue damage parameter, *In Advances in Fatigue Science and Technology, Proceedings of the NATO Advanced Study Institute*, cd. C. M. Branco and L. G. Rosa. Kluwer Academic, 849-859.

30. **Grover H. J.** (1960), An observation concerning the cycle ratio in cumulative damage, *American Society for Testing and Materials*, Philadelphia, PA , 120-124.
31. **Halford G. R.** (1966), The energy required for fatigue, *Journal of Materials*, 1(1), 3-18.
32. **Halford G. R., Manson S. S.** (1985), Reexamination of cumulative fatigue damage laws, *In Structure Integrity and Durability of Reusable Space Propulsion Systems*, NASA CP-2381. NASA, 139-145.
33. **Henry D. L.** (1955), A theory of fatigue damage accumulation in steel, *Transactions of the ASME*, 77, 913-918.
34. **Hua C. T., Socie D., F.** (1984), Fatigue damage in 1045 steel under constant amplitude biaxial loading, *Fatigue of Engineering Materials and Structures*, 7, 3, 165-179.
35. **Inglis N. P.** (1927), Hysteresis and fatigue of Wohler rotating cantilever specimen, *The Metallurgist*, 23-27.
36. **Kachanov L. M.** (1969), Time to the rupture process under creep conditions, *Izvestiia AN SSSR*, 1984, OTN(8), 26-31.
37. **Kommers J. B.** (1945), The effect of overstress in fatigue on the endurance life of steel, *Proceedings, American Society for Testing and Materials*, 45, 532-541.
38. **Kujawski D., Ellyin F.** (1984), A cumulative damage theory of fatigue crack initiation and propagation, *International Journal of Fatigue*, 6, 2, 83-88.
39. **Lagoda T**. (2001), Energy models for fatigue life estimation under uniaxial random loading. Part I: The model elaboration. *Int. J. Fatigue*; 23:467–80.
40. **Langer B. F.** (1937), Fatigue failure from stress cycles of varying amplitude, *ASME Journal of Applied Mechanics*, 59, AI60-AI62.
41. **Leis B. N.** (1988), A nonlinear history-dependent damage model for low cycle fatigue, *Low Cycle Fatigue*, ASTM STP 942.
42. **Leis B. N.** (1997), An energy-based fatigue and creep-fatigue damage parameter, *Journal of Pressure Vessel and Technology*, *ASME Transactions*, 99(4), 52-+-533.
43. **Lemaitre J., Chaboche J. L.** (1978), Aspect phenomenologique de la ruptutre par endommagement, *Journal Mecanique Appliquee*, 2(3), 317-365.
44. **Lemaitre J., Plumtree A.** (1979), Application of damage concepts to predict creep-fatigue failures, *ASME Journal of Engineering Materials and Technology*, 101, 284-292.
45. **Lemaitre J., Chaboche J. L.** (1990), Mechanics of Solid Materials, trans. B. Shrivastava, *Cambridge University Press*, Cambridge, UK.
46. **Li C., Qian Z. and Li G.** (1989), The fatigue damage criterion and evolution equation containing material microparameters, *Engineering Fracture Mechanics*, 34(2), 435-443.
47. **LLorca J.** (2002), *Fatigue of particle-and whisker-reinforced metal-matrix composites*, Progress in Materials Science, 47, 283-353.
48. **Machlin E. S.** (1949), Dislocation theory of the fatigue of metals, N.A.C.A. Report 929.
49. **Manson S. S.** (1966), Interfaces between fatigue, creep, and fracture, *International Journal of Fracture Mechanics*, 2, 328-363.
50. **Manson S. S., Halford G. R.** (1981), Practical implementation of the double linear damage rule and damage curve approach for treating cumulative fatigue damage, *International Journal of Fracture*, 17(2), 169-192.
51. **Manson S. S., Halford G. R.** (1983), Complexities of high-temperature metal fatigue: some steps toward understanding, *Israel Journal of Technology*, 21, 29-53.
52. **Marco S. M., Starkey W. L.** (1954), A concept of fatigue damage, *Transactions of the ASME*, 76, 627-632.
53. **Miner M. A.** (1945), Cumulative damage in fatigue. *Journal of Applied Mechanics*, 67, AI59-AI64.
54. **Morrow J. D.** (1965), Cycle plastic strain energy and fatigue of metals. In Internal Friction, Damping, and Cyclic Plasticity, ASTM STP 378, *American Society for Testing and Materials*, Philadelphia, PA, 45-84.
55. **Niu X. D.** (1987), Memory behavior of stress amplitude responses and fatigue damage model of a hot-rolled low carbon steel. In Mechanical Behavior of Materials-V, *Proceedings of the Fifth International Conference*, Vol. 1, ed. M. G. Yan, S. H. Zhang and Z. M. Zheng., *Pergamon Press*, Oxford, 685-690.
56. **Niu X., Li G. X., Lee H.** (1987), Hardening law and fatigue damage of a cyclic hardening metal, *Engineering Fracture Mechanics*, 26(2), 163-170.
57. **Palmgren A.** (1924), Die Lebensdauer von Kugellagern, *Veifahrenstechinik*, Berlin, 68, 339-341.
58. **Plumtree A. and O'Connor B. P. D.** (1989), Damage accumulation and fatigue crack propagation in a squeeze-formed aluminum alloy, *International Journal of Fatigue*, 11, 4, 249-254.
59. **Rabotnov Y. N.** (1969), Creep Problems in Structural Members, *North-Holland*, Amsterdam.
60. **Radhakrishnan V. M.** (1978), Cumulative damage in low-cycle fatigue, *Experimental Mechanics*, 18, 8, 292-296.
61. **Radhakrishnan V. M.** (1980), An analysis of low cycle fatigue based on hysteresis energy, *Fatigue of Engineering Materials and Structures*, 3, 75-84.
62. **Richart F. E., Newmark N. M.** (1948), A hypothesis for the determination of cumulative damage in fatigue, *Proceedings, American Society for Testing and Materials*, 48, 767-800.
63. **Seweryn A, Buczyński A, Szusta J.** (2008), Damage accumulation model for low cycle fatigue, *Int. J. Fatigue*, 1, 30:756-65.
64. **Shanley F. R.** (1952), A theory of fatigue based on unbonding during reversed slip, Report P-350, *The Rand Corporation*, Santa Monica.
65. **Socie D. F., Fash J. W., Leckie F. A.** (1983), A continuum damage model for fatigue analysis of cast iron, *In Advances in Life Prediction Methods*, ed, D. A. Woodford and J, R. Whitehead, *The American Society of Mechanical Engineers*, New York, 59-64.
66. **Sutton Ch. E.** (2009), Fatigue damage assessment of particle-reinforced metal matrix composite materials under uniaxial and multiaxial loadings conditions, *Digital Commons @ Ryerson*, Toronto, Ontario.
67. **Tamura I., Tomota Y., Ozawa H.** (1973), Strength and ductility of Fe–Ni–C alloys composed of austenite and martensite with various strength, *Proceedings of the Third International Conference on Strength of Metals and Alloys*, Vol. 1. Cambridge: Institute of Metals; 611–5.
68. **Valluri S. R.** (1961), A unified engineering theory of high stress level fatigue, *Aerospace Engineering*, 20, 18-19.
69. **Valluri S. R.** (1961), A theory of cumulative damage in fatigue. Report No. ARL 182, *Aeronautical Research Laboratory, Office of Aerospace Research*, United States Air Force.
70. **Weinacht D. J., Socie D. F.** (1987), Fatigue damage accumulation in grey cast iron, *International Journal of Fatigue*, 9, 2, 79-86.
71. **Wheeler O. E.** (1972), Spectrum loading and crack growth, *ASME Journal of Basic Engineering*, D94(1), 181-186.
72. **Willenborg J., Engle R. M., Wood H. A.** (1971), A crack growth retardation model using an effective stress concept, AFFDL TM71-I-FBR.
73. **Williamson R. L., Rabin B. H., Drake J. T.** (1993), Finite Element Analysis of Thermal residual Stresses at Graded Ceramic-Metal Interface, Part I. Model Description and Geometrical Effects, *J. Appl. Phys.*, Vol. 74, 2, 13010-1320.
74. **Zuchowski R.** (1989), Specific strain work as both failure criterion and material damage measure, *Res Mechanica*, 27(4), 309-322.

Acknowledgment: The results presented in this paper have been obtained within the project "KomCerMet" (contract no. POIG.01.03.01-14-013/08-00 with the Polish Ministry of Science and Higher Education) in the framework of the Operational Programme Innovative Economy 2007-2013 and within the EU FP7 Project "Micro and Nanocrystalline Functionally Graded Materials for Transport Applications" (MATRANS) under Grant Agreement no. 22886.

RHEOLOGICAL PROPERTIES OF MR FLUIDS RECOMMENDED FOR USE IN SHOCK ABSORBERS

Bogdan SAPIŃSKI[*], Wojciech HORAK[**]

[*]AGH University of Science and Technology, Faculty of Mechanical Engineering and Robotics, Department of Process Control, Al. Mickiewicza 30, 30-059 Kraków, Poland
[**]AGH University of Science and Technology Faculty of Mechanical Engineering and Robotics, Department of Machine Design and Technology, Al. Mickiewicza 30, 30-059 Kraków, Poland

deep@agh.edu.pl, horak@agh.edu.pl

Abstract: The paper summarises the results of laboratory testing of rheological behaviour of (magnetorheological) MR fluids designed for use in shock absorber and vibration dampers. The experiments used a rotational rheometer with an extra chamber inside which a uniform magnetic field can be generated. Underlying the description of rheological properties of fluids is the Herschel-Bulkley's model of viscous-plastic substances. The aim of the experiment was to determine the shear stress, yield stress, the yield factor and the power-law exponent depending on the magnetic flux density, followed by the comparative study of rheological parameters of investigated fluids.

Key words: MR Fluids, Rheological Characteristics, Herschel-Bulkley's Model, Shear Stress, Yield Stress

1. INTRODUCTION

MR fluids are suspensions of ferromagnetic particles with the diameter 1-20μm in a carrier fluid which does not exhibit any magnetic properties. The fraction of ferromagnetic particles in a MR fluid ranges from 10 to 15 % by volume. These particles are typically made of iron oxides or iron, nickel, cobalt alloys. Saturation magnetisation of their material is about 2.2T. The choice of the carrier fluid depends on the projected application requirements of MR fluids. Most widely used carrier fluids include mineral or synthetic oils, some of them are based on water, polyesters or polyeter (Cheng et al., 2009; Gorodkin et al., 2009; Jonsdottir et al., 2010; Phule, 2001). MR fluids may contain some additives to prevent sedimentation and aggregation of particles and to improve their lubrication properties. Some admixtures, mostly surfactants are added to improve the fluid stability. These include polymers or carboxyl acids (Du et al., 2010).

The unique feature of a MR fluid is that its rheological properties change under the action of the applied magnetic field. This change is instantaneous (the response time of MR fluids is of the order of several milliseconds) and reversible. Besides of their unique property, MR fluids are now widely used in devices with the controllable operating parameters, such as couplings, brakes, vibration dampers or shock absorbers (Gołdasz and Sapiński, 2011; Olabi and Grunwald, 2007; Sapiński, 2006). Presently, most widespread industrial applications of MR fluids include shock absorbers and vibration dampers. The structure and operating principles of MR shock absorbers is outlined in the comprehensive work (Zhu et al., 2012).

In the absence of magnetic field, MR fluid behaves like typical non-colloidal suspensions. Rheological properties of MR fluids in this state are dependent mostly on rheological parameters of the base fluid, properties of solid particles (size, shape and volumetric proportion).

Under the action of a magnetic field, the particles arrange themselves in spatial, columnar structures, along the magnetic field lines. In the macro-scale, that is observed as a change of rheological properties of the fluids. Through the application of magnetic field, the yield stress can be increased to 100kPa or even to 1400kPa providing the strain state of the fluid is modified accordingly (Olabi and Grunwald, 2007; Wang et al., 2011).

The MR effect, i.e. the change of rheological properties of the fluid under the action of magnetic field is associated mostly with magnetic properties of the material from which the particles are made. In the context of magnitude of MR effect, of particular importance is the saturation magnetisation of the particle material and the volumetric proportion of ferromagnetic particles in a MR fluid.

Rheological properties of a MR fluid are determined by several factors: rheological parameters of the base fluid, concentration and density of ferromagnetic particles, their dimensions, shape and magnetic properties. When analysing the behaviour of MR fluids, the effects of the presence of surfactants, thermal interactions and distribution of the applied magnetic field have to be taken into account.

Several MR fluids are now commercially available that are dedicated for use in vibration damping systems. Because of the variety of adopted measurement methods, the data provided in manufacturers' specifications may not allow a direct comparison between rheological properties of several fluids. The purpose of the present study is to obtain the characteristic of MR fluids and to compare the rheological properties of MR fluids recommended for use in shock absorbers.

2. MR FLUIDS RECOMMENDED FOR USE IN SHOCK ABSORBERS

Depending on their applications, commercially available MR fluids intended for use in system with controllable process parameters can be categorised into two groups: MR fluids for use in shock absorbers and those recommended for use in couplings and brakes. The main difference between their properties lies in the

level of the achievable yield stress. For fluids designed for use in shock absorbers, the value of yield stress is less than 20kPa, for fluids employed in couplings and brakes the yield stress can exceed 50kPa. Apart from differences in composition of the two fluid types (addition of some improvers), the volumetric proportion of ferromagnetic particles will differ, too (20% for MR fluids used in shock absorbers and over 40% in those applied in couplings and brakes).

Selection of a MR fluid to be used in a shock absorber should be optimised in terms of such parameters as: variability range of the yield stress under the action of magnetic field, stability of MR fluid (resistance to oxidation), resistance to sedimentation, ease of application, tribological properties and durability as well as the admissible temperature range for fluid operation. Another vital parameter of a MR fluid that impacts on the performance of shock absorbers is fluid viscosity in the absence of magnetic field.

The behaviour of MR fluids is typically governed by models of viscous-plastic substances, including the Bingham model, the bi-viscous model and the Herschel-Bulkley's model (Gołdasz, 2012). The first two models give an approximate description of the MR fluid behaviour whilst the Herschel-Bulkley's power law formula enables a more accurate representation of yield stress. The model can be expressed as:

$$\tau = \tau_0 + \eta \dot{\gamma}^n \tag{1}$$

where: τ – shear stress, τ_0 – yield stress, η – visosity, $\dot{\gamma}$– shear rate, n – power-law exponent

Depending on the power law exponent, the model governs various aspects of fluid behaviour. For shear thinning substances n<1, whilst for shear thickening ones *n*>1. For *n*=1, this model becomes an equivalent of the Bingham model.

3. EXPERIMENTS

Testing is done on three MR fluids recommended for use in shock absorbers: MRF-122EG (Lord Corporation) two manufactured by the BASF company (Basonetic 2040, Basonetic 4035) (http://www.basonetic.com/, http://www.lord.com/). Similar density of tested fluids is indicative of similar proportion of solid particles. Selected properties of investigated fluids are compiled in Tab. 1.

Tab. 1. Properties of investigated MR fluids

MR fluid	Density	Saturation magnetization
	[g/cm^3]	[kA/m]
Basonetic 2040	2.47	~418
Basonetic 4035	2.68	~417
MRF-122EG	2.38	~359

The experiments were performed using a rotational rheometer Physica MCR 301 (http://www.anton-paar.com/) complete with a test cell enabling the experiments to be conducted under a uniform magnetic field. The schematic diagram of the test cell is shown in Fig. 1.

A MR fluid sample (2) was placed between the electromagnet cores (4) and a rotational plate in a rheometer (1). The flux density was altered through the change of current intensity in the electromagnet windings (3). The closed chamber formed a magnetic circuit controlling the field distribution in such manner that field lines should be perpendicular to the shearing direction.

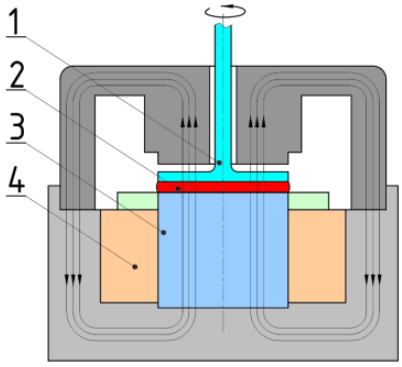

Fig. 1. Schematic diagram of the test cell

The testing was done in the experimental setup incorporating two parallel plates with the diameter Ø 20mm, under the magnetic field with the flux density B=0-0.5T in the temperature-stabilised conditions (at the temperature 25°C). The gap height was h=0.5 mm and the volume of the tested fluid samples was 175µl.

The experiments were conducted in two stages. In the first stage the shear stress curves were obtained under the linearly increasing flux density and for the constant shear rate 1001/s. In the second stage the yield curves were obtained for the constant flux density B: 0, 0.1, 0.2, 0.3, 0.4, 0.5T. The results give us a better insight into rheological behaviour of investigated fluids.

Measurement data were then subjected to the correction procedure by the method suggested by Soskey and Winter (1984), on account of the non-Newtonian behaviour of MR fluids and the plate-plate configuration.

Fig. 2 shows the flow curves of investigated MR fluids, obtained in the absence of magnetic field.

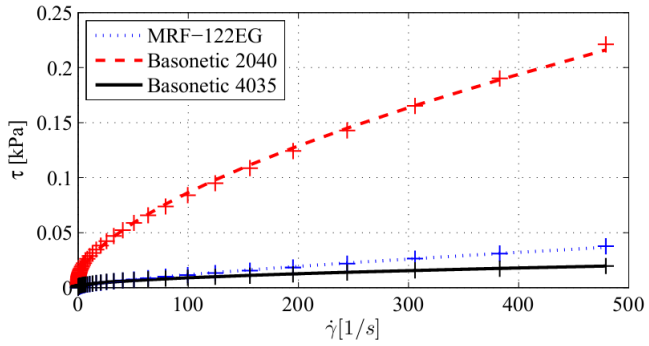

Fig. 2. Flow curves (B=0T)

The values of shear stress obtained for Basonetic 4035 and MRF-122EG were relatively low, which suggests the low viscosity of the base fluid. In the case of Basonetic 2040, a yield stress limit is clearly revealed, which indicates it is based on a high-viscosity oil.

The values of the Herschel-Bulkey's model parameters obtained for the investigated fluids in the absence of magnetic field are summarised in Tab. 2. Thus obtained yield stress plots are found to be non-linear.

Differences between the values of the H-B exponent n may be indicative of the influence that the solid phase (ferromagnetic

particles) has on the behaviour of the MR fluid in the absence of magnetic field. The values n<1 are characteristic of typical non-colloidal shear thinning suspensions.

Tab. 2. Parameters of the Herschel-Bulkey's model, (B=0 T)

MR fluid	Yield stress τ_0	Viscosity η	H-B exponent n
	[Pa]	[Pa·s]	[-]
Basonetic 2040	6.45	4.7	0.61
Basonetic 4035	0.32	0.83	0.51
MRF-122EG	0.48	0.37	0.74

Fig. 3 shows the shear stress plots for investigated MR fluids under the linearly increasing magnetic flux density and for the fixed shear rate ($\dot{\gamma}$=1001/s). The range of shear stress values under the specified conditions was similar for all fluids. Differences in the stress values are observed when the flux density was B≥0.2T.

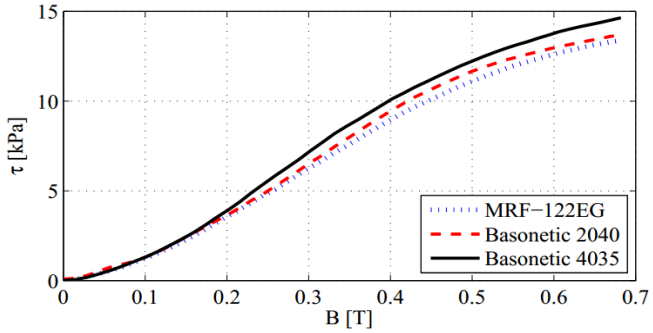

Fig. 3. Shear stress vs magnetic flux density ($\dot{\gamma}$=1001/s)

The highest levels of the shear stress are registered for Basonetic 4035, which features low zero-state viscosity and high saturation magnetisation.

Fig. 4 shows the yield stress curves obtained by applying the Herschel-Bulkey's model to approximation of measurement points determined under variable flux densities.

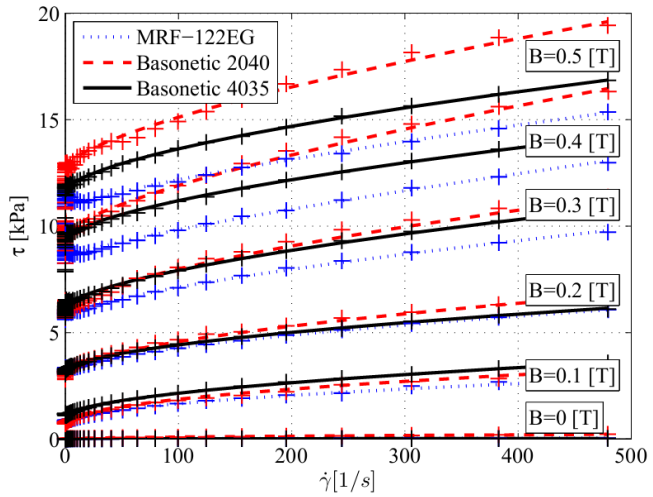

Fig. 4. Flow curves approximated by the Herschel-Bulkley's model

It appears that the adopted rheological model agrees well with the measurement data. Model coefficients used in further analyses are obtained by approximation.

The plots of yield stress obtained by the Herschel-Bulkey's model are shown in Fig. 5. At low levels of magnetic flux density, all fluids exhibit similar yield stress. More considerable differences between the values of this parameters for particular MR fluids are registered for B>0.3T. The lowest values of the yield stress are registered for the fluid with the lowest saturation magnetisation

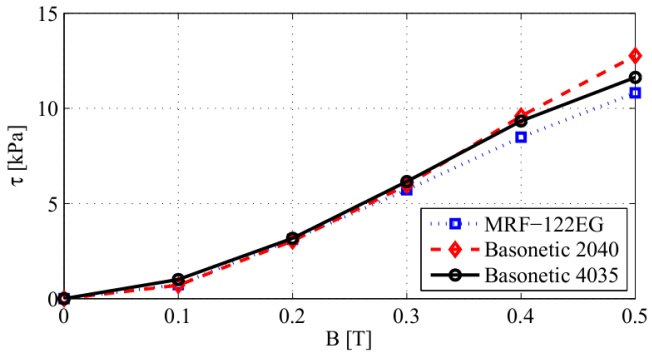

Fig. 5. Yield stress vs. magnetic flied density; Herschel-Bulkley's model

Fig. 6 shows the variability of the yield factor of the analysed rheological model.

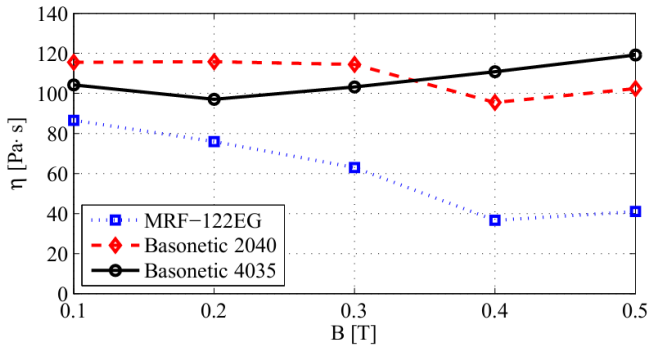

Fig. 6. Viscosity vs. magnetic flied density; Herschel-Bulkley's model

For MR fluids featuring similar magnetisation (Basonetic 2040, Basonetic 4035) in the investigated range of magnetic flux density, the values of the yield factor are similar. For the fluid having the lowest saturation magnetisation (MRF-122EG), the yield factor tends to decrease with an increased magnetic flux density.

Fig. 7 shows the plots of the exponent n in Herschel-Bulkey's model (H-B exponent).

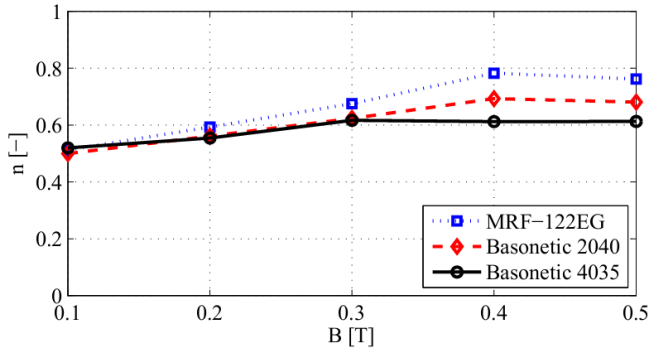

Fig. 7. Power-law exponent vs. magnetic flied density

The rheological behaviour of investigated fluids is characteristic of shear thinning fluids (n<1). It appears that the value of the exponent n tends to increase with an increase in the magnetic flux density. That indicates the lower level of shear thickening of investigated fluids under higher flux densities.

One has to bear in mind that in the model applied in Eq (1), the variability of the yield curve is associated with both the viscoisty (η) and the power-law exponent (n).

4. SUMMARY

W The paper summarises the results of laboratory testing of rheological behaviour of commercially available MR fluids (Basonetic 2040, Basonetic 4035, MRF-122EG), differing in their zero-state viscosity and in the level of saturation magnetisation.

Testing of rheological parameters of selected MR fluids indicates their similar behaviour. Plots of investigated parameters reveal that the considered range of magnetic flux density will not provide for saturation magnetisation of tested fluids. It is reasonable to expect a further increase of the yield limit, at higher levels of the magnetic flux density.

The upper limit of yield stress variability under the defined test conditions approaches 12kPa.

Most significant differences between the behaviour of particular MR fluids are revealed in the absence of magnetic field and at high levels of magnetic flux density. At low flux densities, the differences between properties of MR fluids may be attributable to differences in their composition and rheological parameters of the base fluid. At higher values of magnetic flux density, the observed differences are mostly due to magnetic properties and differences in volumetric proportion of ferromagnetic particles in the MR fluids.

REFERENCES

1. **Cheng H., Wang J., Zhang Q., Werely N.** (2009), Preparation of composite magnetic particles and aqueous magnetorheological fluids, *Smart Materials and Structures*, 18, 8, 1-4.
2. **Du C., Chen W., Wan F**. (2010), Influence of HLB parameters of surfactants on properties of magnetorheological fluid, *Advanced Materials Research*, 97-101, 843-847.
3. **Gołdasz J.** (2012), *Magnetorheological Shock Absorbers: Automotive Context*, Wydawnictwo Politechniki Krakowskiej.
4. **Gołdasz J., Sapiński B.** (2011), Modeling of Magnetorheological Mounts in Various Operation Modes, *Acta Mechanica and Automatica*, Vol. 5, No. 4, *29-39.*
5. **Gorodkin S., James R., Kordonski W.** (2009), Magnetic properties of carbonyl iron particles in magnetorheological fluids*, Journal of Physics: Conference Series*, 149(1), 1-4.
6. **Jonsdottir F., Gudmundsson K. H., Dijkman T. B., Thorsteinsson F., Gutfleisch O.** (2010), Rheology of perfluorinated polyether-based MR fluids with nanoparticles, *Journal of Intelligent Material Systems and Structures*, 21, 11, 1051-1060.
7. **Olabi A., Grunwald A.** (2007), Design and application of magneto-rheological fluid, *Materials and Design*, 28(10), 2658-2664.
8. **Phule P**. (2001), Magnetorheological (MR) fluids: Principles and applications, *Smart Materials Bulletin*, 2001(2), 7-10.
9. **Sapiński B.** (2006), *Magnetorheological dampers in vibration control*, Uczelniane Wydawnictwa Naukowo-Dydaktyczne AGH, Kraków.
10. **Soskey P. R,. Winter H. H.** (1984), Large step shear strain experiments with parallel disk rotational rheometers, *Journal of Rheology,* 28, 625–645.
11. **Wang H., Zhang B. J., Liu X. Z., Luo D. Z., Zhong S. B.** (2011), Compression resistance of magnetorheological fluid, *Advanced Materials Research*, 143-144, 624–628.
12. **Zhu X., Jing X., Li Ch.** (2012), Magnetorheological fluid dampers: A review on structure design and analysis, *Journal of Intelligent Material System and Structures*, 23(8), 839-873.
13. Anton Paar, http://www.anton-paar.com/
14. BASF The Chemical Company, http://www.basonetic.com/
15. LORD Corporation, http://www.lord.com/

This research is supported by the National Centre for Research and Development under grant No. PBS 1/A6/3/2012.

INVESTIGATION OF MR FLUIDS IN THE OSCILLATORY SQUEEZE MODE

Bogdan SAPIŃSKI[*], Wojciech HORAK[**], Marcin SZCZĘCH[**]

[*]AGH University of Science and Technology, Faculty of Mechanical Engineering and Robotics, Department of Process Control, Al. Mickiewicza 30, 30-059 Kraków, Poland
[**]AGH University of Science and Technology Faculty of Mechanical Engineering and Robotics, Department of Machine Design and Technology, Al. Mickiewicza 30, 30-059 Kraków, Poland

deep@agh.edu.pl, horak@agh.edu.pl, szczech@agh.edu.pl

Abstract: The paper summarises the results of laboratory testing of three commercially available magnetorheological (MR) fluids operated in the oscillatory squeeze mode. Tested fluids include the Basonetic 204 and Basonetic 4035 (BASF) and MRF-122EG (Lord Corporation). The oscillatory squeeze mode produces large forces at small displacements. This feature may be well utilised in fabrication of new MR devices. The purpose of the experiments was to evaluate the suitability of MR fluids for applications in MR vibration dampers being developed under the current research project. The results enable a comparative analysis of investigated fluids and verification of phenomena encountered in the oscillatory squeeze mode and reported in the literature.

Key words: MR Fluid, Oscillatory Squeeze Mode, Experiments

1. INTRODUCTION

MR fluids are suspensions of ferromagnetic particles in a carrier liquid (typically oil or water) whose rheological properties can be controlled through the action of a magnetic field. The fluids can be operated in the valve mode (used in vibration dampers (Sapiński, 2006)), in the direct shear mode (used in brakes and couplings) or in the squeeze mode (used in dampers and bearings (Bonneau and Frene, 1997; Farjoud et al., 2008; Guldbakke and Hesselbach, 2006; Mazlan, 2008)). Literature on the subjects abounds in reports on the valve and coupling modes whilst the squeeze mode still poses a major challenge to researchers.

Properties of MR fluids operated in the squeeze mode are dependent on application requirements. In the case of vibration damping systems, of particular importance is the ability to generate significant forces when MR fluid is displaced from the squeeze zone and to provide for a wide variability range of rheological parameters.

This paper summarises the laboratory testing of selected MR fluids operated in the oscillatory squeeze mode with a constant contact area between the sample and plate. Since MR fluids dedicated directly to this operation mode are not available commercially, experiments were done on samples of MR fluids which, according to the manufacturers' specifications, are recommended for use in vibration dampers.

The purpose of the experiments was to evaluate the suitability of those MR fluids for use in squeeze mode vibration dampers, which are investigated by the authors under the current research project.

2. SQUEEZE MOEDE

Two cases of the squeeze mode operation of MR fluids are considered: with the constant volume (Fig. 1a) and with the constant contact area (Fig. 1b). Stresses obtained for MR fluid when squeezed approach 100-150kPa with relatively small displacements of the order of several millimetres. These features can be used to develop novel devices using the MR fluid technology (Bonneau and Frene, 1997; Gołdasz and Sapiński, 2011; Zhang et al., 2011).

There are only few studies exploring the squeeze mode of the MR fluid operation and the involved phenomena. In the work Horak (2013), attention is given to the effect of the displaced carrier fluid from the squeeze zone. As a result, the properties of the MR fluid will change during its operation in the squeeze mode.

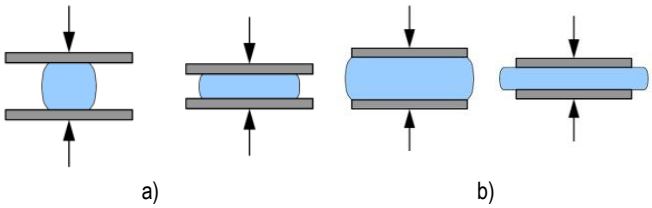

Fig. 1. Squeeze of the MR fluid: a) with the constant volume, b) with the constant contact area

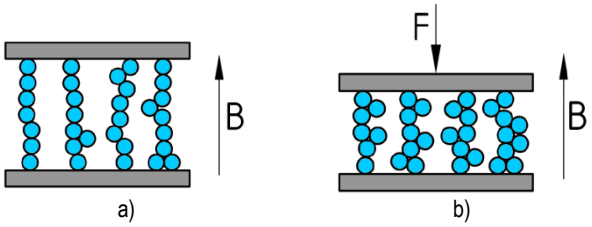

Fig. 2. MR fluid particles a) column-like chain structures, b) deformation due to compression

Another phenomenon observed when a MR fluid is operated in the squeeze mode is the change of the fluid structure. In the presence of a magnetic field, ferromagnetic particles are arranged in column-like chain structures (Fig. 2a) which get deformed due to compression (Horak, 2013; Tao, 2011) (Fig. 2b).

When operated in the squeeze mode, the MR fluid provides increased resistance to compressive loading and its yield stress tends to increase. As a result, the yield stress of the MR fluid may increase even 6-times (Tao, 2011).

Another aspect of the MR fluid behaviour in the squeeze mode is the clumping effect (Farjoud et al., 2008; 2011) which involves aggregation of MR fluid particles leading to formation of ferrous particle aggregate clumps in the fluid. As a result, progressively increasing force will develop in consecutive test runs.

Moreover squeeze force is also influenced by pressure generated in the MR fluid under the action of the applied magnetic field.

3. EXPERIMENTS

3.1. Examined fluids

Testing is done on three MR fluids, two manufactured by the BASF Company (Basonetic 2040, Basonetic 4035) and MRF-122EG, manufactured by Lord Corporation (http://www.basonetic.com/, http://www.lord.com/). The choice of those particular fluids was prompted by the intention to conduct an experiment on a MR fluid with a relatively low volumetric density (<3 g/cm^3). Similar density of tested fluids is indicative of similar solid fraction. The percentage of ferromagnetic particles in MR suspension is an important factor affecting the behaviour of the MR fluids.

MR fluids Basonetic 4035 and MRF-122Eg have a similar viscosity in the absence of the magnetic field (indicated by similar viscosity of the carrier fluid) but differ significantly in the level of saturation magnetisation. Basonetic 2040 features a higher zero-state viscosity and its saturation magnetisation level is approaching that displayed by Basonetic 4035. Selected properties of fluids used in tests are summarised in Tab. 1.

Tab. 1. Properties of MR fluids

MR fluid	Density	Dynamic viscosity (B=0 [T], $\dot{\gamma}$=100 [1/s])	Saturation magnetization
	[g/cm^3]	[Pa·s]	[kA/m]
Basonetic 2040	2.47	0.956	418
Basonetic 4035	2.68	0.106	417
MRF-122EG	2.38	0.127	359

3.2. Experimental set-up

Tests were performed in the experimental set-up shown schematically in Fig. 3 (National Science Centre, contract number 1185/B/T02/2011/40). Testing device consist of a frame on which a linear servo-motor (1) is mounted, enables to change the position of the measuring plate with the accuracy 0.001mm. A force sensor (2) is attached to the motor, used for measuring the tensile and compression forces. The sample of the MR fluid was placed inside the test cell (3).

The investigated sample of MR fluid (5) was placed between the electromagnet cores (7) and a movable plate made of a paramagnetic material (4). The magnetic circuit is closed by the chamber housing (6). The applied magnetic field induction is altered by varying the current intensity in the electromagnet coil (8). In the electromagnet core and in the housing the ducts are made to allow the flow of the cooling fluid, which ensures the temperature stabilisation of the system. All experiments were conducted at the constant temperature 25°C.

A PC with the dedicated software (LabView version 2010) enables the control of position and speed of the linear motor and steering of the electromagnet power supply, as well as data acquisition.

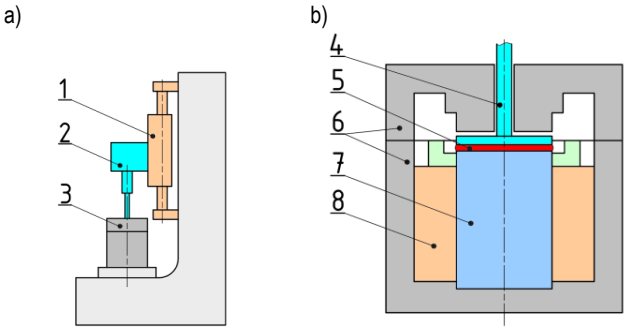

Fig. 3. Schematic diagram: a) experimental set-up, b) test cell

The schematic of the squeeze flow geometry is shown in Fig. 4. A mobile plate with the diameter Ø 45mm was placed between the electromagnet core and the cell housing, having identical diameter. The height of the gap between the core and the cell cover is h_g=10mm, the sample volume 1.6ml and the initial height of the gap is h_0=1mm. The amplitude of the applied triangular excitation inducing the plate position is Δh=0.2mm.

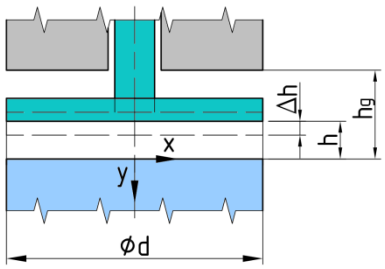

Fig. 4. Schematic of geometry

Experiments were performed in the presence of the magnetic field with the flux density B: 70, 100, 140, 200 and 270 [mT] under the applied excitation with the frequency f=0.1 and 0.5 [Hz], corresponding to the squeeze rate 0.04 and 0.02 [mm/s]. The squeeze force was assumed to have the positive sign.

3.3. Results

Fig. 5 shows plots of squeeze force and of the applied excitation (changes in the plate's position) for one of the MR fluids (MRF-122EG) and for various levels of magnetic flux density. The plots of displacement excitations for f=0.1 and 0.5Hz are slightly different, which is associated with the accuracy of level involved in the linear motor executing the pre-set operation pattern.

The relationship between the squeeze force (F) and change of the gap height (Δh) is shown in Fig. 5, 6 and 7. For all investigated fluids, during the return movement of the plate (gap increase), the squeeze force rapidly decreases, going down to its initial level.

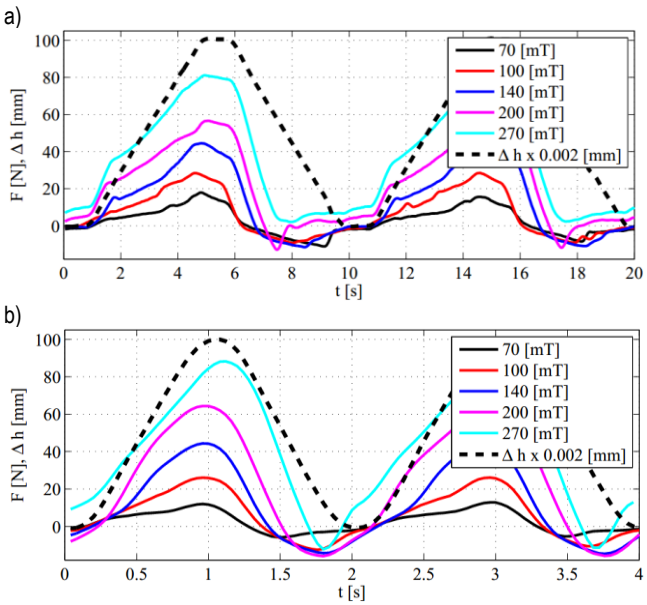

Fig. 5. Squeeze force and plate displacement vs. time; MRF-122EG; a) f=0.1Hz, b) f=0.5Hz

For flux density B<100mT, the force increase is linear for the fluids Basonetic 4030 and MRF-122EG. In the case of the fluid Basonetic 2040, however, a dramatic force increase was registered in the final phase of the squeezing process.

For flux density B>140mT, a two- stage force increase was observed for MRF-122EG and Basonetic 4035. In the first stage the squeeze force increases rapidly and then begins to increase linearly, at a lower rate, finally reaching its maximal value. Revealed differences between force vs. gap height plots obtained for MR fluids differing in viscosity of their carrier fluids may be indicative of the influence that the structure of the fluid has on the process of squeezing. In Basonetic 2040 (based on a high-viscosity oil), formation of chain structures is hindered because of higher resistance to motion experienced by ferromagnetic particles. In the case of various MR fluids subjected to magnetic field with the same flux density, those with less extended particles structures will experience squeezing.

For the fluid featuring the highest zero-state viscosity (Basonetic 2040), the squeeze frequency does not significantly affect the registered force pattern. The influence of the squeeze rate on the squeeze force is revealed only in fluids whose carrier fluid has lower viscosity (MRF-122EG and Basonetic 4035). This behaviour of MR fluids may be indicative of the influence that the rate of the chain structure formation has on the squeezing force. A high squeeze frequency shortens the time needed by the MR fluid particles to form a chain structure. In MR fluids containing low-viscosity carrier fluids formation of chain structures will take less time.

For flux density B=270mT, a non-zero force is registered whilst the moving plate returns to its initial position. This force is the consequence of pressure developed in the MR fluid due to the action of a magnetic field. A thorough analysis of this phenomenon is presented in the work Salwiński and Horak (2012).

The plots of maximal squeezing force are provided in Fig. 9. No matter what the squeezing rate, for lower flux densities the greatest resistance to squeezing is registered for fluids with highest viscosity. This may by cause to the fact that under the action of weaker fields, the carrier fluid viscosity becomes the major determinant of the MR fluid behaviour. High viscosity of the carrier fluid may be responsible for lower values of the maximal squeeze force registered in measurements taken at higher flux densities. Most probably, high viscosity of the carrier fluid impacts on the dynamics of MR particles forming the chain structures, that is why at the instant the squeezing begins, the less developed particle structure will get deformed.

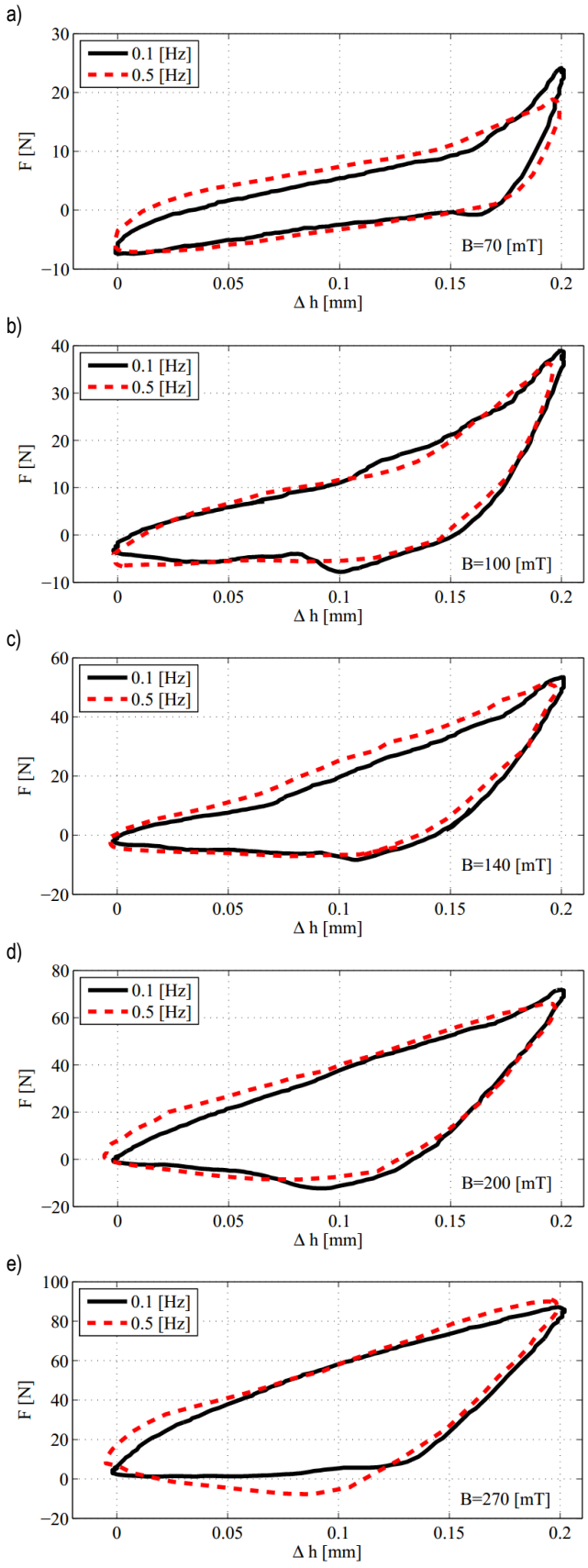

Fig. 6. Force vs. time; Basonetic 2040

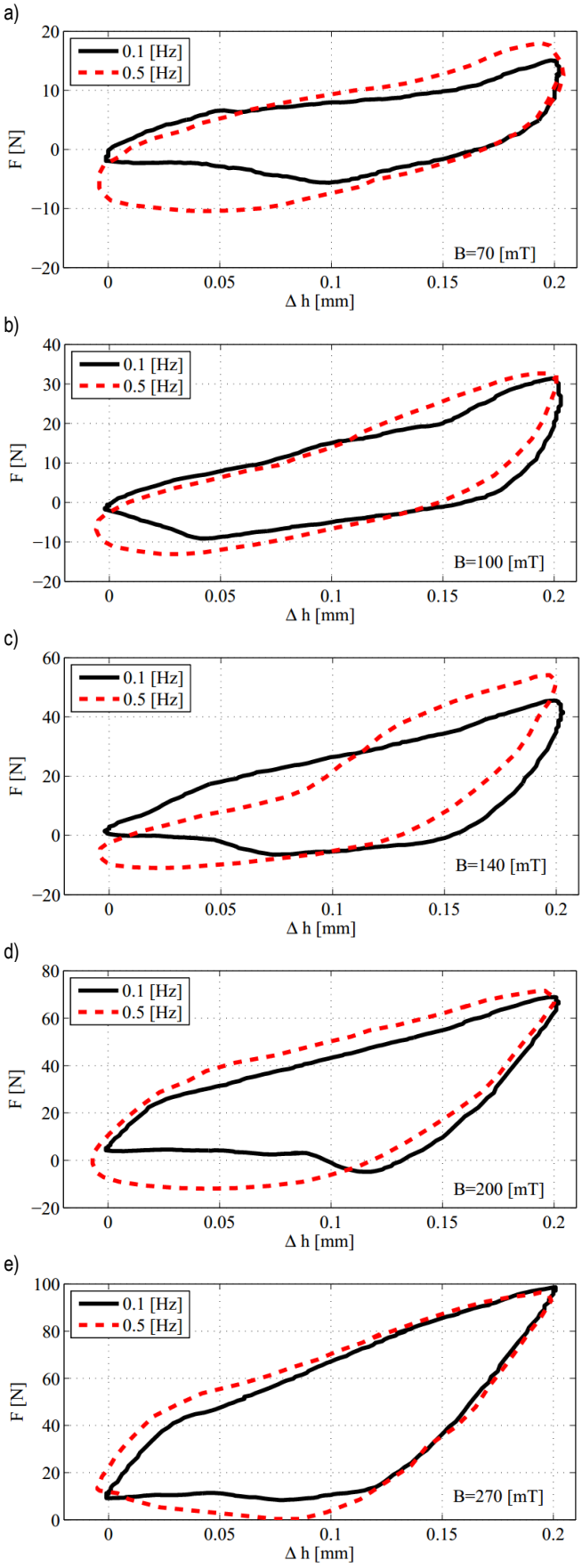

Fig. 7. Force vs. time; Basonetic 4035

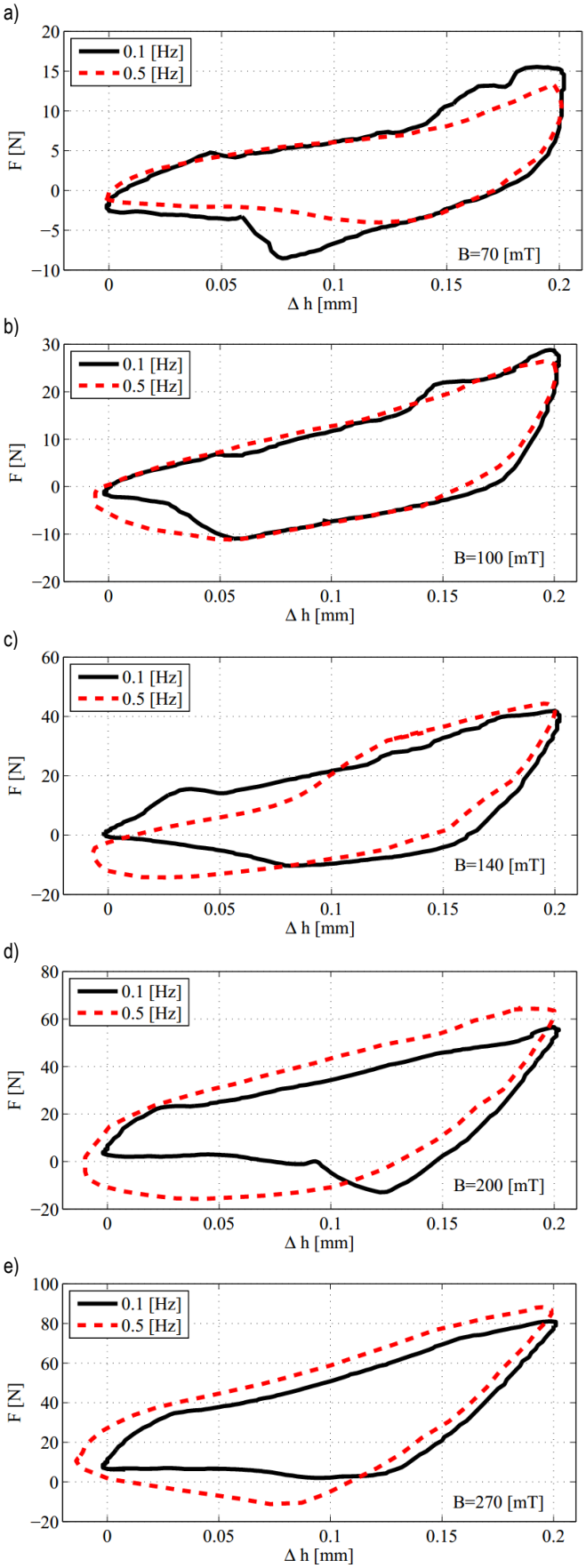

Fig. 8. Force vs. time; MRF-122EG

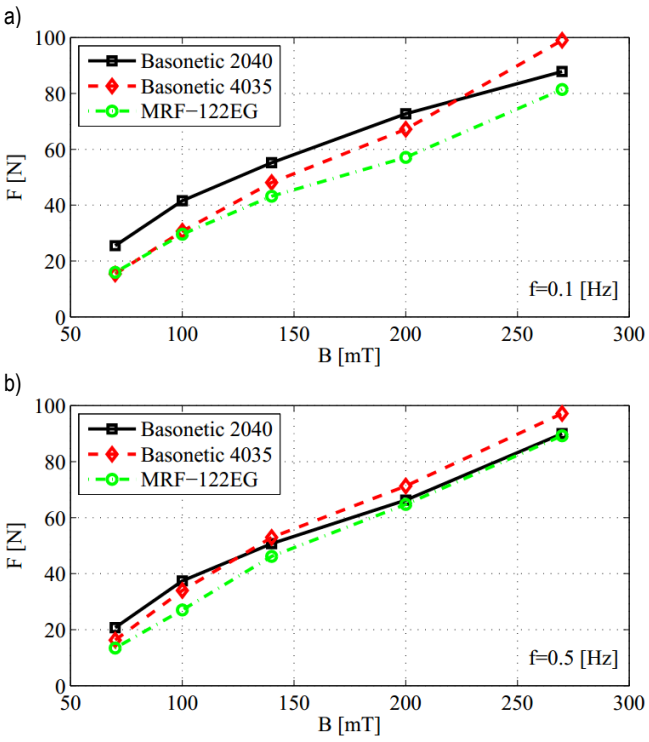

Fig. 9. Maximal force vs. flux density

It is worthwhile to mention, that for flux densities B<100mT the maximal squeezing forces registered for MR fluids with similar viscosity yet differing in saturation magnetisation are similar, evidencing the dominant influence that viscosity of the carrier fluid has on the behaviour of MR fluids operated in the squeeze mode under the action of magnetic field with a relatively low flux density.

The highest value of the maximal squeezing force is obtained for the MR fluid featuring high saturation magnetisation and low viscosity. The squeezing rate is found to have little effect on maximal squeeze force.

Fig. 10 shows the photo of MR fluid (MRF-122EG) after the experiments, revealing the carrier fluid released from the MR fluid. The identical process is observed for all investigated fluids. Release of the carrier fluid is associated with the fact that ferromagnetic particles in the squeeze zone are maintained in position by the magnetic field and the carrier fluid mostly will be pushed from the gap, causing the rheological properties of MR fluids to be altered. That is so because the (percentage) proportion of the solid phase in MR fluid is changed, too.

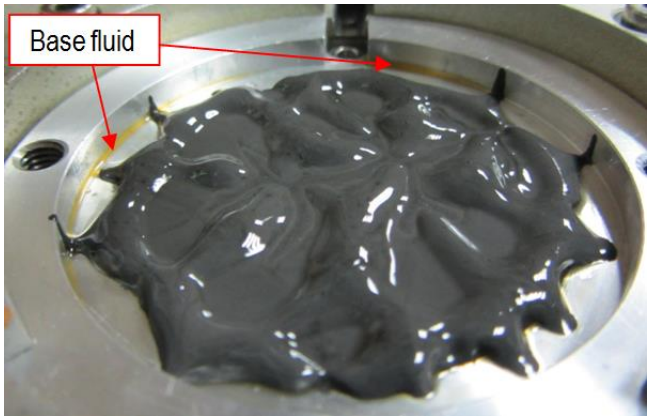

Fig. 10. MRF-122EG after experiments

4. SUMMARY

The paper summarises the results of testing of three commercially available MR fluids (Basonetic 2040, Basonetic 4035, MRF-122EG) operated in the oscillatory squeeze mode. Investigated fluids differed in their zero-state viscosity and in the level of saturation magnetisation.

The resistance to squeeze exhibited by MR fluids are determined by several factors, such as: yield stress, viscosity, strength of chain-like structures of ferromagnetic particles, the rate of formation of chain structures. Furthermore, the magnetostatic pressure associated with MR fluid and magnetic field interactions is a major determinant, too.

The behaviour of all investigated MR fluids was similar. The differences between the registered force values and the shapes of the squeeze force plots are attributable to various levels of intricacy of MR fluid particle structures and differences in viscosity of carrier fluids in the investigated samples.

It was observed that the carrier fluid tends to get separated from the ferromagnetic particles during the experiments.

No progressively increasing squeeze force was observed in consecutive squeeze test runs. It is reasonable to suppose, therefore, that no 'clumping effect' occurred during the experiments.

The behaviour of MR fluid operated in the squeeze mode is a complex research problem. At the current stage it is impossible to address and explain all aspects involved in the squeeze mode of MR fluid operation. The analysis is further complicated by lack of specific data about the composition and structure of investigated fluids, for instance the shape and size of forming particles.

REFERENCES

1. **Bonneau O., Frene J.** (1997), Non-linear behavior of a flexible shaft partly supported by a squeeze film damper, *Wear*, 206, 244- 250.
2. **Chengye L., Fengyan Y., Kejun J.** (2011), Design and finite element analysis of magnetic circuit for disk MRF brake, *Advanced Materials Research*, 181-182, 22-527.
3. **Farjoud A., Craft M., Burke W., Ahmadian M.** (2011), Experimental investigation of MR squeeze mounts, *Journal of Intelligent Material Systems and Structures*, 22, 1645-1652.
4. **Farjoud A., Vahdati N., Fah Y.** (2008), MR-fluid yield surface determination in disc-type MR rotary brakes, *Smart Materials and Structures*, 17, 3, 1-8.
5. **Gołdasz J., Sapiński B.** (2011), Model of a squeeze mode magnetorheological mount, *Solid State Phenomena*, 177, 116-124.
6. **Gołdasz J., Sapiński B.** (2011), Modelling of magnetorheological mounts in various operation modes, *Acta Mechanica et Automatica*, 5, 29-40.
7. **Guldbakke J. M., Hesselbach, J.** (2006), Development of bearings and a damper based on magnetically controllable fluids, *Journal of Physics: Condensed Matter*, 18, 38, 2959-2972.
8. **Horak W.** (2013), *Theoretical and experimental analysis of magnetorheological fluid squeeze flow mode*, PhD Thesis, AGH University of Science and Technology, Krakow.
9. **Mazlan S.** (2008), *The behaviour of magnetorheological fluids in squeeze mode*, PhD Thesis, Dublin City University.
10. **Salwiński J. Horak W.** (2012), Measurement of normal force in magnetorheological and ferrofluid lubricated bearings, *Key Engineering Material,* Vol.490, 25-32.
11. **Sapiński B.** (2006), Magnetorheological dampers in vibration control, *Uczelniane Wydawnictwa Naukowo-Dydaktyczne AGH*, Kraków.
12. **Tao R.** (2011), Super-strong magnetorheological fluids, *Journal of Physics: Condensed Matter*, 13, 50, 979-999.

13. **Zhang X. J., Farjud A., Ahmadian M., Guo K. H., Craft M**. (2011), Dynamic Testing and Modelling of an MR Squezee Mount, *Journal of Intelligent Material Systems and Structures*, Vol. 22, 1717-1728.
14. BASF The Chemical Company, http://www.basonetic.com/
15. LORD Corporation, http://www.lord.com/
16. Theoretical and experimental analysis of thrust slide bearing lubricated with magnetic fluid. National Science Centre, contract number 1185/B/T02/2011/40.

This research is supported by the National Centre for Research and Development under grant No. PBS 1/A6/3/2012.

THE SENSITIVITY OF A PHOTOGRAMMETRIC METHOD IN FORMABILITY ANALYSIS

Ján SLOTA*, Miroslav JURČIŠIN*, Ivan GAJDOŠ*, Emil SPIŠÁK*

*Faculty of Mechanical Engineering, Department of Technologies And Materials, Technical University of Košice, Letná 9, 042 00 Košice, Slovakia

Jan.Slota@tuke.sk, Miroslav.Jurcisin@tuke.sk, Ivan.Gajdos@tuke.sk, Emil.Spisak@tuke.sk,

Abstract: Nowadays is a possible to implement numerical simulation and photogrammetric inspection to the complex process chain of inspection. In the recent years there has been significant progress in accuracy improving of these methods of inspection in pre-production or post-production stage of manufacturing. This article discusses these two methods from sensitivity and comparison point of view. Most attention has been paid to the photogrammetric method and his sensitivity to using different approaches. Results were compared with the result of numerical simulation and experiment. Numerical simulation was performed in static implicit finite element code Autoform. For this purpose, GPS cover of galvanized steel of DQ category was used for inspection. In this paper was proved that photogrammetric method of strain measurement is highly sensitive on the various external factors. Further results and findings are included in the next chapters of this paper.

Key words: Photogrammetric Method, Strain Measurement, Deep Drawing, Simulation

1. INTRODUCTION

Numerical simulation and optical photogrammetric methods are nowadays frequently used inspection tools of manufacturing process. This is evidenced by the amount of scientific articles and conferences aimed to this problematic all over the world that dealt with use of these methods in the various fields of manufacturing. For example exploitation in the analysis of optimisation of forming process of drawnpiece (Fracz et al., 2013), health care services (Goellner et al., 2010), validation process of sheet metal materials of case study, in Audi corporation (Griesbach, 2010), in the analyses of draping cracks in the glass fiber textile industry (Kruse and Wendland, 2010), analyses of deep drawing process of GPS cover (Slota and Jurčišin, 2010) and many others applications. Photogrammetric measurement of strain works on the method of digital image correlation (DIC), and several publications were devoted to the detailed description of the DIC method. For example in the analyses of monitoring crack growth using videoextensometry techniques (Ambriško and Pešek, 2011), videoextensometric monitoring of various deformation characteristics in a static tension loading (Hlebová et al., 2011) or photogrammetric monitoring of deformation process using different strain rates (Mihaliková et al., 2011). In this paper, photogrammetric measuring was performed using ARGUS system. ARGUS is the contactless measuring system that on the basis of optical scanning allows predicting critic areas which are taking places during forming process. On the sheet metal is before forming applied grid of circle points. Size of these points is obviously between 1 and 6 mm. Grid is deformed at the same time as the sheet metal is deformed. Grid of circle points is by the influence of direction and intensity of stresses deformed, and is changing his shape. Measuring consists on the photogrammetric principle where surface is scanned using CCD camera with high resolution. Pictures are taken from different angles, and with using of image processing are computed 3D coordinates of grid points. Distances between points of grid are defined by lateral distortion. On the basis of law of volume preservation are computed decompositions of major and minor strains, thickness reduction or critical areas of drawn part, etc. (ARGUS User Guide, 2011). Digital image correlation method and numerical simulation of deep drawing process is useless, if the results are not corresponding with results of experimental measuring. Therefore is necessary to investigate difficulties associated with new progressive methods of inspection. In this paper was investigated GPS cover. Five different depths of drawn part were inspected. Results were compared with results of experimental measuring. Process was modeled in static implicit simulation software Autoform. Autoform is simulation software which is developed in cooperation with many world known companies as for example Audi, Arcelor, ThyssenKrup but also by HP whether IBM (Cover story: Focus on CAD CAM and simulation, 2011). As was mentioned, software works with implicit time integration strategy which is in every time step starting from the previous time step and a mesh is generated using local refinement due to requiring accuracy of problem, which is calculated resulting from current mesh. This solving process is iterated until the estimated error is between bounds of the interval of requiring precision. If the time step between new iteration is not too large, the time of solving process is usually very small (Schmidt and Kunibert, 2004).

2. EXPERIMENTAL PROCEDURE

The aim of this experiment was to investigate difficulties which were observed during the inspection of part using photogrammetric measuring method. For this purpose was used ARGUS measuring system which is type 12M, with resolution of camera 12 million pixels in case of photo camera and system 5M with 5 million pixel resolution in the case of video camera. Diameter of points etched on sheet was 1 mm. Distance between their centers was 2 mm, but measuring was possible also in the middle points

of grid, it means that measurement was performed in the minimal step distance about 1 mm. The accuracy of the ARGUS system within strain measurement is up to 0.2% [9]. Mechanical properties of the drawn part made of mild steel DX 52 D are in the Tab. 1. Thickness of the blank was 0.5 mm. Initial shape of the blank, with etched grid is illustrated in the Fig. 1. Dimensions highlighted in the Fig. 1 are a x b with values 44 x 160 mm, respectively.

Tab. 1. Mechanical properties of investigated steel

Steel	R_e [MPa]	R_m [MPa]	A_g [%]	C [MPa]	n [-]
DC 52 D	264	360.5	15.9	568	0.13

The grid of points was etched by electrochemical method using electrolyte which is suitable to the zinc coated surface of sheet. Special anti-reflexive spray was available as a last option in order to avoid inaccuracies related to the reflexive effect, because it can influence measurement in terms of strain amount. Illustration of image in ARGUS measurement is illustrated in the Fig. 2. Blue colour of element represents elements which are detected and rendered. Empty place represents place which is insufficiently recorded and therefore is necessary another photo from different angle. To compensate optical distortion and better locate all reference points the picture calibration was used.

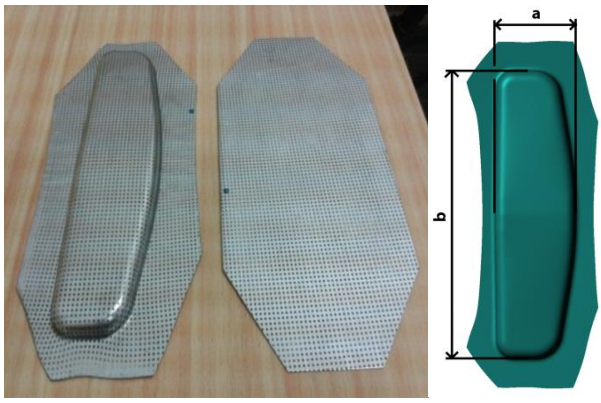

Fig. 1. Final shape and dimensions of the part and the blank

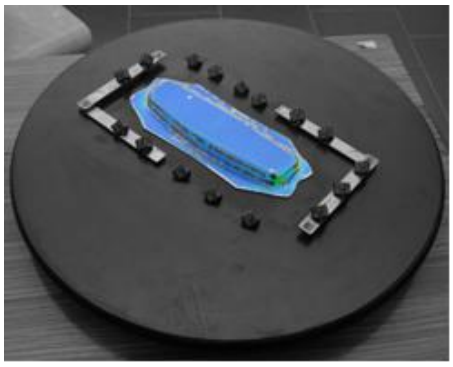

Fig. 2. Photogrammetric strain measurement in ARGUS using video camera

Drawing process was performed in the hydraulic press ZD 40. In order to minimalize friction, teflon film was used. This experiment had several objectives. First objective was to etch grid of points on 7 blanks illustrated in the Fig. 1 right, measure strains by photogrammetric method and compare results of measuring considering the shape of part and amount of major strains. Best 5 blanks were subsequently used for the deep drawing process and again inspected with ARGUS system where thickness reduction was measured and compared with results of numerical simulation and experimental measurement. Next objective was to quantify difference between scanned results of blank with and without anti-reflexive spray. For better illustration, difference between surface of sheet with and without the anti-reflexive spray is illustrated in the Fig. 3. Last objective was to identify differences between results of the measuring using photo camera and video camera.

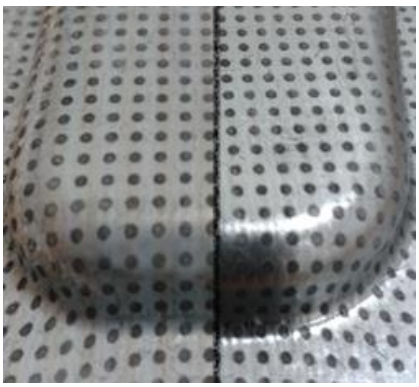

Fig. 3. Area with developer (on the left) and without developer

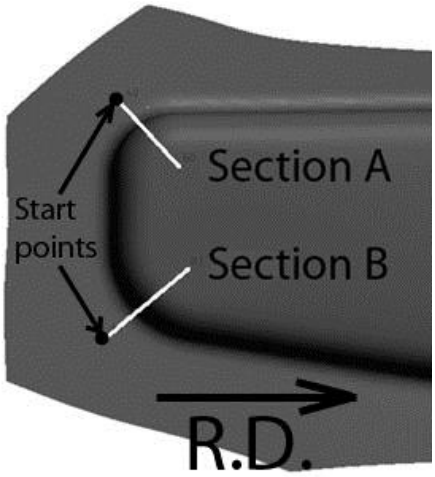

Fig. 4. Sections on the drawn part with highlighted sections, start points of measuring process and rolling direction

As was mentioned, deep drawing process was modelled in the static implicit code Autoform. This code is discretizing blank by triangular mesh. For better precision, element size was set to 1 mm. Number of integration point was automatically set to the value 11. This value is automatically set as soon as springback computation is required. Angle of triangular element was set to the value 22.5°. Maximum level of refinement was set to the value 4. Implies from this, minimal element size in places where was sheet maximally deformed was 0.0625 mm. Such small refinement was not localized on the final shape of part after simulation. Shell elements were used in process of numerical simulation. Hardening curve was defined using approximation function which is available in Autoform code and Hill's 48 yield criterion was defined with defining R_e and r values in directions 0, 45 and 90°

to the rolling direction. These values were 1.28, 0.89 and 1.71 respectively. Coefficient of friction was set to the value 0.15 and the gap between punch and die was equal to the thickness of the sheet except for the critical places on the radii where the gap was increased about the value of 10 % of the sheet. Comparisons of results obtained from experimental, numerical and photogrammetrical measuring were investigated in two sections of part curvature, which are illustrated in the Fig. 4. These two part curvatures were selected due to existence of the most critical strain and stresses in these areas. Experimental data were obtained in the 8 selected local places of curvatures.

3. RESULTS AND DISSCUSSION

Results of measurement differences between two cases – with and without anti-reflexive spray will be discussed as first. Shape of scanned blank and value of major strain is considered. Since the sheet is so far not loaded by any force, expected value of major strain is 0. However, as experiment shown, by the inaccuracies of scanning or etching, value of major strain is not equal to zero. Also is observed small difference between shape of the same surface of blank with and without anti-reflexive spray. Result is illustrated in the Fig. 5.

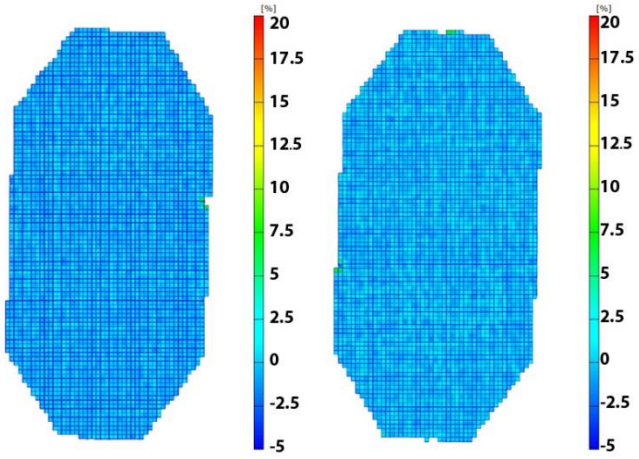

Fig. 5. Results of scanning by ARGUS. On the left side is scanned blank with anti-reflexive spray and on the right side is scanned blank without the anti-reflexive spray

Tab. 2. Influence of anti-reflexive spray

Parameter	With spray	Without spray
Max. MS [%]	7.93	8.25
Min. MS [%]	-3.49	-1.66
Average of MS [%]	0.62	0.48
Standard deviation of MS [%]	0.54	0.62
Difference [%]	29.2	

First of all as can be seen, on the sheet are measured positive and negative values of major strain (MS) before forming. This may be caused by several errors which will be described in further experimental result. In this case is experiment directed to the influence of anti-reflexive spray. Shape of blank is almost the same in both cases, but there is difference in measured values of strain. In sprayless case is measured maximum major strain of value 8.25 % and in the other case is maximal in the same place 7.93 %. Greater difference in the minimal value of major strains in case without spray (-3.49 %) and with spray (-1.66 %) occurred. It was computed, that in case with spray was arithmetic value of major strain in longitudinal section 0.62 % and standard deviation 0.54 % and in the case without spray was arithmetic value of major strain 0.48 % with standard deviation 0.62 %. For better understanding, results are illustrated in the Tab. 2.

Difference is calculated using following equation:

$$d = \frac{MS_S - MS_{WS}}{MS_{WS}} \quad (1)$$

where: d – difference, MS_S – Average of major strain with the application of anti-reflexive spray, MS_{WS} – average of major strain without the application of anti-reflexive spray.

From results in Tab. 2 implies, that when anti-reflexive spray is used, value of major strain in this case is higher about 29.2 %. Differences could be caused by the small change of circle diameters after layer of anti-reflexive spray was applied. However, when the spray was used, smaller standard deviation of results occurred. It means that points showed a higher degree of uniformity. Local places where major strain reached value up to 8 % may be etched incorrectly – for example, time of etching was exceeded or surface of sheet was affected by the various undesirable substances. Since the value of major strain measured by ARGUS is higher using anti-reflexive spray, it should be used only in cases where it is necessary, so in cases where the surface of sheet is highly reflective.

On all blanks in pre-production phase was etched grid of points in order to perform measuring which will illustrate various inaccuracies of etching and measuring. It is considered that the value of major strain on the sheet before forming is equal to zero. Results of measuring showed, that reality is different. First, as is illustrated in the Fig. 6 and 7, empty places on the blank are observed and also different distribution of major strain is observed. From illustrated results implies, that not all blanks were scanned sufficiently enough. Especially on samples marked as 3 and 6 are visible empty places, where points were not recognized. Maximal and minimal measured major strains are illustrated on the legend, and results of average major strains and thickness reduction (TR) through the longitudinal sections are in the Tab. 3. In either case was measured major strain equal to zero. From approximately 200 measured values on the each sample were all values of major strain greater than value 0.007 %.

Tab. 3. Strain and thickness reduction of etched blanks

Sample number	Average of MS [%]	Average of TR [%]
1	0.55	0.26
2	0.91	0.15
3	1.86	0.66
4	0.59	0.42
5	0.73	0.17
6	1.22	0.09
7	0.56	0.4

Samples number 3 and 6 were scanned in insufficient quality, therefore for further experimental procedures were not used. Omitted places on the scans illustrated in the Fig. 5 and 6 may be caused by several factors as insufficiently clean surface, inequality of surface, errors during etching caused by long time of effects of electric current, imperfect photogrammetric detecting by cam-

era, different light in the laboratory where the measurement takes place, different angles of taking photos etc. Software is defined in the way that diameter of etched point is equal to 1 mm, but real diameter may be different and mentioned phenomenon may cause that points are smaller or larger than is defined and software it evaluate that blank was already loaded.

Next experimental procedure was strain measuring by two approaches. Differences between strain measuring with photo (PC) and video camera (VC) were discussed. Both of these methods have advantages and disadvantages. Advantage of using photo camera is possibility of measuring parts which are larger, since video camera is placed on the tripod and is difficult to scan larger parts from one place. Advantage of using video camera is that is more users friendly. Measured part is placed on the turntable, and photos are making by the simple computer commands. Blank were scanned by these two methods and results will be discussed. First, distribution of major strains and shape of blanks are in the Fig. 7.

Results are graphically illustrated in the Fig. 8 and values are evaluated in the Tab. 4. Shape of the blank is approximately equal. Minimal measured major strain differs by a very small amount. Difference between averages of major strain calculated using equation 1 in longitudinal sections is 20 %.

Tab. 4. Strain and thickness reduction of the blank

Parameter	PC	VC
Max. MS [%]	6.63	4.28
Min. MS [%]	-1.88	-1.89
Average of MS [%]	0.65	0.52
Standard deviation of MS [%]	0.85	0.74
Difference [%]	20	

From the results presented in the Tab. 4, the standard deviation and average of major strain is smaller in the case of video camera, it can be assumed that video camera has a smaller resolution and not whole areas of points were scanned accurately enough. Using of video camera is beneficial in the case of smaller parts, because is simpler and faster to measure strains. Photo camera is the only option in the case of measuring larger parts.

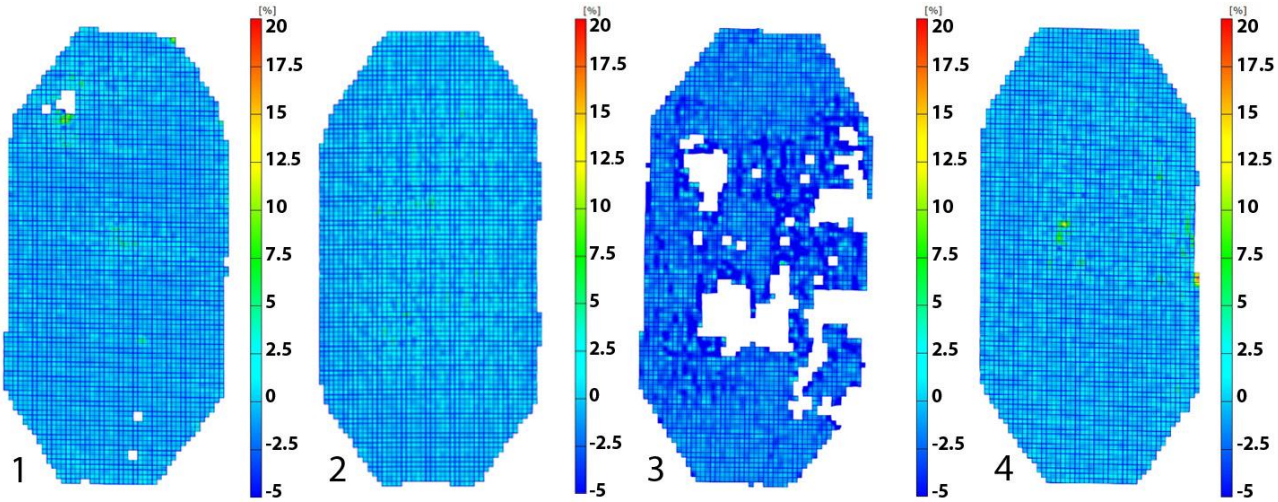

Fig. 6. Strain distribution on samples 1-4 from photogrammetric system. Data were measured using VC system

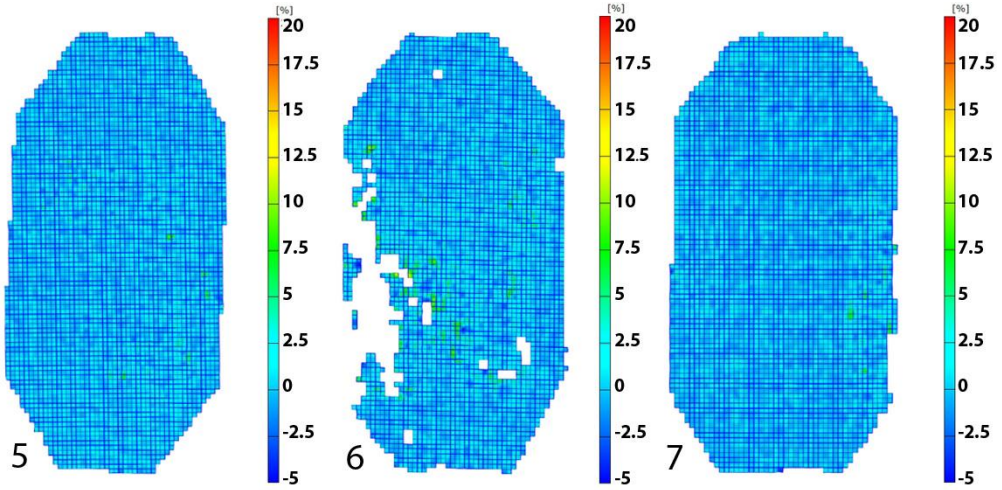

Fig. 7. Strain distribution on samples 5-7 from photogrammetric system. Data were measured using VC system

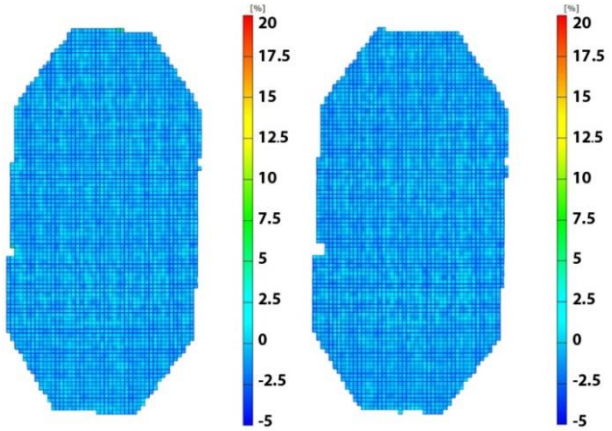

Fig. 8. Results of scanning using different sensing devices. On the left result of scanning using PC system, and on the right result of scanning using VC system

As in the previous cases, these differences will be discussed in the further chapter. Last experiment was focused to the comparison of photogrammetric measuring method, numerical simulation results and experimentally obtained results. After the evaluation of measurement illustrated in the Fig. 6 and 7, five blanks were used to the drawing process and GPS cover was drawn. Blanks number 3 and 6 were rejected, because if there has been visible significant problem during surface scanning in pre-production phase, it can be expected that there will be problem also during scanning in the post-production phase. In order to compare results, five different drawing depths were selected from 16 to 20 mm. Even though in previous experiments was as a comparison parameter selected major strain, thickness reduction is more suitable for inspecting final product of deep drawing process. Therefore in this comparison was chosen this parameter. In the Fig. 9 – Fig. 13 are illustrated results in the two sections which are highlighted in the Fig. 4. Section curve illustrated in the Fig. 9 – Fig. 13 was obtained from measuring in ARGUS. This curve was plotted in order to illustrate position of GPS cover wall in which thickness reduction was measured.

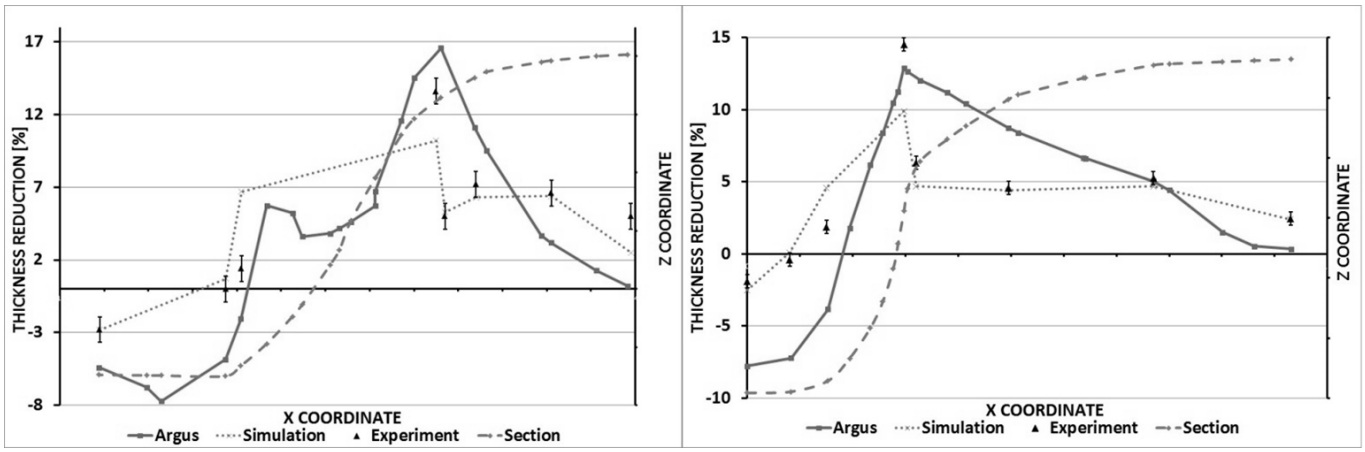

Fig. 9. Depth of drawn part equal to 16 mm. Section A on the left, section B on the right

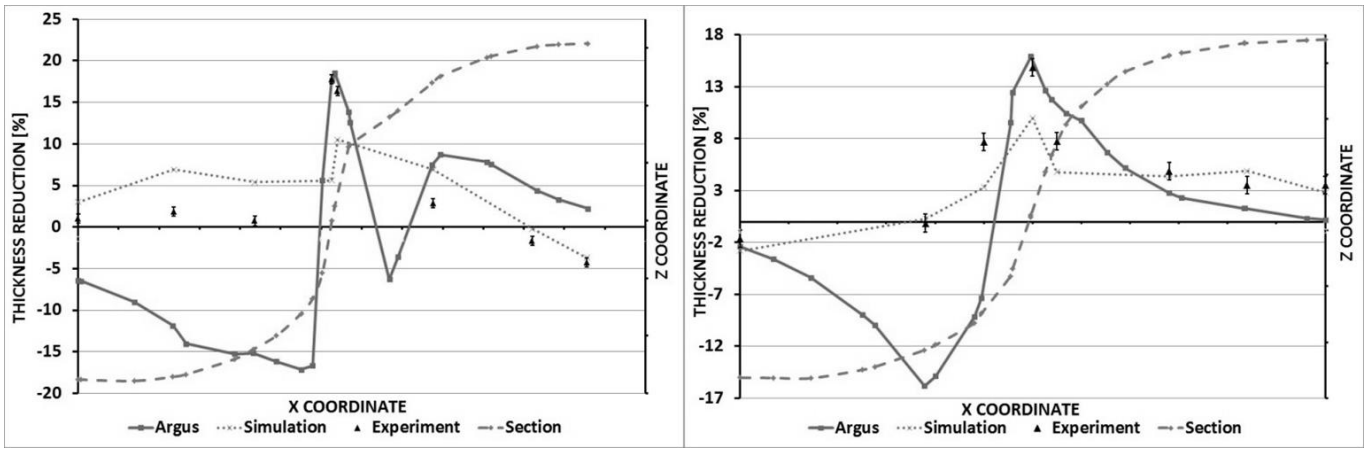

Fig. 10. Depth of drawn part equal to 17 mm. Section A on the left, section B on the right

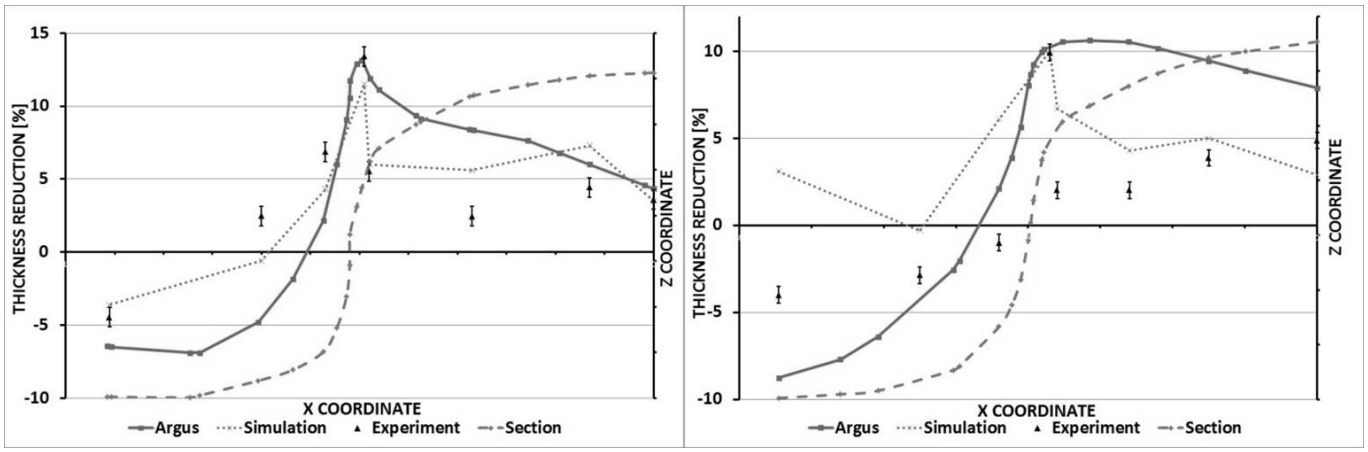

Fig. 11. Depth of drawn part equal to 18 mm. Section A on the left, section B on the right

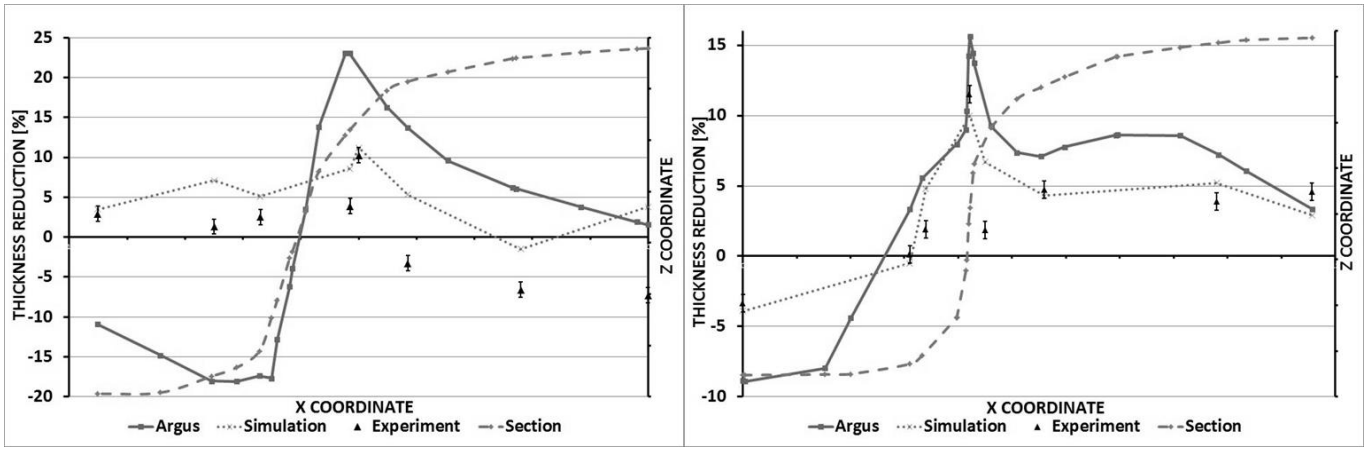

Fig. 12. Depth of drawn part equal to 19 mm. Section A on the left, section B on the right

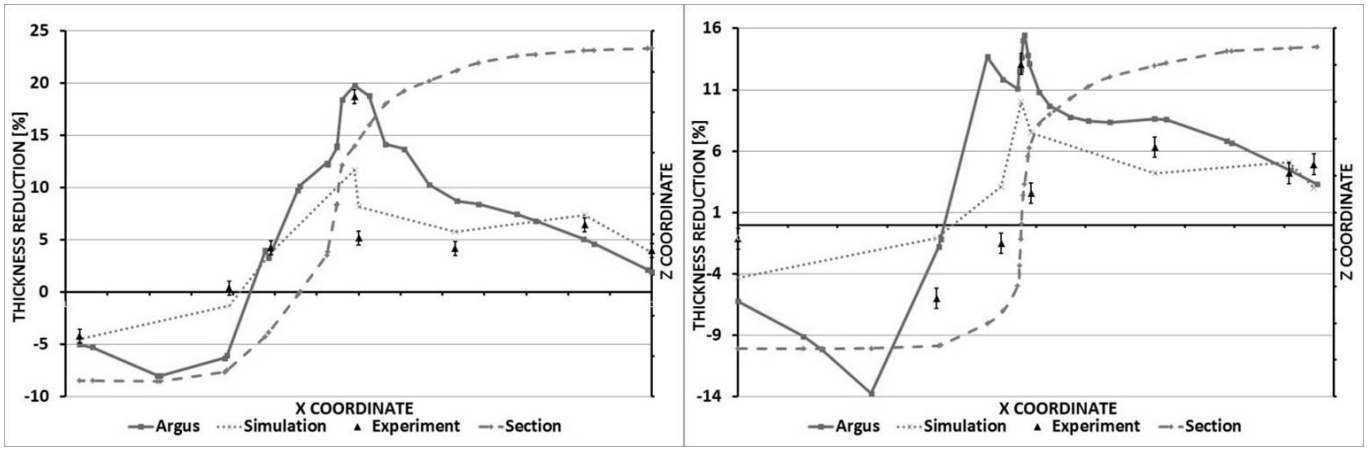

Fig. 13. Depth of drawn part equal to 20 mm. Section A on the left, section B on the right

Results shown in the Fig. 9, for depth 16 mm are result of 8 experimental measuring, numerical simulation and photogrammetric method. In case of experimental measuring, measurement uncertainty was computed in every single point. In this case, numerical simulation was more accurate, because there was observed a greater overlap with experimental measuring. In case where drawing depth was set to 17 mm, numerical simulation and photogrammetric scanning had a different course of results. As was illustrated in the Fig. 10, trend of the course is copied a greater in case of numerical simulation. In case, illustrated in the Fig. 11, where drawing depth was set to 18 mm, numerical simulation and photogrammetric scanning had approximately the same distribution of thickness reduction. However, in the case of section B, in the first point, there was a great difference, because while numerical simulation computed that there was a positive thickness reduction, in the case of photogrammetric measuring there was measured negative thickness reduction what is corresponding with experimental measurement. Result of experiment, where

drawing depth was set to 19 mm is shown in the Fig. 12. As from this graph implies, numerical simulation was more accurate in comparison to experimentally obtained values. The most critical local places were overestimated by ARGUS, what may not cause problems in technical practice. In the last drawing depth illustrated in the Fig. 13, as well as in the previous case, numerical simulation was more accurate. However, numerical simulation underestimated the value of thickness reduction in the most critical area. This may cause a problems in the production, or problems with quality of final product. From Fig.9 –Fig.13 implies that thickness reduction for greater drawing depth is not growing uniformly. It was caused by the reason that for every drawing depth was used new blank.

4. CONCLUSIONS

In this paper, two progressive methods of formability analysis were compared. It was proved, that there is difference between measured values of strain using photogrammetric 5M and 12M camera. It was also proved that anti-reflexive spray influence amount of measured strain. It was found that photogrammetric system does not provide acceptable accuracy in the measurement of certain areas of draw piece. There were observed great sensitivity of different factors to the measured values. Among these factors in pre-production phase it can be included the time of etching, an appropriate electrolyte, etching process parameters, different type of measuring grid, quality of sheet surface and others. In post-production phase it is type of used camera, application of developer, interpolation parameters, different lighting conditions, angles of camera view, number of captured pictures, etc.

Numerical simulation of process was performed in order to compare results with photogrammetric system. It was found that results of numerical simulation corresponded with experimentally obtained data greater than photogrammetric system. Results of numerical simulation can be more accurate either by better material description and material models considering Bauschinger effect, apparent Young's modulus, etc. or sophisticated computing algorithms. There still exist areas for continued development in the case of photogrammetric measuring and numerical simulation.

REFERENCES

1. **Fracz W., Stachowicz F., Pieja T.** (2013), Aspect of verification and numerical optimization of sheet metal and numerical simulations process using the photogrammetric system, *Acta Metallurgica Slovaca*, 19, 51–59.
2. **Goellner M et al.** (2010), Photogrammetric measurement of initial tooth displacement under tensile force, *Medical Engineering & Physics*, 32, 883–888.
3. **Griesbach B et al.** (2010), Validation of sheet metal materials by forming analysis with automatic ARGUS measurement cell, *International conference for integration of optical metrology in industry and research,* Braunschweig, Germany.
4. **Kruse F., Wendland B.** (2010), Determination of draping characteristics of carbon glassfiber textiles using Argus, *International conference for integration of oprical metrology in industry and research,* Braunschweig, Germany.
5. **Slota J., Jurčišin M.** (2012), Experimental and numerical analysis of the deep drawing process using optical measuring system, *Zeszyty Naukowe Politechniki Rzeszowskiej*, 84-4, 37–45.
6. **Ambriško L., Pešek L.** (2011), Determination the crack growth resistance of automotive steel sheets, *Chemické listy*, 105, 767–768.
7. **Hlebová S., Pešek L., Kandra T.** (2011), Comparison of determination characteristics of the steel sheet in local and global area by the static loading using videoextensometry, *Chemické listy*, 105, 577–579.
8. **Mihaliková M., Ambriško L., Pešek L.** (2011), Videoextensometric measuring of deformation process in automotive steel at two strain rate levels, *Kovové materiály*, 49, 137–141.
9. **ARGUS USER GUIDE. (**2011), http://www.gom.com/.
10. **Cover story: Focus on CAD CAM and simulation**. (2001), Parametric die faces in one hour, *International sheet metal review.*
11. **Schmidt A., Kunibert G.S.** (2004), *Design of adaptive finite element software, The finite element toolbox,* Bremen: University of Bremen.

This contribution is the result of the projects implementation: Centre for research of control of technical, environmental and human risks for permanent development of production and products in mechanical engineering (ITMS: 26220120060) supported by the R&D Operational Programme funded by the ERDF and VEGA 1/0396/11.